Design of High-Performance Surfaces for Controlling Phase Transformation

By

Brian Tobelmann

A dissertation submitted in partial fulfillment
of the requirements for the degree of
Doctor of Philosophy
(Materials Science and Engineering)
in the University of Michigan
2021

Doctoral Committee:
Associate Professor Anish Tuteja, Chair
Assistant Professor John Heron
Professor Pramod Reddy
Professor Max Shtein

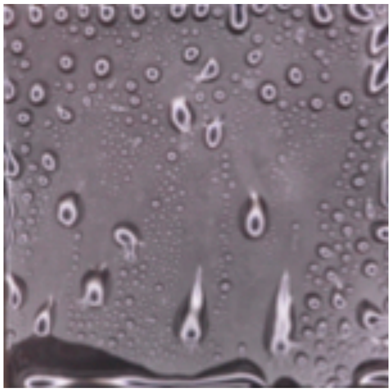

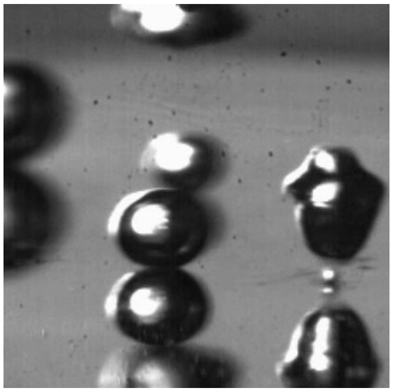

Brian Tobelmann

btobel@umich.edu

ORCiD: 0000-0002-1548-9481

Dedication

This work is dedicated to all of my family, past, present, and future; especially those that have pursued advanced degrees of their own and set a stellar example for me to follow.

Acknowledgments

Firstly, I want to recognize my late uncle Michael A. Cala who passed away during my doctoral work. He received his PhD from … in … and has been an inspiration throughout my academic career. His public service is appreciated, and he is greatly missed.

I thank my research advisor, Professor Anish Tuteja, who has pushed me towards constant improvement. He has provided an opportunity to explore the fringes of science and driven me forward in engineering challenges. His mentorship is greatly appreciated, and his teachings will continue to be a part of me work for years to come. Thank-you also to my committee members, Professor Pramod Reddy, Professor Max Shtein, and Professor John Heron, in supporting my development as a researching, sharing their expertise, and providing valuable input on my research and dissertation. I want to especially thank the professor John Heron, and his lab member Peter Meisenheimer, who collaborated on two of my projects and provided valuable development that would not have been possible without them.

Thank-you to all of the lab members in the Polymers, Surfaces, and Interfaces research group. Every member has played a role in the success of my work and without the support of the group, I would not be where I am today. I want to especially thank Abhishek Dhyani, Brian Macdonald, and Jiayue Huang who I worked with closely on one project, their expertise was critical, and I enjoyed collaborating with them. To Fan-Wei, I have confidence you will pick up the work I leave off on and I look forward to seeing the progress you make in the field. Lastly, to all of the past and current group members I have worked with, Kevin, Mathew, Sarah, Jing, Catherine, David, Alex, Taylor, and Sujay; I will miss the comradery in the lab, even though the last year has been an odd one for us all.

I thank all of the programs and administrators I worked with during my 4+ years, especially the department of Materials Science and Engineering for giving me this opportunity to pursue my passions at the University of Michigan. Renee Hilgendorf has always been supportive and provided assistance whenever I got confused. I also owe a great deal of gratitude to the staff and administrators of the Biointerfaces Institute, Michigan Center for Materials Characterization, Lurie Nanofabrication Laboratory, and the Van Vlack Laboratory. I would have been unable to do so much work without the assistance and expertise from everyone in those programs.

Most importantly, I thank all of my family that have provided the necessary support to get this far in my academic career. My parents worked very hard to provide a good education for me and I will never be able to fully repay them for every opportunity they gave me. They set an example with masters of their own and provided me with the STEM opportunities that have brought me to engineering. My sister Jessica, for providing guidance and assistance throughout my undergraduate career that opened the opportunities for me to do research which ultimately brought me to graduate school. My oldest brother Matthew, who has always been a support system and an inspiration for me. As much as I try to not walk in his exact footsteps, he has led such great example that it is difficult not to strive for the greatness he has exemplified. And to my brother Stephen, he has been a constant support in Ann Arbor throughout my doctorate (even though he followed me here), I would not have made it through these years without his jovial spirit and welcoming support. Thank-you especially to all of my friends from undergraduate studies and the Wisconsin Sailing class of 2012 (Jen Burke, Elliot Busta, Katie Hall, Whitney

Kent, Peter Grimmer, Caya McFalls, Laura Boot, Leslie Poole, Ian Norman, Ian Walter, Teddy Brown, and Tom Sorenson). Your support over the last 8+ years has been unrivaled, and I am certain that, without the lighthearted times you all, I would have lost my drive long ago. Lastly, to all of my close friends and family members with advanced degrees, you set a great example and make it difficult to live up to your hard work and dedication: David Tobelmann, Rosemary Tobelmann, Matthew Tobelmann (PhD), Jessica Fritz, Cristi Tobelmann, Michael Fritz, Michael Cala (PhD), Gregory Cala (PhD), Alexis Sears, Terri Sears, Jen Burke, Peter Grimmer, Caya McFalls, Ian Walter, and Tom (12.25) Sorenson.

Table of Contents

Chapter

List of Figures

List of Tables

Abstract

Controlling phase transformation has been of particular interest for the past several decades. The properties of a phase transformation interface have a direct correlation with the performance of the surface and control of this performance opens up numerous opportunities for applications in: efficient liquid condensers, steam power production, oil separation and distillation, ice resistant aircraft, and microelectronics cooling. Previous research has employed a variety of techniques to control phase transformation from selectively textured surfaces, interfacial free energy modified surfaces, and porous surfaces infused with lubricant. However, while many of these researchers have focused on the capability to induce phase transformation on these surfaces, there has been a lack of focus on the optimization of these processes. Furthermore, many of the prior technologies suffer from poor durability and lifespan longevity in their intended applications. These factors have combined to inhibit the widespread adoption of these technologies due to cost and logistical pitfalls.

This dissertation presents a systematic method to design optimized surfaces to control phase transformation on a surface while simultaneously enhancing the durability of the surfaces to resist environmental damage. The first research chapter addresses condensation heat transfer surfaces, optimizing the interfacial heat transfer when condensing a liquid. Using thermodynamic analysis, we design parameters for the optimal surface conditions during condensation, identify surface treatments that have selectively tuned contact angle and

hysteresis, and display quantifiable improvements. These novel design parameters go against prior trends in condensation and exhibit efficient condensation on hygrophilic surfaces by minimizing the hysteresis on a surface using amorphous thin films. The second research chapter then addresses boiling heat transfer, maximizing the capability and useability of a smooth surface. No previous study has effectively used smooth surface modifications for boiling due to the fragility of such surface modifiers. This novel surface coating, based on diamond-like carbon, demonstrates high temperature stability and simultaneously enhances the heat transfer rate and maximum capable heat transfer compared to an uncoated surface.

In chapter 4, we then transition to examining icing performance and the ability to delay the onset of ice formation on a surface, typically referred to as frosting. There have been a multitude of studies that have developed anti-icing surfaces, though scalability and applicability have been varied with no clear use cases. We demonstrate a simple coating that inhibits ice formation in conditions far harsher than would be experienced in a real-life application. The facile coating can easily be tuned to the specific application and performance properties required for use. We then compare it to prior state of the art and prove a significant improvement under standardized test conditions. Lastly, the final chapter utilizes the learnings of diamond-like carbon in chapter 3 to develop a novel fluorinated diamond-like carbon that maintains a superhydrophobic state and resists high temperature and abrasion. Such a surface coating exhibits as a useful application for nucleate boiling cooling of microelectronics, the fluorinated surface can conduct the same amount of heat as an uncoated surface at about 20°C lower temperature. This surface is also the first to demonstrate superhydrophobic capabilities in environments in excess of 500°C. The work herein has identified the properties necessary to optimize phase transformation surfaces and developed coatings that conform to the optimized design and display the predicted enhancements.

Chapter 1

Introduction

1.1 Introductory Remarks

Surfaces with controlled wettabilities have garnered significant attention for decades due to their usefulness in a variety of applications like stain resistant textiles[1], marine drag reduction and anti-biofouling[2], and self-cleaning surface.[3] There have been a variety of published methods to reduce the interactions between a liquid and surface such that droplets easily roll or slide off.

Modified surfaces have been of particular interest for the use in phase transformation applications. Phase transformation of water is associated with nearly 500x as much energy as the specific heat of water, leading to an opportunity for enhanced heat transfer if phase transformation can be stimulated. Further, it has been shown that the Gibb's free energy barrier of phase transformation varies directly with the free energy of the surface.[4] The control of surface free energy has been shown to enhance both the vaporization (boiling) and condensation of water.[5–7] To maintain an efficient surface, droplets or bubbles must be allowed to quickly form and easily depart from the surface without coalescing with nearby neighbors. Surface texturing has been of particular interest as it can be used to enhance both boiling and condensation.[8,9] To further improve condensation behavior, lubricant can be infused into the surface so that droplets are held on a lubricant layer to slide freely, or the texture can be treated such that droplets literally jump off the surface uninhibited.[10,11] Lastly, texturing can improve boiling through a variety of methods: increased surface area, capillary wicking, and increased nucleation sites.[12–14] Prior work has demonstrated numerous advances in phase transformation heat transfer utilizing one or more the above strategies.

However, many of these methods are limited by their inability to scale to a useful point, suffer from severe degradation with sustained use, and/or are only useful in specific conditions that limit their widespread use. This thesis works to address these downfalls by developing surfaces that are optimized for their intended use, are robust for sustained use cases, and have direct applicability for widespread adoption. The surfaces fabricated have been tested against comparable, state of the art, surfaces to display excellence in the field of research.

1.2 Wettability of Smooth and Textured Surfaces

The wettability of a surface is derived from the interaction between a liquid and the surface. The manner in which a liquid will interact with the surface is dependent on a wide array of variables, including the roughness, surface free energy, liquid surface tension, polarity, chemical homogeneity, and crystallinity. This interaction is typically quantified as the contact angle (θ) between a liquid droplet and the surface (**Figure 1.1**), varying from $0° < \theta < 180°$.

1.2.1 Contact Angle and Surface Tension

Both liquids and solids inherently prefer to remain in a bulk and resist surface area; in the absence of any external forces, a liquid would revert to its minimum surface area shape, a sphere. Surface tension can be considered a measure of the energy required to deform these substances and create additional surface area. The contact angle between a liquid and a smooth surface is based on the energy balance at the 3-phase contact line; where the solid-vapor (γ_{sv}), liquid-vapor (γ_{lv}), and solid-liquid (γ_{sl}) meet.

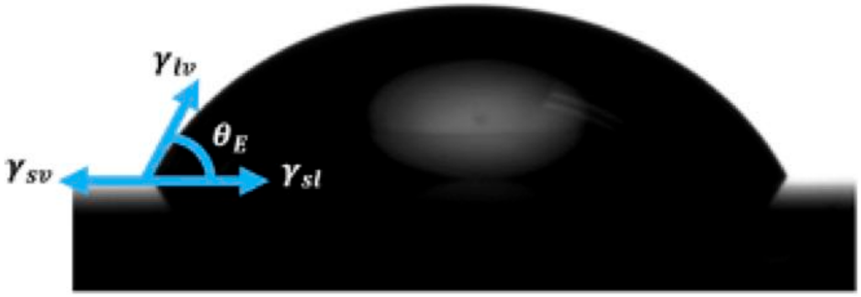

Figure 1.1: Liquid droplet on a smooth surface exhibiting a contact angle at equilibrium (θ_E), determined by the balance of forces at the 3-phase contact line.

The equilibrium contact angle (θ_E) can be determined using the Young's Equation (below) and the corresponding liquid surface tension (γ_{lv}) and surface free energy (γ_{sv}).[15]

$$cos\theta_E = \frac{\gamma_{sv}-\gamma_{sl}}{\gamma_{lv}} \tag{1.1}$$

Typically, the solid-liquid interfacial tension (γ_{sl}) is unknown as it depends on the interactions between the solid and liquid. However, the solid-vapor (γ_{sv}) and liquid-vapor (γ_{lv}) are known, which necessitates the need to measure the contact angle so as to infer γ_{sl}.

The contact angle is typically calculated through an optical method in which a camera is used in conjunction with software to calculate the visual contact angle of a droplet with the surface. While this is typically close to the actual contact angle of a surface, and is commonly used and reported in research, there are some inherent errors to consider. This method is a better reference for the average intrinsic contact angle. The Young Equation was designed for an ideal, homogeneous, solid surface, roughness, heterogeneity, and molecular interactions at the 3-phase contact line can all affect the contact angle.[16] While a visual measure will be used throughout this work, it is sufficiently close to an accurate measure, and the dynamic contact angles are more commonly used to give a more accurate representation of the liquid-surface interactions. If more accurate results are required, researchers will use methods like the Wilhelmy plate method[17] or capillary bridge system[18], though the accuracies of these methods are not needed herein. For a smooth surface, the maximum achievable intrinsic contact angle is $\theta_E \approx 120°$, which occurs on a fluorinated monolayer with a surface free energy $\gamma_{sv} = 9$ mJ m^{-2}.[19] Fluorine containing solids are typically desired for liquid repellency due to the electronegativity and low polarizability of the fluorine, which resist interactions with other molecules imparting the low adhesion properties desired.[20,21] Thereby the fluorinated monolayer would lend to the most liquid repellant surface, though there is a limit to the liquid resistance as no know substance can exhibit $\theta_E > 90°$ for any liquids with $\gamma_{lv} < 40$ mN m^{-1}.[22]

The surface tension γ_{lv} of a liquid can rather easily be determine experimentally through a variety of measurement methods. The pendant drop method is a commonly used technique in which a droplet it suspended from a needle. If the density of the liquid is known, the force of surface tension opposes the force of gravity on the droplet, and a profile can be fit to the droplet to calculate the surface tension via the Young-Laplace equation.[23] There are numerous other methods to calculate surface tension, including the Du Noüy ring[24], Wilhemy plates[25], maximum bubble pressure[26], and capillary rise[27] methods. **Table 1.1** lists the surface tension of various liquids, including those utilized herein.

Table 1.1: Surface tension of various liquids that are used, or referenced, throughout this work, in descending order by surface tension.[28–34]

Liquid	**γ_{lv} (mN m$^{-1)}$**
Water	72.1
Diiodomethane	50.8
n,n-Dimethylformamide	35.1
Toluene	27.9
n-Hexadecane	27.5
Chloroform	26.7
Dichloromethane	26.5
Acetone	23.5
2-Propanol	23.3
Ethanol	22.1
Methanol	22.1
n-Octane	21.1
1-Propanol	20.9
Krytox 100	17.0
Pentane	15.8
Vertrel XF	14.1
Perfluorohexane	11.5

Lastly, the surface free energy γ_{sv} can be determined through a comparative study utilize the prior two measurements (contact angle and surface tension). One of the simplest techniques is the Zisman method, which can be used to estimate the critical surface tension (γ_c). This method utilizes liquids with varying surface tension (ie n-Ethers with varying lengths) to determine the highest surface tension that would wet the surface ($\theta = 0°$). This technique is very rudimentary, and even Zisman carefully pointed out that the resulting γ_c is merely symbolic of the surface free energy but not equal to. Many subsequent studies have further refined this method to get a more accurate estimation of the surface free energy. One of these methods, which is used in this work, is the Owens-Wendt[35] calculation, which extends from the Fowkes[36] method. The Owens-Wendt calculation utilizes the contact angle from a polar liquid (typically water) and a non-polar liquid (hexadecane for $\gamma_{sv} < 25$ mJ m^{-2}; diiodomethane for $\gamma_{sv} > 25$ mJ m^{-2}), which have known polar and dispersive components to their surface tensions. From the contact angles and known surface tensions, the surface free energy γ_{sv} can be inferred. This method does have its own limits as it can only be utilized for surfaces on which at least two of the probe liquids do not wet (diiodomethane $\gamma_{lv} \approx 67$ mN m^{-1}). This limitation becomes essentially irrelevant for most studies as high surface energy materials (such as plasma cleaned Si or metals) are prone to hydrocarbon absorption to the surface.[37] This makes the accurate measurement of the contact angle and surface free energy of these surfaces exceedingly difficult, unless the surfaces are stored in a high vacuum environment with minimal atmospheric contaminants, and this results in widely varying reported literature values.[38] **Table 1.2** lists the surface energy of a selection of surfaces.

Table 1.2: Approximate surface energy of various solids and surfaces, including analogous solids to substances referenced throughout this work.[39–45]

Solid	**γ_{sv} (mJ m^{-2})**
-CF_3 monolayer	9
Perfluoropolyether	17.7
Polytetrafluoroethylene	19
-CH_3 monolayer	23
Polydimethylsiloxane	23.5
Polypropylene	31
Polyethylene glycol	48.3
Cellulose	89
Glass	~310
Titanium Dioxide	~530
Copper	1650

1.2.2 Wettability Terminology

How a liquid interacts with a solid can be categorized into two distinct states, "-phobic" or "-philic" where the former refers to a surface that resists wettin[67]g and the latter a surface that spontaneously wets. Generally, a surface on which θ > 90° is considered "-phobic" and θ < 90° is considered "-philic". When the liquid is water, these distinctions are termed hydrophobic and hydrophilic, and equivalent nomenclature exists for describing oils ("oleo-") and low γ_{lv} liquids ("omni-") as shown in **Figure 1.2**.

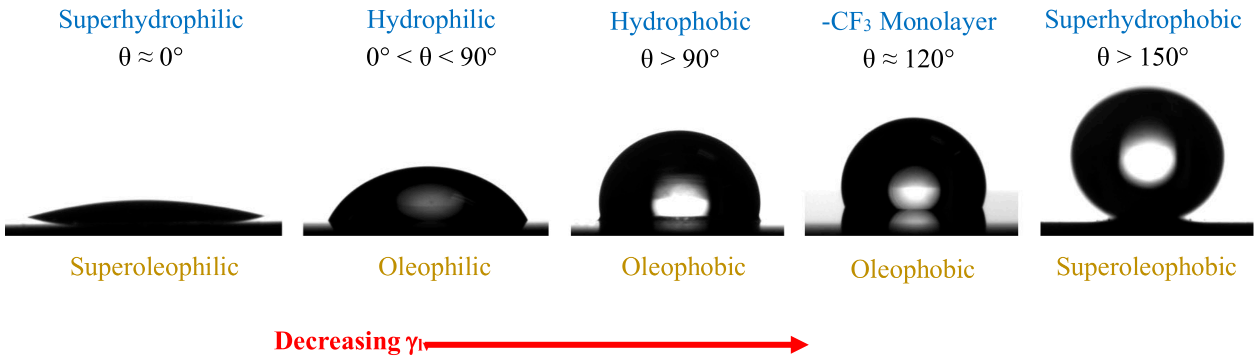

Figure 1.2: Conventional terminology for describing wetting and droplets representing the corresponding behavior. These representative images were captured on a goniometer using water on smooth Si substrates treated with decreasing surface energy: plasma-cleaned Si, polyethylene glycol, polydimethylsiloxane, and perfluoropolyether. The far right surface is a superhydrophobic surface made from a fluorintaed diamond-like carbon with rms roughness of ~100 nm. Below the images are the corresponding terminology for wetting behavior with oils.

There are numerous surfaces that have been reported to display contact angles about 120°, which is the theoretical limit for a perfect -CF$_3$ monolayer.[46–50] These surfaces are deemed “superhydrophobic” and display a contact angle in excess of 150°. This is only possible through the combination of hydrophobicity and roughness such that a liquid is suspended in a composite interface with the roughness; this leads to liquids easily beading up and rolling off the surface. The influence of surface roughness will be covered further in section 1.4. Some low γ_{sv} surfaces have been referred to as omniphobic despite $\theta_E < 90°$, typically associated with surfaces that can easily shed and repel low γ_{lv} liquids, though the literature is not consistent with this classification.[51,52] **Table 1.3** contains some commonly used nomenclature to describe the wetting behavior of various liquids on different surfaces.

Table 1.3: Array of possible wettability classifications that are commonly used by the scientific community. "Hydro-" refers to the distinction of water with a generally high surface tension and polarity, "Oleo-" refers to oils with moderate surface tension and are typically non-polar, and “Omni-” encompasses most low surface tension liquids which can include polar solvents and fluorinated liquids. Adapted from dissertation by Mathew Boban.

Nomenclature	**Liquids Repelled**	**θ (°)**	**Example Surfaces**
Superomniphilic/ Superhydrophilic	None	$\theta_E \approx 0°$	High surface energy solids (metals, glass, TiO_2)
Superoleophilic	Water	$\theta_E \approx 0°$	Typically moderate surface energy polymers that have roughness so as water displays more "-phobic" and oils display more "-philic"
Hydrophilic/ Oleophobic	Oil, not water	$\theta_E \approx 0°$ for water $\theta_E > 90°$ for oil	Counter intuitive surfaces since $\gamma_{lv,water} > \gamma_{lv,oil}$; achievable with functional groups that selectively wet water due to its polarity[53,54]
Hydrophobic	Water	$\theta_E > 90°$	A wide variety of solids including polyethylene and PTFE[55]
Oleophobic	Oil	$\theta_E > 90°$	Roughened PTFE[1]
Omniphobic	All	$\Delta\theta \approx 0°^{\dagger}$	Surfaces with fluorinated lubricant infused[56], smooth perfluorinated films[57]
Superhydrophobic	Water	$\theta_E > 150°$	Textured, hydrophobic surfaces, like the lotus leaf[58]
Superoleophobic	Oil	$\theta_E > 150°$	Electrospun or microstructured surfaces[59–62]
Superomniphobic	All	$\theta_E > 150°$	Hierarchically textured surfaces that are treated with a perfluorinated coating[63–65]

† Not a generally accepted classification, but some studies have used this terminology.

1.2.3 Contact Angle Hysteresis

While hydrophobicity is commonly used as a reference to the ability of a surface to resist wetting, this description is insufficient to convey the mobility of a droplet on the surface. Static contact angle only provides a snapshot of the surface and is rarely representative of actual use. All surfaces have some variation across the surface in homogeneity and roughness which can create small variations in the contact angle at different points on the surface.[66,67] This variation can make it exceedingly difficult to measure a consistent static contact angle as a droplet can take on multiple equilibrium contact angles on the same surface, caused by metastable states where it can be locally pinned.[68]

In most applications, the shedding ability of a liquid is far more important than the static wetting angle, which is why contact angle hysteresis is a much better measurement for a surface. To obtain the contact angle hysteresis, the dynamic contact angles can be collected for when the liquid is advancing and receding from the surface, as shown in **Figure 1.3**. One method of measuring the dynamic contact angles is to tilt a surface just until a droplet of liquid starts moving across it, then measuring the contact angle at the forward and aft edges of motion, corresponding to the advancing and receding contact angles. The method utilized herein is by use of the sessile drop technique.[69] A drop suspended from a syringe and the surface is brought up to contact with the drop. Liquid is then added to the drop so as to expand the drop and progress the 3-phase contact line forward. When the contact line is moving at a constant contact angle, the angle is measured; this is the advancing contact angle (θ_{adv}). The liquid is then slowly withdrawn back into the syringe so that the contact line moves inward, and the angle is measured when it is constant; this is the receding contact angle (θ_{rec}). The contact angle hysteresis ($\Delta\theta$) can then be determined by the difference in the advancing and receding contact angles ($\Delta\theta = \theta_{adv\,-}\,\theta_{rec}$). The relationship between these angles is complex and will be examined later in this thesis. The hysteresis, though, is directly representative of the mobility of a liquid on a surface, so although a surface may present as "-philic", it could still easily shed liquid depending on the hysteresis. Since hysteresis is so closely related to how a liquid interacts on a surface, we will report dynamic contact angles throughout this thesis as the dynamic contact angles can provide insight into both the wetting behavior and the mobility behavior of a liquid.

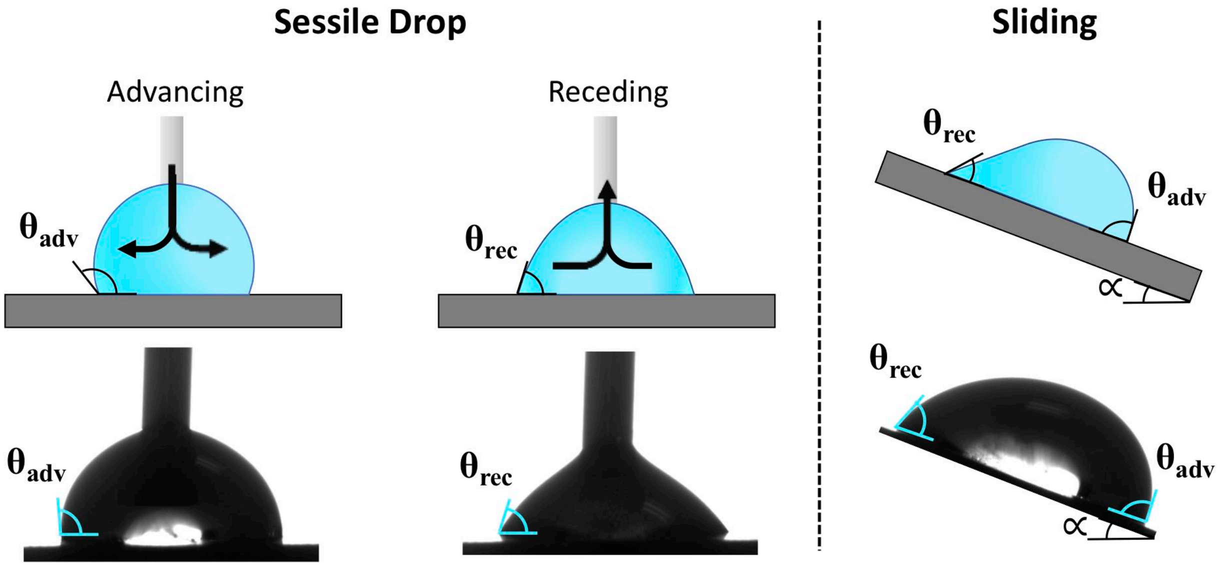

Figure 1.3: Methods for measuring the dynamic contact angles on most substrates. The sessile drop technique utilizes a syringe to expand and contract a drop, thereby moving the contact line outward and inward, respectively, to obtain the advancing and receding contact angles. A droplet sliding on an inclined surface can also be used to obtain the same angles. Both of these methods are depicted (top) with corresponding images of actual droplets being measured (bottom).

1.3 Textured Surfaces

Up to this point, all wettability classifications have been under the assumption of a smooth surface. Any surface roughness or texturing will change the wetting characteristics of any surface, and the contact angle will take on an apparent contact angle θ*, dependent on the wetting state. **Figure 1.4** displays the two distinct states of wetting on a textured surface that a liquid can take on: Wenzel state in which the texture is fully wetted, and the Cassie-Baxter state in which air pockets are entrapped underneath the liquid.

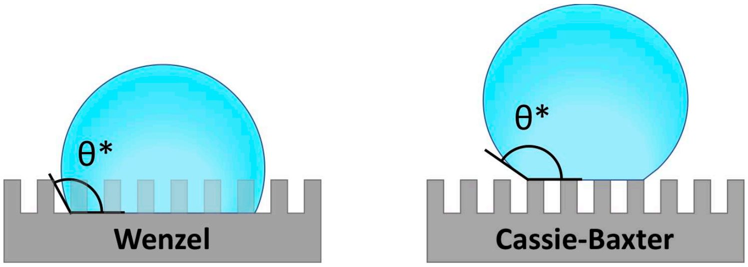

Figure 1.4: There are two possible wetting states for a liquid on a textured surface. The Wenzel state, in which the liquid fully penetrates the texture, or the Cassie-Baxter state in which the liquid rests on top of the texture with composite surface underneath from the entrapped air pockets.

1.3.1 Textured Surface Creation

There are a variety of methods employed to create surface texture, most employ some type of removal of a substrate to get the desired surface geometry. Some of the simplest manners involve randomly etching the surface whether by an acid or base etch[2,9], laser etching[70], or plasma etching[71]. In order to achieve omniphobic surfaces, it requires systematically etching the substrate in a specific manner to get a pattern, typically with reentrant features; this etching is typically done using photolithography techniques with plasma etching.[63,72,73] Lastly, porous surfaces can be created (either additively or through etching) to create texture.[74,75] After the surface texturing, most of these surface undergo a treatment, typically a perfluorinated coating, to reduce the surface energy to produce the desired wetting state below.

1.3.2 Wenzel Wetting State

The first study on the effect of textural roughness and its influence on wetting was conducted by Wenzel, hence the term Wenzel state.[76] The Wenzel equation relates that the apparent contact angle of a surface (θ^*) will vary according to the intrinsic contact angle (θ_E) and the roughness (r).

$$\cos\theta^* = r\cos\theta_E \tag{1.2}$$

In essence, this equation says that a “-philic” surface will become more “-philic” (ie apparent contact angle will be lower than the intrinsic contact angle) with roughness, and a “-phobic” surface will become more “-phobic” (ie apparent contact angle will be higher than the intrinsic contact angle) with roughness. However, because the liquid is wetting the roughness, as r increases, the solid-liquid contact area will also increase in area which creates more pinning points for the liquid. It would then follow, that the hysteresis (Δθ) will inevitably increase on any Wenzel wetted surface. Generally, a Wenzel wetted liquid is immobile from the surface as $\theta_{rec} \rightarrow 0°$.

1.3.3 Cassie-Baxter Wetting State

As the texture increases in roughness and/or the surface energy decreases from a Wenzel state, the surface eventually reaches a point in which microscopic air pockets can be trapped under the liquid. This state of composite wetting (partially wetting the surface, partially wetting the air pockets) is called a Cassie-Baxter state.[77] In this wetting state, the apparent contact angle is always above 150° and is in essence and average of the contact angle on the wetted surface and the air pockets (inherent contact angle of 180°). The generic form of this equation is the weighted average of these contact angles and the surface area of that contact angle:[78]

$$\cos\theta^* = \sum r_i \phi_i \cos\theta_i \tag{1.3}$$

The term ϕ refers to the areal fraction of the total contact area. Since a droplet in air reverts to a sphere (θ = 180°) to minimize surface area, and the cos(180°) = -1, this equation can be simplified as follows:

$$\cos\theta^* = r_\phi \phi_s \cos\theta_E + (1 - \phi_s)\cos 180° \tag{1.4}$$

$$\cos\theta^* = r_\phi \phi_s \cos\theta_E + \phi_s - 1 \tag{1.5}$$

Where the term r_ϕ is the same roughness term used in the Wenzel equation, the wetted area in proportion to the total projected area. As such, there is a crossover point of the intrinsic contact angle (θ_E) at which there is a critical contact angle (θ_c) in which a liquid will transition from a Wenzel wetting state to a Cassie-Baxter state. This transition is associated with a minimum energy configuration, and if done spontaneously, can result in the release of excess energy due to the reduction in surface area.[79]

1.4 Heat Transfer During Phase Transformation

As mentioned above, the enthalpy of vaporization of water is about 500x greater than the enthalpy associated with changing water by 1°C. This presents an opportunity to transport significant amounts of thermal energy with a minimal temperature change. Being able to harness the most efficient method of phase transformation has been sought after for decades with significant progress, but still limited by the applicability. One of the largest inhibitors of heat transfer is with insulating films, and when the opposing state of the liquid covers the surface it acts as a large resistance.[80] Thereby the challenge with heat transfer has been in both enhancing the heat transfer properties, while also inhibiting the resistive films forming.

1.4.1 Condensation Heat Transfer

Condensation heat transfer is predicated on the nucleation, growth, and departure of droplets from a surface, forming from a vapor rich atmosphere. The heat transfer performance of a surface is dependent on this cyclic behavior of the droplets and is averaged across the surface and displayed in a heat curve, analogous to the one shown in **Figure 1.5**. The onset of droplets nucleating sees a sudden increase in heat flux (q'') as the surface shifts from pure convection heat transfer to phase transformation heat transfer, once the surface temperature is depressed enough to overcome the energetic barrier ($\Delta T = T_{vapor} - T_{surface}$). As droplets nucleate, grow, and depart individually, referred to as the dropwise condensation region, the heat transfer coefficient (HTC) can be determined by q''/ΔT. Eventually the surface reaches a critical heat flux (CHF) point at which droplets form much faster than the rate at which they can depart, and the condensate forms a film over the surface, referred to as the filmwise condensation region. This transition is associated with up to a 3-fold decrease in heat transfer coefficient.[81] Condensate has a low thermal conductivity, so a film of water insulates the surface and reduces the surfaces ability to transfer heat efficiently.[82] The objective of any enhanced condensation surface is to maximize the heat transfer coefficient and delay the critical heat flux to be as high as possible.

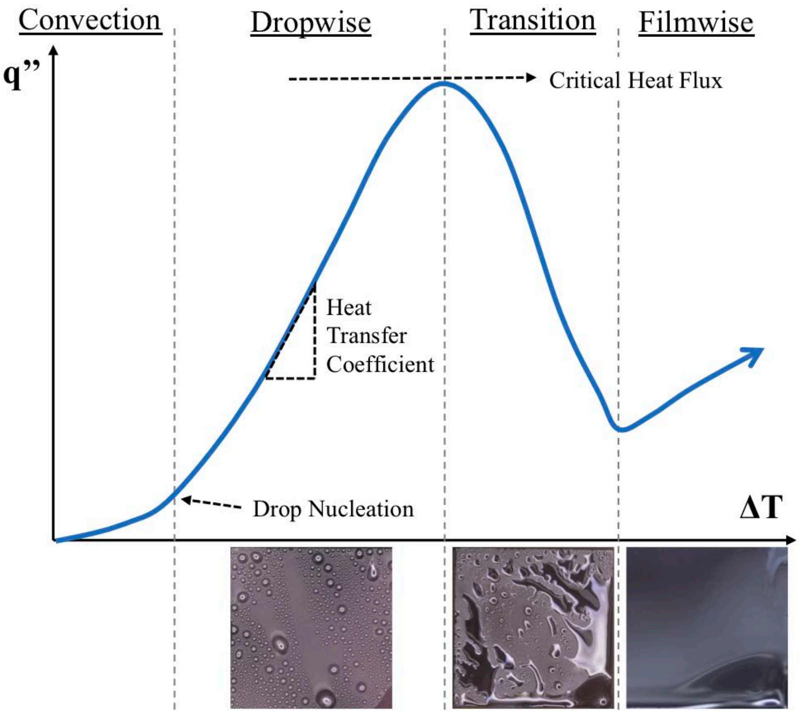

Figure 1.5: Schematic of a condensation heat curve plotted with heat flux (q'') on the vertical axis and surface subcooling (ΔT) on the horizontal axis. The plot can be divided into 4 distinct regions with images of condensation in these regions shown below the plot: Convection in which no condensation is occurring; Dropwise Condensation in which droplets nucleate, grow and depart the surface individually; Transition region where droplets begin to coalesce and form a film in regions of the surface; Filmwise condensation where a film on condensate completely cover the surface. From a plot like this, several heat transfer properties can be inferred. The subcooling temperature at which droplet nucleation begins is shown by a sudden increase in heat transfer at low subcooling. The heat transfer coefficient (HTC) can be determined by the average slope of the curve in the dropwise nucleation region. The critical heat flux is the highest heat flux achievable in the dropwise region before droplets start to coalesce and form a film. Figure adapted from Nature Review.[83]

In a saturated or sub-saturated atmosphere, the vapor and liquid phases are in equilibrium so condensation will not occur spontaneously; an energetic driving force for condensation to occur on a surface is created by a subcooling of the surface, below the vapor temperature. While the scientific community is still undecided on the mechanism of condensation, whether it is droplets nucleating on the surface or unstable, thin films of liquid breaking up, there is consensus that it is driven by heterogeneous nucleation.[84–86] The energetic driving force that initiates heterogeneous condensation is highly dependent on the wetting properties of the liquid and the surface on which condensation will occur. Heterogeneous nucleation is dependent on the Gibbs free energy associated with creating a nucleus on the surface which varies directly with the contact angle such that:[87]

$$\Delta G_{heterogeneous} = \phi \Delta G_{homogeneous} \tag{1.6}$$

$$\text{where } \phi = \frac{1}{4}(2 - 2\cos\theta_E - \cos\theta_E \sin^2\theta_E) \tag{1.7}$$

The Gibbs free energy of homogeneous nucleation is the least energetically favored mechanism of nucleation as this would be analogous to a drop of water spontaneously nucleating in the vapor, suspended in space. The factor ϕ varies from 0 to 1 as the contact angle (θ_E) varies from 0° to 180°, such that the Gibbs free energy barrier is negligible on a superhydrophilic surface ($\theta_E = 0°$). Thereby as a surface becomes more hydrophobic, the energetic barrier for condensation becomes increasingly more difficult to initiate nucleation. Since the heat transfer coefficient is dependent on the rate at which droplets can be formed, a decrease in contact angle should lead to an increase in heat transfer coefficient.

Droplet nucleation begins at very small sizes, on the scale of just a few nanometers in diameter. Given this small size, nucleation sites are essentially independent of the macroscale roughness because any surface is smooth on this size scale.[88] Due to the higher enthalpy of vaporization compared to specific heat, the HTC is directly related to the rate at which droplets nucleate and depart the surface. As the droplets grow on the surface, the resistance of the condensate inhibits heat transfer. At sufficiently small radii (less than a few hundred nanometers), the resistance through the surface dominates and limits the heat flux, but as the droplet grows larger, the resistance through the liquid dominates.[89] Therefore, the residence time of a droplet on the surface is so significant because the longer a droplet remains on the surface, the larger it gets, and the more it inhibits heat transfer.

Departure of droplets has been the primary focus to enhance condensation and this has been done through a variety of mechanisms. Passive departure of droplets has been limited; much of the work has focused on using very low surface energy, highly fluorinated self-assembled monolayers.[57,90] While this can be paired with a pattern of hydrophilic regions to enhance nucleation, these are still reliant on the low surface energy, hydrophobic regions for depature.[91,92] There are also active methods used to assist in droplet departure, these can include from sweeping arms, ultrasonic sound, and vibrations to assist in droplet removal from the surface.[93,94]

Lastly is the use of textured surfaces. While it may seem logical that a superhydrophobic surface would be exceptional with enhancing droplet departure, this is generally not true for condensation. Superhydrophobic surfaces rely on the Cassie-Baxter state such that the droplet needs to be suspended above the surface texture with air gaps under the interface. Due to the nanoscale size of the droplets as they nucleate, the droplets form within the surface structure and then as they grow, they grow in the Wenzel wetting state, pinning the droplets to the surface and preventing departure.[95,96] There have been a few notable exceptions to this. The first is to infuse the texturing with a non-volatile lubricating oil; as condensate droplets form, they form on top of the lubricant and they can easily run off.[10,56,97,98] At sufficiently low heat fluxes, surface texturing that has been treated with a low surface energy coating, have displayed jumping behavior in the droplets.[11] This behavior is caused by the release of excess surface energy by the coalescence of droplets.[99] The excess surface energy is converted into kinetic energy, causing the droplet to break the adhesive force with the substrate and depart from the surface. As the heat flux increases, though, and the rate of condensation increases, the droplets cannot depart the surface quickly enough and eventually begin to coalesce in the Wenzel state.[100]

1.4.2 Boiling Heat Transfer

Similar to condensation, boiling heat transfer is predicated on the nucleation, growth, and departure of vapor bubbles from the surface to transfer heat from the surface to a liquid. The heat transfer performance of a surface is an average of the cyclic behavior of the bubbles on the surface as displayed in **Figure 1.6**. The incipience of nucleate boiling is defined by the sudden increase in heat flux (q''), typically at low superheating ($\Delta T = T_{surface} - T_{vaporization}$). The bubbles then continue to nucleate, grow, and depart from the surface, referred to as the nucleate boiling region. Eventually, the surface reaches a high enough temperature that the liquid cannot rewet it and a film of vapor forms over the surface. This point can go by different names, most commonly referred to as the critical heat flux (CHF) or departure from nucleate boiling (DNB) and is very sudden, with minimal to no transition region. Just as in condensation, the heat transfer coefficient (HTC) is measured in the nucleate region by q''/ΔT. Once film boiling occurs, surface experiences is sudden increase in temperature. The far less efficient film boiling regime requires a superheat many hundreds of degrees, Celsius, higher than that of a similar heat flux achievable in the nucleate boiling regime, at just a few degrees superheat.[101] The utility of a high efficiency boiling surface, especially in use for power production, is predicated on increasing the HTC while delaying the CHF to as high of a surface superheat as possible

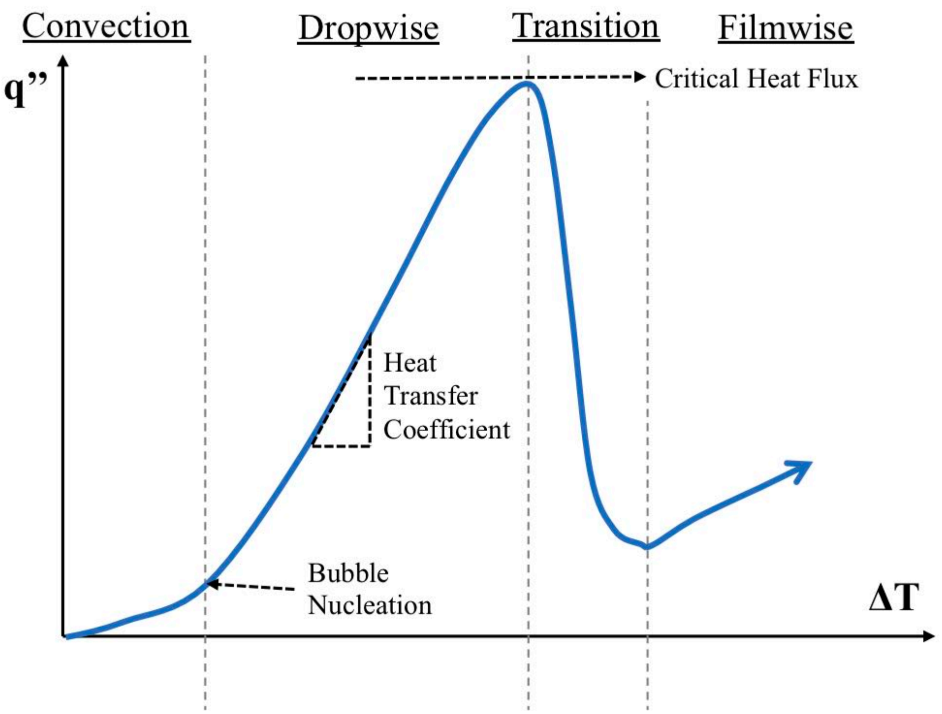

Figure 1.6: Schematic of a boiling heat curve plotted with heat flux (q'') on the vertical axis and surface superheat (ΔT) on the horizontal axis. The plot can be divided into 4 distinct regions with images of boiling in these regions shown below the plot: Convection in which no boiling is occurring; Nucleate Boiling in which bubbles nucleate, grow, and depart the surface individually; Transition region where bubbles begin to coalesce and form a vapor layer in regions of the surface; Filmwise boiling where a film on vapor completely covers the surface. From a plot like this, several heat transfer properties can be inferred. The initiation of nucleate boiling where bubbles begin to form on the surface. The heat transfer coefficient (HTC) can be determined by the average slope of the curve in the nucleate boiling region. The critical heat flux is the highest heat flux achievable in the nucleate region before bubbles start to coalesce and form a film. Figure adapted from Nature Review.[83]

Just as in condensation, the energy barrier to initiate bubble nucleation is dependent on the wetting properties of the liquid on the surface. The Gibbs free energy associated with nucleating a bubble varies with the contact angle such that:[102]

$$\Delta G_{heterogeneous} = \phi \Delta G_{homogeneous} \tag{1.8}$$

$$\text{where } \phi = \frac{2+2\cos\theta_E+\cos\theta_E\sin^2\theta_E}{4} \tag{1.9}$$

Again, heterogeneous nucleation is favored over a bubble spontaneously nucleating in the bulk liquid (homogeneous nucleation). Unlike condensation, though, the factor ϕ varies inversely for boiling, in that it varies from 0 to 1 as the contact angle varies from 180° to 0° respectively. Thereby, as a surface becomes more hydrophobic, the energy barrier to nucleate a bubble decreases. Since the heat transfer coefficient is dependent on the rate of nucleating bubbles, a higher contact angle leads to a higher HTC. This works counter to the critical heat flux, though, as a lower contact angle increases the ability of the liquid to wet the surface and therefore increases the critical heat flux.

The behavior of bubbles nucleating is not entirely dependent on the contact angle. Given Gibbs free energy barrier for bubbles to nucleate, incipience of nucleate boiling on a Teflon surface should theoretically not initiate until a surface superheat of about 188°C, at standard atmospheric conditions.[103] We know this not to be true from just observing boiling water in a kitchen, bubbles during boiling commence at a significantly lower superheat. Rather than pure heterogeneous nucleation on the surface, surfaces facilitate the nucleation of bubbles from gas and vapor trapped within the pits and cavities on a surface.[104] These trapped pockets significantly reduce the activation energy required to nucleate a bubble. Significant progress has been made to increase the HTC of boiling surfaces by adding increasingly complex geometries which further enhance the number of nucleation sites. Despite the enhancement by trapped vapor, there is still a correlation between the number of active nucleation sites on a rough surface that relates to the contact angle.[105] Furthermore, the significance of surface texturing on the HTC is not fully understood as the increased complexity has led to inherent randomness that cannot be modeled, though there has been some evidence that most of the HTC enhancement is caused simply by the increased wetted surface area of textured surfaces.[12,106]

The other important design consideration is the critical heat flux; delaying the CHF is important to operate at high heat fluxes without the extreme temperatures inherent with film boiling. In addition to analysis of the Gibbs free energy barrier, critical heat flux has been experimentally proven to decrease with increasing contact angle.[107] The CHF can be enhanced with surface texturing, though the exact mechanism by which texture prevents a vapor film from forming, is still unclear. The current theory is that the texturing allows for capillary wicking such that the surface can more easily resupply and wet with liquid, thereby maintaining attachment of the liquid to the surface for longer.[108–110]

Despite these improvements, much of the prior boiling heat transfer enhancements have been achieved through use of surface roughness and texturing. This presents problems in that it is difficult to understand the exact mechanism of enhancement which leads to difficulty in modeling and predicting the behavior of both the heat transfer coefficient and critical heat flux.

1.4.3 Frost Formation and Icing

There is a wide variety of phase changes towards the solid phase for a variety of liquids; this work will examine specifically the freezing of water. Although we don't specifically measure heat transfer, frost formation is an inhibitor of heat transfer as it forms an insulating layer, akin to the liquid insulating film in condensation and vapor insulating film in boiling. Preventing this frost layer has significant implications in efficiency of refrigeration systems, reducing energy use in air ducts, and increasing safety in numerous industrial applications.[111–113] Prevention of this undesired ice formation on a multitude of surfaces is the focus of this work.

Just as with condensation and boiling, the spontaneous nucleation of ice crystals is extremely unlikely. Homogeneous nucleation requires a significant thermodynamic driving force and can only occur under specific conditions when the instantaneous alignment of temporary hydrogen bonds align and form a seed crystal. Heterogeneous nucleation is far more likely and is relevant in most practical situations. Again, heterogeneous nucleation induces a lower free energy barrier for nucleation which can be represented, similar to boiling and condensation:[114]

$$\Delta G_{heterogeneous} = \phi \Delta G_{homogeneous} \tag{1.10}$$

$$\text{where } \phi = \frac{2 - 3\cos\theta_E + \cos^3\theta_E}{4} \tag{1.11}$$

Similar to condensation, the factor ϕ varies from 0 to 1 as the contact angle varies from 0° to 180°, leading to a direction in that more hydrophilic surfaces nucleate ice easier, whereas a highly superhydrophobic surface (θ_E = 180°) requires the same nucleation energy as homogeneous nucleation.

Several different methods have been attempted to prevent ice and frost formation on surfaces. Logically, the first direction was to utilize hydrophobic and superhydrophobic surfaces as the high contact angle should prevent nucleation. Superhydrophobic showed initial success in elongating icing time of water on a surface, but this was due to the reduced heat transfer from the liquid into the surface, a result of the composite interface since the liquid was in a Cassie-Baxter wetting state.[115] These surfaces suffered from poor durability as the surface texturing was easily damaged by departing ice, exposing high surface energy material, and causing a Wenzel wetting state.[116] Furthermore, the surfaces did not prove to be anti-frosting because they were susceptible to contamination from dust and other particles. These particles acted as nucleation points for ice to form, and once any ice or water is present, these points act as growth platforms since water has an effective 0° contact angle on water or ice.[117]

The discovery of surface contamination leading to enhanced frost formation led to the use to materials that could suppress ice formation. Anti-freeze proteins (AFPs) were first discovered in polar fish that could survive in sub-freezing conditions.[118,119] Applying similar proteins to a surface was shown to prevent ice growth by bonding to the crystal face of the ice and preventing propagation of the crystal.[120] This was significant because even if a surface was contaminated and ice began to nucleate, the proteins could prevent the ice from propagating.[121] A similar focus of suppressing ice formation as AFPs has been the use of ions to reduce the freezing temperature of water such that it will not freeze on the surface but remain in the liquid state. Various hydrogels and polyelectrolyte brushes have been created that can hold ions within the bulk.[122–124] These materials have ions that can be exchanged for ions with lower freezing temperatures; once water diffuses into the surface, the ions suppress the ice formation temperature and the water remains in the liquid state.[125]

1.5 Research Overview

There have been numerous studies on a wide array of mechanisms to control and optimize phase transformation surfaces. However, all of these studies can be categorized as failing it at least one of the following areas: optimization for heat transfer performance, durability and long-term longevity, and/or facile and easily scalable. This dissertation is divided into 4 chapters, each addressing the performance of a surface during either condensation, boiling, or ice/frost deposition.

In chapter 2, we identify the design criteria necessary to maximize the heat transfer coefficient and enhance performance for condensation heat transfer on a smooth surface. By utilizing mildly hygrophilic surface energy combined with very low contact angle hysteresis enabled by thin, amorphous films, we demonstrate an enhancement over traditional technologies using high contact angle coatings. We are also the first study to demonstrate dropwise condensation improvements on hydrophilic surfaces and maintain dropwise condensation on the lowest contact angle surface (30°). These amorphous surfaces also demonstrated exceptional longevity and durability with negligible degradation after extended use and mechanical abrasion.

Chapter 3 addresses boiling heat transfer and focuses specifically on smooth surfaces whereas prior studies have focused on textured surfaces. Textured surfaces face economic and logistical difficulty when considering the scale up to industrial use cases, and investigations of smooth surface coatings have been sparce due to the temperature degradation of boiling surfaces. We create a diamond-like carbon (DLC) doped with silicon, which is the first, high temperature stable boiling surface that simultaneously enhances both heat transfer coefficient and critical heat flux. The silicon stabilizes the film at high temperatures and increases the contact angle which enhances the heat transfer coefficient. The smoothness of the film reduces the contact angle hysteresis and enables an enhancement in the critical heat flux. This diamond-like carbon surface also exhibits exceptional durability and shows little affect by harsh mechanical abrasion. We continue the use of DLC for boiling in chapter 5 with a fluorine doped DLC that maintains a superhydrophobic Cassie-Baxter wetting state above 500°C, higher than any silane modified superhydrophobic surface. This is particularly valuable for high heat flux boiling applications, like electronics cooling, in which a similar degree of cooling can be achieved at 20°C lower temperature compared to an uncoated surface. The fluorinated DLC maintains its superhydrophobicity in harsh boiling environments allowing for an HTC enhancement of 120% with a minor reduction in CHF.

Lastly, chapter 4 examines the icing and frosting properties of surfaces in which we develop a coating that delays frost formation on a surface by over 2000%. Poly-zwitterionics have the ability to strongly bind water in a non-freezing state within a network. We develop a network of 2-(Methacryloyloxy)ethyl-dimethyl-(3-sulfopropyl)ammonium hydroxide (SBMA) that inhibits frost formation and delays icing of liquid water on the surface. The coating is easily produced and can be scaled by thickness to each specific use case. We also demonstrate superior performance over prior technologies when compared in identical environmental conditions.

In this dissertation, we address all three phase transformations of liquids and identify design criteria to enhance the desirable performance characteristics of a surface for each phase transformation. We also apply the design criteria and create surfaces that demonstrate the desired performance enhancements. Lastly, many of the surfaces exhibited superior longevity of use and mechanical durability, especially when compared to prior published technologies.

Chapter 2

Durable, Amorphous Polymer Brushes for Enhanced Condensation Heat Transfer

This chapter is primarily adapted from a first-author article submitted to *Advanced Materials.*

2.1 Introduction

As discussed in the introduction, condensation heat transfer is a highly effective mechanism for removing energy from a system. Condensation is used across a breadth of industrial settings, some of which are the largest energy consumers in the world, like oil refining, water distillation, power generation, and refrigeration.[126–129] Improving the heat transfer properties for condensation by just 10% has the potential to reduce energy consumption by up to 4% if implemented in the processes above. This enables increased output, smaller and cheaper equipment, and significant cost and energy savings.[130]

Condensation can take on two distinct modes, dropwise condensation (DWC) and filmwise condensation (FWC). Dropwise condensation is far preferred due to the lower energy requirement and increased heat transfer rate, though filmwise condensation is nearly ubiquitous in commercial operations for cost and durability considerations. The two key design parameters for any condensation surface are balancing the high heat transfer rates during dropwise condensation while preventing the critical heat flux, or transition from dropwise to filmwise.

The performance of a surface during dropwise condensation is predicated on the rate at which droplets can form (nucleation rate) and the rate at which droplets depart (shedding rate); increasing both of these factors, increases the heat transfer and prevents the CHF. As mentioned in the introduction, the nucleation rate is directly associated with the contact angle through the Gibbs free energy of nucleation, but liquids have a tendency to "stick" to more hygrophilic surfaces. The Kim and Kim model combines these factors to account for the nucleation rate and the shedding rate.[131]

Prior work can be categorized into three mechanisms to promote dropwise condensation: low surface energy smooth films, superhydrophobic texturing, and lubricant infused surfaces (LIS). Surfaces like hydrophobic waxes, PTFE, and omniphobic self-assembled monolayers were first used to enhance dropwise condensation. By maintaining a high contact angle, droplets had reduced contact area with the surface and could easily run off. This promoted a high shedding rate but suffered from poor nucleation due to the high Gibbs free energy barrier.[11,132,133] Soon after discovery, lubricant infused surfaces were quickly used for condensation, with the initial surfaces merely proving out that a droplet could condense and roll off the surface without wetting the underlying texturing.[10,97,134,135] Even with enhancements in texturing and lubricant to minimize shedding of the lubricant and improve heat transfer, LIS has always suffered from poor durability.[56,98,136] This degradation of the lubricant layer is caused by cloaking, in which a thin film of lubricant sits on top of every droplet and runs off the surface when the droplet departs, means that LIS can only sustain dropwise condensation for a few minutes to hours.[137–140] Lastly, superhydrophobic surfaces have shown a unique ability to remove droplets from the surface when the droplets coalesce due to the reduction in surface energy being converted to kinetic energy.[11] While successful at enhancing heat transfer coefficient for a low heat flux, once the subcooling exceeds just a few degrees, the nanotexture wets and droplets continue forming in the Wenzel state.[141]

Here, I report the design and fabrication of a solid, smooth coating that enhances condensation heat transfer for a variety of liquids with different surface tensions. These coatings exhibit mechanical durability and use longevity in excess of 200 hours. Through a thermodynamic and polymer analysis, I report the first stable, dropwise condensation on hygrophilic surfaces through a combination of moderate contact angle, low hysteresis, and ultra-low glass transition temperature.

2.2 Design Criteria for Condensation

There are numerous design considerations that go into a condensation surface for heat transfer. Many of these considerations can be derived from the modeling that has been done to predict the heat transfer properties of a variety of surfaces. One of the most notable and widely used models is the Kim and Kim model which accounts for a variety of factors including the droplet distribution, droplet sizes, conductivity of the surface, liquid and vapor thermodynamic properties[131]. Utilizing this model, with additional analysis and interpretation, I have created a set of design criteria that can be utilized to maximize the condensation heat transfer properties for any surface and condensate combination.

An ideal condensing surface for enhanced heat transfer performance would be a self-assembled monolayer that is polymer based with a glass transition temperature far below the ambient temperature and a moderate surface energy such that the contact angle for the target condensate is mildly hygrophilic. The following describes the design rationale for each of these parameters and the considerations taken to get to this conclusion.

2.2.1 Resistance

Resistance plays two critical roles in heat transfer during condensation, the first is in consideration of the surface coating. Every material has a thermal conductivity, or the ability to transfer thermal energy through its bulk. A smaller conductivity means that there is a large temperature drop across a material for a given heat flux. For condensation, the performance of a surface is quantified by the heat flux achieved at a given subcooling (ΔT). If there is a large temperature drop across the coating layer, then the temperature at the surface of the coating will be higher than the substrate temperature.[142] Since the nucleation rate is directly related to the surface temperature, the heat flux would therefore be lower with a coating compared to the uncoated substrate (if all other properties were the same). This can be mitigated by utilizing thermally conductive and/or very thin coatings. If the conductivity is large enough, the temperature drop through the coating becomes negligible and the surface of the coating has essentially the same temperature as the surface of the substrate. Reducing the thickness has a similar effect; since conductivity is kW m^{-1} K^{-1}, the temperature drop across a material is dependent on the thickness of the material. Reducing the thickness to be very small again minimizes the temperature drop to a point that it is negligible. This trade-off was modeled by Kim and Kim and is shown in **Figure 2.1**. Any coating that will enhance condensation heat transfer must minimize the effect of resistance in the coating either through minimal thickness or increased conductivity.

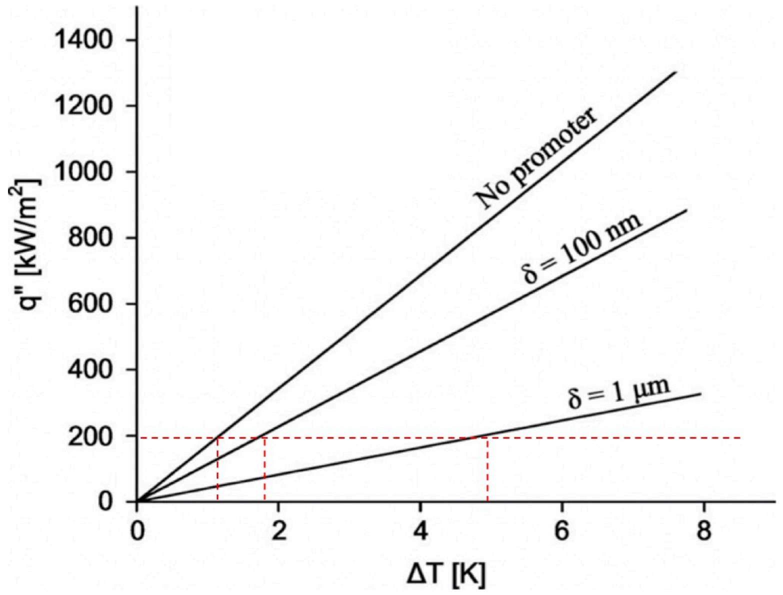

Figure 2.1: Heat flux versus vapor subcooling for different thickness of a coating layer. As the thickness increases, the temperature drop across the coating increases which reduces the net heat flux. For example, at a heat flux of 200 kW m^{-2}, there is about a 4°K temperature drop across a 1 μm coating, so the substrate would have to be cooled to 4°K cooler with the coating to achieve the same heat transfer performance as the bare substrate. This figure was adapted from the study by Kim and Kim with a coating conductivity of 0.2 W m^{-1} K^{-1}.[131]

To address the coating resistance, polymer based self-assembled monolayers were identified as ideal candidates. Since most unmodified, polymer-based coatings will have relatively low thermal conductivity, the best approach is to minimize the thickness; as seen in **Figure 2.1**, a one magnitude increase in thickness can lead to about a 300% reduction in heat transfer. Self-assembled monolayers (SAMs) are only a few nanometers thick, so the thermal conductivity becomes negligible. Take for example a 10 nm film of Teflon (k=0.25 W m^{-1} K^{-1}) at a heat flux of 250,000 W m^{-2}, the temperature drop across the Teflon would be just 0.08 K. Furthermore, wettability is only dependent on the surface, so it is unnecessary to have a bulk material with contributes to thermal losses but does not improve performance.

Liquid on the surface can also introduce resistance in a similar fashion as the coating above. If there is a layer of water covering the surface, as is present in filmwise condensation, additional vapor can only condense on the outside of the liquid film. Thus, there is a temperature drop across the thickness of the liquid film that reduces performance in a similar way. When a liquid film is present, the heat transfer is reduced 2-3 fold compared to dropwise condensation, and this is almost entirely due to the difference in condensing temperature between the coating surface temperature and the liquid surface temperature.[143] Even in dropwise condensation, though, the conductivity of the liquid and the resistance it induces is critical to the design of maximizing the performance. Heat flux is based on energy per unit area, the more exposed area on a surface, the greater the heat transfer. As droplets form, portions of the surface are covered by droplets which add an additional resistance to heat transfer, shown in **Figure 2.2.** Just as in filmwise condensation, this increased liquid resistance reduces the heat transfer performance due to a temperature drop across the droplet. Although this reduction in performance is isolated to the surface area covered by the individual droplet, when a surface is covered by many droplets, this becomes a more dominant factor.

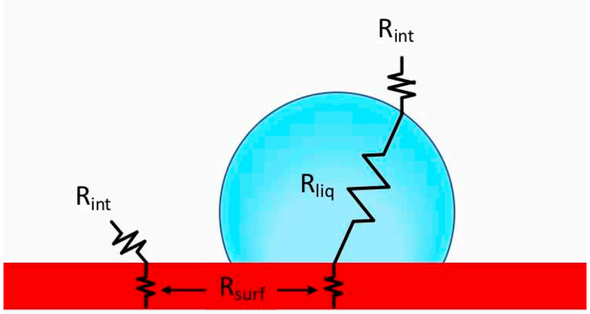

Figure 2.2: Resistance diagram of a condensing surface, both exposed and covered by a droplet. Droplets covering a surface can introduce significant resistance on the isolated area the droplet is covering.

Just as with the coating resistance, the liquid resistance should be minimized for maximum heat transfer performance. Since the conductivity of the liquid cannot be varied, the droplet size is the only factor that can control the liquid resistance. Minimizing the droplet size on the surface by enabling droplets to depart early and when they are small will reduce the effect of liquid resistance, and the method to do so is analyzed later in how to enable early departure of droplets.

2.2.2 Optimize Surface Energy for Condensation

As described in section 1.4.1, the Gibbs free energy for a droplet to nucleate will vary with the contact angle. The nucleation density on a surface will vary between 10^9-10^{15} m^{-2} and, although it cannot be directly modeled, is directly associated with the contact angle (i.e. the surface energy).[144] The nucleation density then relates to the heat flux since it is correlated with the volume of liquid being condensed, a greater nucleation density means more liquid condensing which leads to a higher heat flux. Logically, minimizing the contact angle would be the best way to maximize the heat transfer as that would maximize the nucleation density. As the contact angle decreases, though, the droplets on the surface cover more and more surface area for the same volume of droplet. When the droplets cover more of the surface, this increases the resistance across that cover portion of the surface as described above, and also leads to more droplets coalescing and spreading, increasing the likelihood of a liquid film forming (CHF). It turns out there is an ideal contact angle which balances the increased nucleation rate of a hygrophilic surface, with liquid repellence to prevent significant droplet spreading on the surface. This can be directly modeled, shown in

Figure 2.3, by the Kim and Kim model which predicts that there is a maximum heat transfer coefficient when the contact angle is between 40° and 80°. If the contact angle is higher than the maximum point, then the system is dominated by the rate of nucleation as the nucleation density decreases with increasing contact angle. If the contact angle is lower than the maximum point, then the system is dominated by the resistance of the droplets as they spread across the surface and inhibit heat transfer.

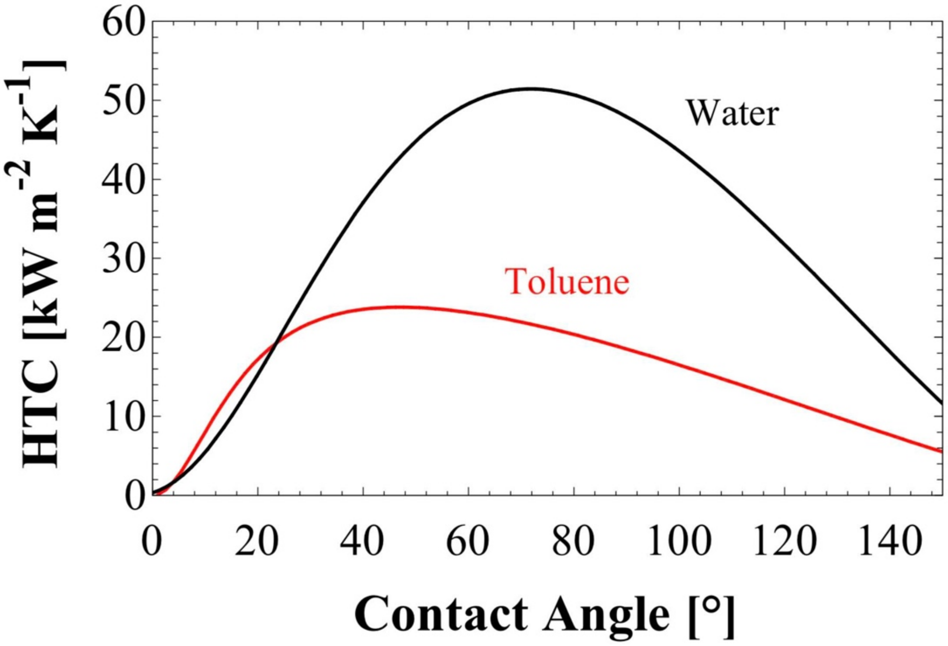

Figure 2.3: Numerical model of heat transfer coefficient (HTC) versus the contact angle for water and toluene. There exists a maximum heat transfer coefficient at a moderately hygrophilic contact angle (40° < θE < 80°). As the contact angle increases (to the right), the nucleation rate of the surface decreases which inhibits condensation. As the contact angle decreases (to the left), the droplets that nucleate, spread across the surface leading to increased resistance and increased coalescence. Plot created assuming a constant contact angle hysteresis of 10°.

There exists a range for the ideal contact angle since the condensate surface tension, condensate conductivity, and enthalpy of vaporization will all vary with different liquids. Typically, lower surface tension liquids have a lower ideal contact angle for condensation heat transfer. As the surface tension decreases, the departing droplet size decreases as well, as shown in **Figure 2.4**. When the droplets depart from the surface at smaller sizes, a surface can maintain a more efficient condensation mode, therefore with low surface tension liquids, the maximum heat transfer coefficient will occur at a slightly lower contact angle.

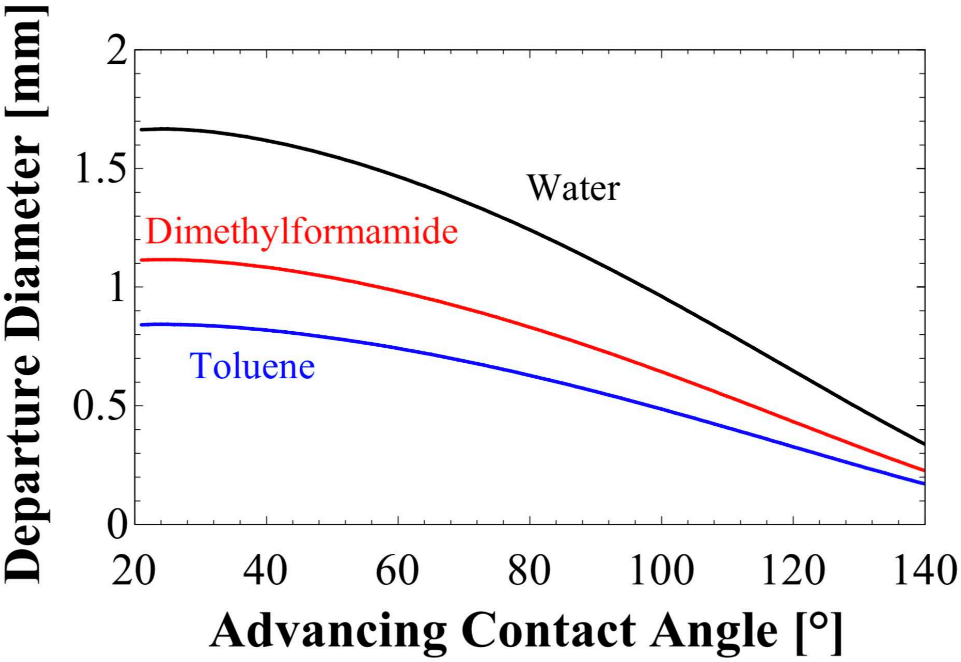

Figure 2.4: Prediction for the departure diameter of a droplet from a vertical surface versus contact angle for water, dimethylformamide, and toluene, liquids with decreasing surface tensions, respectively. As the surface tension decreases, the diameter at which a droplet will depart the surface gets smaller for a given apparent contact angle. Plot created assuming a constant contact angle hysteresis of 10°.

From this model, it is obviously that this classification of "moderately hygrophilic" surfaces would produce the maximum condensation heat transfer. Upon examination of prior condensation heat transfer work, this has not been pursued as prior work has focused on condensing on low surface energy (high contact angle) films.[57] Even lubricant infused surfaces utilize a fluorinated lubricant which gives a water contact angle of about 120°. Before this work, there was not any previously study that sustained dropwise condensation on a hydrophilic surface. Condensing on a surface with a contact angle $\theta_E < 90°$ typically results in the early onset of filmwise condensation as droplets would get pinned to the surface. The key to fulfilling this design criteria to have a moderate surface energy, is to enable early and facile departure of droplets from the surface to prevent them from coalescing.

2.2.3 Minimize Hysteresis for Early Departure

As described above, it is obvious that reducing the contact angle (increasing the surface energy) would produce a higher heat transfer coefficient for condensation, though previous studies have not developed such a surface. Simply increasing the surface energy, thereby decreasing the contact angle, is not sufficient to create efficient condensation. Typically, a reduced contact angle leads to droplets getting pinned to the surface and unable to slide off. This presents two problems in that droplets that grow too large before departing introduce increased thermal resistance, compounded by the fact that it is a hygrophilic surface so the droplet spreads and covers a large area. Further, delayed departure eventually causes droplets to coalesce leading to a liquid film forming. To properly utilize a hygrophilic surface and realize a heat transfer enhancement, the droplet departure must be addressed.

For this, we can turn to the Furmidge equation which shows that the force for a droplet to slide on an inclined (α) surface is related to the gravitational (g) force of the droplet:[145]

$$F_{slide} = m\, g \sin\alpha \tag{2.1}$$

$$F_{slide} = \gamma_{lv}(\cos\theta_{rec} - \cos\theta_{adv})2r \tag{2.2}$$

Since the mass (m) and radius (r) of the droplet are directly related, they can both be minimized by minimizing the difference of the cosines. This difference approaches zero as the difference between the advancing and receding contact angles, or the hysteresis (CAH = θ_{adv} - θ_{rec}), approaches zero. The influence of hysteresis for different advancing contact angles is shown in **Figure 2.5**. From this, one can identify that as the hysteresis approaches zero, the advancing contact angle becomes nearly negligible. That is to say that the surface energy becomes irrelevant to the departure behavior of droplets if the hysteresis is minimized. Analysis of this also directs that if the hysteresis can be reduced to less than 8°, the departure diameter of a droplet will be about 1mm, regardless of advancing contact angle.

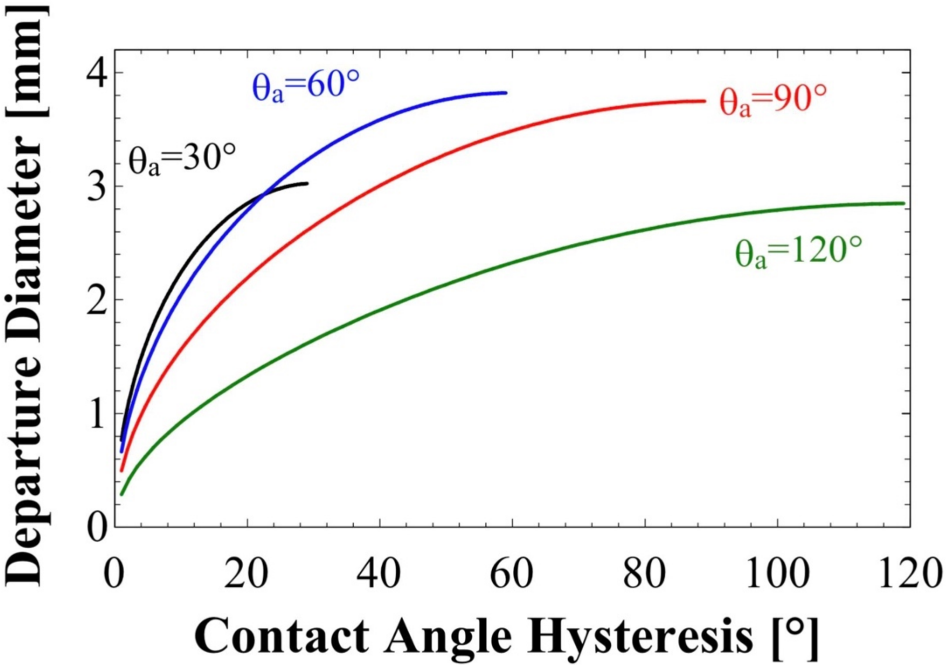

Figure 2.5: Estimated departure diameter for a droplet on a vertical surface versus the contact angle hysteresis for a series of advancing contact angles (30°, 60°, 90°, and 120°). As the hysteresis gets sufficiently low, the droplets depart at essentially the same diameter.

This influence of hysteresis is also reflected when we compare the heat transfer coefficients on various surfaces in **Figure 2.6**. At very low hysteresis, when the departure becomes nearly independent of the contact angle, the highest surface energy displays the highest heat transfer coefficient, as would be expected as that surface would also have the highest nucleation density of droplets. This plot also displays the critical tradeoff with pursuing high surface energy surfaces in that the performance of them quickly drops off to well below hygrophobic surfaces with just a minor decrement in the hysteresis. It becomes obvious why so many studies were performed with low surface energy surfaces (high contact angle), because the hysteresis was nearly negligible and has little to no effect on the heat transfer coefficient as long as it is below 30° (CAH < 30°).

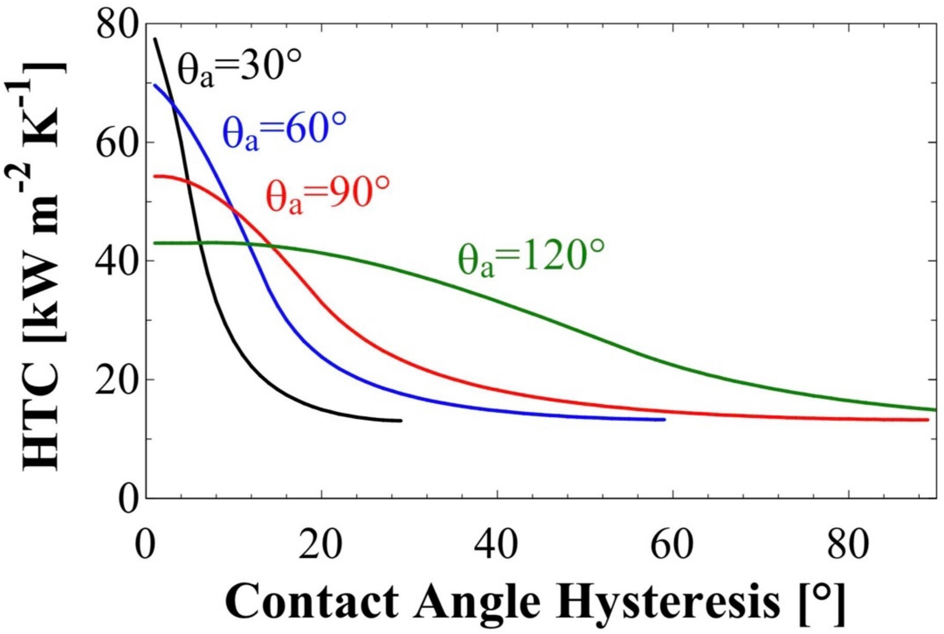

Figure 2.6: Numerical modeling comparing the estimated heat transfer coefficient (HTC) to the contact angle hysteresis with water for various advancing contact angles (30°, 60°, 90°, and 120°). When hysteresis approaches zero, the HTC of the system becomes highest with hydrophilic surfaces.

While contact angle hysteresis has always been a factor in the performance of condensing surfaces, it becomes far more critical in this study. Where previous studies utilized high contact angle surfaces, where hysteresis had little effect, with hygrophilic surfaces, the hysteresis must be kept to minimum to enhance performance. It is only through a reduction in hysteresis that hygrophilic surfaces can exceed the performance of hygrophobic surfaces but can also lead to an enhancement in heat transfer not previously shown before.

2.2.4 Tuned Glass Transition Temperature

As mentioned above, in order effectively develop these hygrophilic condensing surfaces, the hysteresis must be minimized. Two effective methods that have been clearly demonstrated previously has been by reducing surface roughness and maximizing surface homogeneity.[55,146] The hysteresis can be further reduced through use of liquid surfaces, which is the premise of lubricant infused surfaces. Along this line of thought, an amorphous surface exhibits properties similar to liquid surfaces and have been shown to further reduce surface defects and improve hysteresis with most liquids.[67,147,148] By controlling the glass transition temperature of a solid surface such that it is sufficiently low and is in an amorphous state, it will take on “liquid-like” behaviors at room temperature. Combining all of the above design parameters, an ideal condensation surface would be a polymer-based self-assembled monolayer that has a surface energy that is mildly hygrophilic for the target condensate and has a glass transition temperature significantly below the application temperature to produce an amorphous surface that is mobile, minimizing contact angle hysteresis.

2.2.5 Surfaces Identified to Conform to Design Parameters

Identified herein, are a set of polymer brushes that exhibit contact angles between 40° and 80° for the target liquid. They also have glass transition temperatures below -70°C such that they are amorphous and mobile at the testing conditions, >30°C. The three polymer brushes identified are polyethylene glycol [PEG-3], polydimethylsilozane [1,3 cPDMS], and perfluoropolyether [PFPE] based silanes that were selected by tuning the surface energy to be only marginally lower ($\Delta\gamma < 20$ mN m^{-1}) to obtain contact angles that will maximize heat transfer for water, dimethylformamide, and toluene. The resulting films are shown in **Table 2.1** with **Figure 2.3** and **Figure 2.6** overlaid with the corresponding properties of each film tested.

Table 2.1: Surface energy and glass transition temperature for each polymer brush along with dynamic contact angles for each condensate and surface combination. An additional fluorinated monolayer (F13Cl) is shown to be representative of a fully crystalline surface. Testing will also be performed on the crystalline fluorosilane. Note that contact angles for the low surface tension liquids are not shown for PEG-3 as they completely wet the surface.

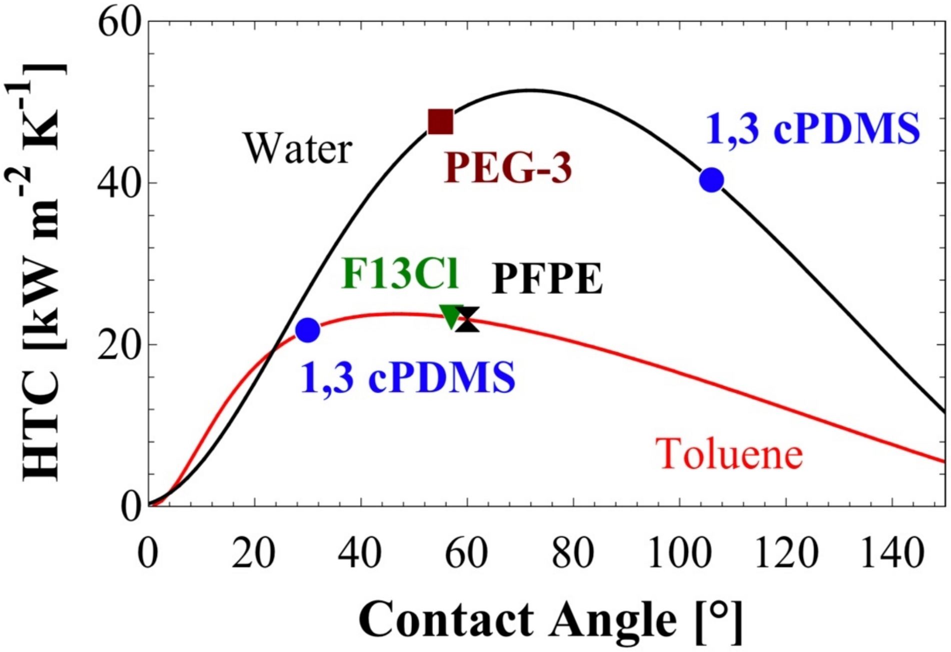

Figure 2.7: Modified version of Figure 2.3 with the contact angles of all coatings tested in this chapter overlayed on the graph for a visual representation of the expected improvement in HTC.

Surface Properties			Water (γ_{lv}=72.1)	Dimethyl-formamide (γ_{lv}=35.1)	Toluene (γ_{lv}=27.5)	Pentane (γ_{lv}=14.5)
Coating	**γ_{sv} (mN m^{-1})**	**T_g (°C)**	**θ_a/θ_r (°)**	**θ_a/θ_r (°)**	**θ_a/θ_r (°)**	**θ_a/θ_r (°)**
PEG-3	61.7	-70	52/45	--	--	--
1,3 cPDMS	25.1	-130	106/101	67/62	31/30	22/20
F13Cl	15.1	175	113/91	78/46	58/31	34/14
PFPE	14.8	-110	120/115	87/81	70/64	34/32

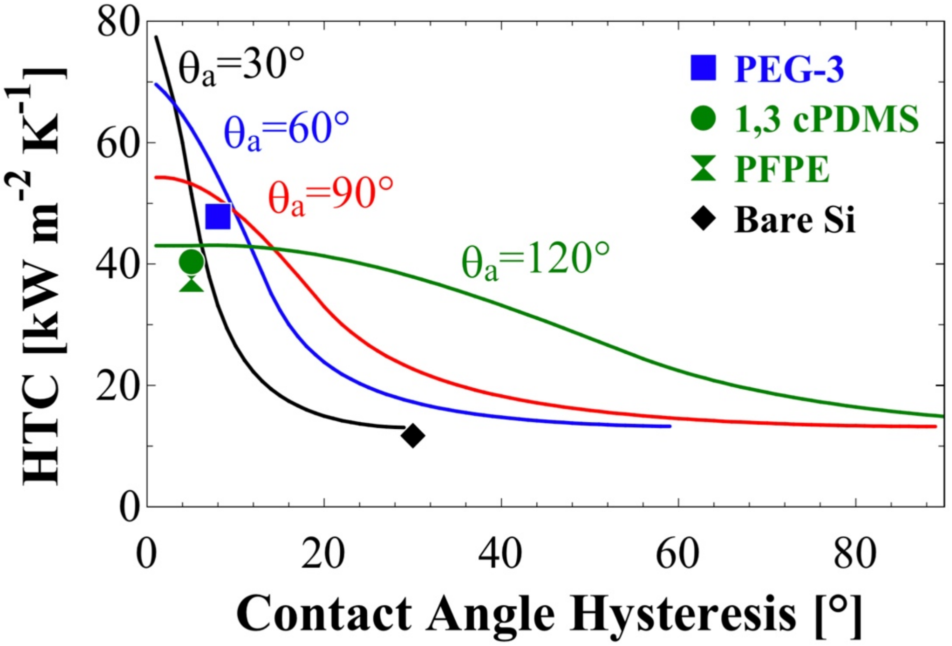

Figure 2.8: Modified version of **Figure 2.6** with the approximate advancing contact angle and contact angle hysteresis overlayed for all experiments run with water as the condensate. The results reported later in this chapter reflect a realized improvement utilizing the PEG-3 due to the lower contact angle.

2.3 Materials and Methods

2.3.1 Coating Deposition Processes

All coatings were self-assembled monolayer silanes that were deposited onto silicon wafers. Prior to silane deposition, the silicon was plasma cleaned for 20 minutes to activate the hydroxyl groups on the surface which subsequently reacted with the silane.

Materials

Silicon wafers (University Wafer test grade, 500 μm thickness, 1.5 nm native oxide layer, double sided polished <100> orientation) were used. On one side of the wafer, a 25 nm layer of NiCr followed by a 200 nm layer of copper were physical vapor deposited using a Cooke Evaporator. The coated wafers were then divided into 20 x 20 mm squares using an ADT 7100 Dicing saw.

The 1,3-dichloromethyldisiloxane, perfluorodecyldimethylchlorosilane, and methoxypolyethyleneoxypropyltrimethoxysilane were purchased from Gelest and Optool DSX was sourced from Daikin. Probe liquids and test liquids were used as received: ethanol, acetone, 2-propanol, toluene, pentane, hexadecane, and dimethylformamide (Fischer Scientific), Vertrel XF dihydrodecafluoropentane (Chemours), trimethylchlorosilane (Acros Organic), diiodomethane (Sigma Aldrich), perfluorohexane (VWR International).

1,3 cPDMS Process

The 1,3-dichlorotetramethyldisiloxane was drop cast onto the plasma cleaned silicon and left to react at atmospheric conditions for 1 hour. It was then rinsed with toluene, acetone, and 2-propanol. The 'capping' process involved attaching methyl groups to the free silanols on the surface to further reduce the surface energy and hysteresis. The PDMS treated silicon was placed in a PTFE container with 200 μL of trimethylchlorosilane for 2 hours. The sample was again rinsed with toluene, acetone, and 2-propanol.

F13CL Process

The perfluorinated, 'glassy' surface was prepared as a comparison to the amorphous surfaces. The plasma cleaned silicon was exposed to (tridecafluoro-1,1,2,2-tetrahydrooctyl)dimethylchlorosilane at 120°C at <5mm Hg in a vacuum oven for 24 hours. The treated surface was then rinsed with Vertrel XF, toluene, acetone, and 2-propanol. The mono-functional version was chosen over the more reactive tri-chloro counterpart to minimize self-polymerization and surface roughness.

PEG-3 Process

A 200 mL solution was prepared of toluene with 0.2w% methoxypolyethyleneoxypropyltrimethoxysilane and 0.1w% 1 molar hydrochloric acid to act as catalyst. The solution was placed in a PTFE container and the plasma cleaned silicon surface submerged in the solution for 2 hours. After treatment, the surface was sonicated in toluene, acetone, and 2-propanol for 2 mins each.

PFPE Process

The plasma cleaned silicon was exposed for 100 hours to Optool DSX at 150℃ at <5mmHg in a vacuum oven. After treatment, the surface was rinsed with Vertrel XF, toluene, acetone, and 2-propanol. Due to the very slow reaction rate of the silane, the extended silanization time was necessary to create a densely packed monolayer that had minimal hysteresis.

Lubricant Infused Surface (SLIPs)

The lubricant infused surface was produced to give a comparison in durability. It was manufactured from an aluminum substrate (6061 T6 Aluminum Alloy, McMaster-Carr) which was first etched in 2.5 molar hydrochloric acid (Fischer Scientific) for 20 minutes to create nano-structure. It was then agitated in a bath sonicator for 10 minutes to remove loose aluminum particles and placed in boiling water to convert the outer layer to boehmite nano-crystals (γ-AlO(OH)). The textured aluminum was reacted with a vapor of (heptadecafluoro-1,1,2,2-tetrahydrodecyl)triethoxysilane (Gelest) in a vacuum oven at 100℃ and ~5 mTorr for 24 hours. After rinsing with Vertrel XF, Toluene, and IPA, Krytox GPL-100 perfluoropolyether oil

(Miller-Stephenson Chemical Company) was drop cast onto the surface, and the sample inverted for 12 hours to allow excess oil to be removed.

2.3.2 Measurement of Contact Angle and Surface Energies

Advancing and receding contact angles for the liquids were obtained from a sessile drop method using a Ramé-Hart 200 F1 contact angle goniometer. A dispensing needle was placed just above the substrate surface and a 10 μL droplet was suspended from the needle. The volume of the droplet was then increased to obtain advancing contact angles and decreased to obtain receding contact angles. DROPImage Advanced software was used to obtain the contact angle using a circular drop fit. Three points on each substrate were measured, and the mean value reported with a standard error of ±2°. The measured contact angles for each surface are shown in **Table 2.2**.

Table 2.2: Measured contact angle for the four test liquids on each of the four surfaces tested. Only water was measured on the PEG-3 as all other liquids fully wet the surface due to the high surface energy, higher than the surface tension of the liquids.

Surface Type	Water θ_a	Water θ_r	DMF θ_a	DMF θ_r	Toluene θ_a	Toluene θ_r	Pentane θ_a	Pentane θ_r
$F_{13}Cl$	113°	91°	78°	46°	58°	31°	34°	14°
PEG-3	52°	45°	--	--	--	--	--	--
1,3 cPDMS	106°	101°	67°	62°	31°	30°	22°	20°
PFPE	120°	115°	87°	81°	70°	64°	36°	34°

To estimate the surface energy of each coating, we used the Owens-Wendt Method.[35] After silanizing each surface, the Owens-Wendt analysis was performed with water (dispersive surface tension, γ_{lv}^{d}=21.1 mN m^{-1}, and polar surface tension γ_{lv}^{p}=51.0 mN m^{-1}) and hexadecane

(γ^{d}_{lv}=27.5 mN m^{-1} and γ^{p}_{lv}=0.0 mN m^{-1}). Using the mean static contact angles of each liquid on the surface, the dispersive (γ^{d}_{sv}) and polar (γ^{p}_{sv}) components of the solid surface energy can be calculated by:

$$2\begin{bmatrix}\sqrt{\gamma^{d}_{water}} & \sqrt{\gamma^{p}_{water}}\\ \sqrt{\gamma^{d}_{hexadecane}} & \sqrt{\gamma^{p}_{hexadecane}}\end{bmatrix}\begin{bmatrix}\sqrt{\gamma^{d}_{sv}}\\ \sqrt{\gamma^{p}_{sv}}\end{bmatrix}=\begin{bmatrix}(1+\cos\theta_{water})\gamma_{water}\\ (1+\cos\theta_{hexadecane})\gamma_{hexadecane}\end{bmatrix} \tag{2.3}$$

Results of these calculations for each surface can be found in Table S.3. Note that for the PEG surface, since the surface energy is so high and hexadecane fully wet the surface, we had to use Diiodomethane (γ^{d}_{lv}=50.8 mN m^{-1} and γ^{p}_{lv}=0.0 mN m^{-1}) instead of hexadecane in the Owens-Wendt calculation to obtain the surface energy.

Table 2.3: Summary of the polar, dispersive, and net surface energy for each of the experimental coatings. Surface energies were calculated using the Owens-Wendt method described above.

Surface Type	γ^{d}_{sv} **(mN m^{-1})**	γ^{p}_{sv} **(mN m^{-1})**	$\gamma_{sv,\ net}$ **(mN m^{-1})**
$F_{13}Cl$	14.5	0.6	15.1
PEG-3	45	16.7	61.7
1,3 cPDMS	23.7	1.4	25.1
PFPE	14.6	0.2	14.8

2.3.3 Droplet Departure Diameter Calculation

Analysis of the experimental departure diameter was performed using ImageJ. Various photos were used that imaged the surface at 5°C and 10°C subcooling. The scale of the image was first calculated using the edge length of the samples which was consistent at 20 mm x 20 mm. Departed droplets near the top of the sample on the surface, were identified as being just departed if there was a droplet with an absence of droplets just above it, indicating that a droplet recently departed that area, which is depicted in **Figure 2.9**. If there was a long path above a droplet, that droplet was not used in this analysis as it would indicate the droplet has been moving and coalescing which would give an inaccurately large diameter. Once a droplet was identified, the brightness and contrast was adjusted on ImageJ to provide a clear and distinguishing border around the perimeter of the departed droplet. Provided the scale previously set, the diameter of the droplet could be directly measured.

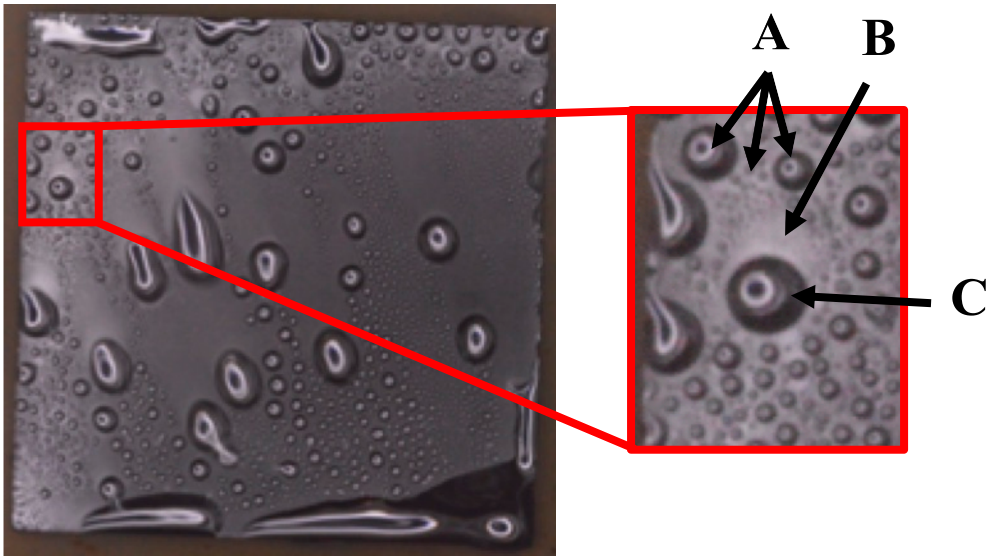

Figure 2.9. Example image of the droplet departure analysis performed. Larger droplets (a) surrounding a (b) void with newly nucleated droplets implying a recently departed droplet (c). When a droplet departs, it moves across the surface and coalesces with other droplets. Once it moves down, there is space where it recently was that is free of any droplets and new droplets nucleate. If there are larger droplets above these newly nucleated droplets, it implies that the moving droplet didn't sweep past them and thus must have departed from the void with the newly nucleated droplets.

2.3.4 Durability and Longevity Characterization

To compare the durability of the surfaces, they were subjected to two tests to expose them to mechanical and chemical abuse. The first test was a series of linear abrasions that reciprocated an abrasive felt over the surface with contact angle being measured after set numbers of abrasions. The second test was an extended use test in which the samples were placed in the heat transfer chamber and experienced continuous condensation for multiple hours.

The mechanical durability test was performed by comparing the θ_{adv} and θ_{rec} with both water and hexadecane after a series of linear Taber abrasions. A piece of silicon was cut to be approximately 75mmx25mm. The silicon was then treated according to the deposition process outlined in 2.3.1. Sample was then mounted to a Taber model 5750 Linear Abrader which has a CS-5 (~12.5 mm diameter) abrasive felt tip attached, and a 500-gram load was applied which produced an equivalent pressure of about 40 kPa. The abrasion head was moved in a reciprocating fashion back-and-forth across the surface in a one-inch length at a speed of 60 cycles/min. After a set number of abrasions, the system was stopped, the surface rinsed with acetone, IPA, and water, and the sample was dried with compressed air. The contact angles were measured at three different places along the abrasion length using both water and hexadecane. After the contact angles were measured, the sample was returned to the abrader for additional abrasion cycles. For most surfaces, the contact angles were collected after every 1000 abrasion cycles initially, and then every 3500 cycles thereafter. For surfaces that degraded rapidly, the contact angles were collected every 100 abrasion cycles.

For the extended use tests, a specimen was first mounts to the condensation test apparatus and deposited with the coating. The system was then operated at normal test conditions with an absolute pressure of 15 kPa and saturated water vapor. The thermal flux of was fixed at 0.1 MW m^{-2} and thermocouple measurements and elapsed time were collected every 20-30 hours. The heat transfer coefficient was calculated at each time interval and plotted to show any degradation in heat transfer performance the surface experiences over extended use.

2.4 Testing in Environmental Chamber

The heat transfer measurements were performed in a custom designed and built environmental chamber. This testing chamber was modified to conform to testing conditions utilized by other research groups. Testing is done at negative relative pressure to increase efficiency as outlined below. This also replicates commercial condensers which are operated at 2-10 kPa to maximize efficiency.

2.4.1 Chamber Layout

The outside view of the chamber can be seen in **Figure 2.10** and schematic in **Figure 2.11**, with the main body of the chamber composed of a stainless steel 4-way cross, vacuum fitting with 6-inch ConFlat flanges. Each of the 4 openings have an attachment to them. The first opening has the sample mounting that is insulated by Teflon and connected to a liquid chiller that uses a PID controller to regulate the cooling temperature. The top opening has a smaller cross attached that consolidates multiple openings. This cross includes a pressure gauge (absolute piezo vacuum transducer, measurement range from 0.1-1300 torr), type T thermocouple (12-inch stainless steel sheath), and valve that opens/isolates the chamber to a vacuum pump. The vacuum pump can reach an absolute pressure of 0.1 Pa, and there is a liquid nitrogen trap (not pictured) between the chamber valve and pump to prevent any vapors from entering the pump. During operation, all flanges are sealed with a perfluoroelastomer (FFKM) gasket and 6 bolts. Heaters are attached to the outside of the chamber to heat the chamber walls. The wall temperature can be controlled with a variable voltage controller to maintain a wall temperature 1-2°C above the boiling temp of the liquid. This prevents vapor from condensing on the walls of the chamber which would reduce the condensation rate on the sample surface.

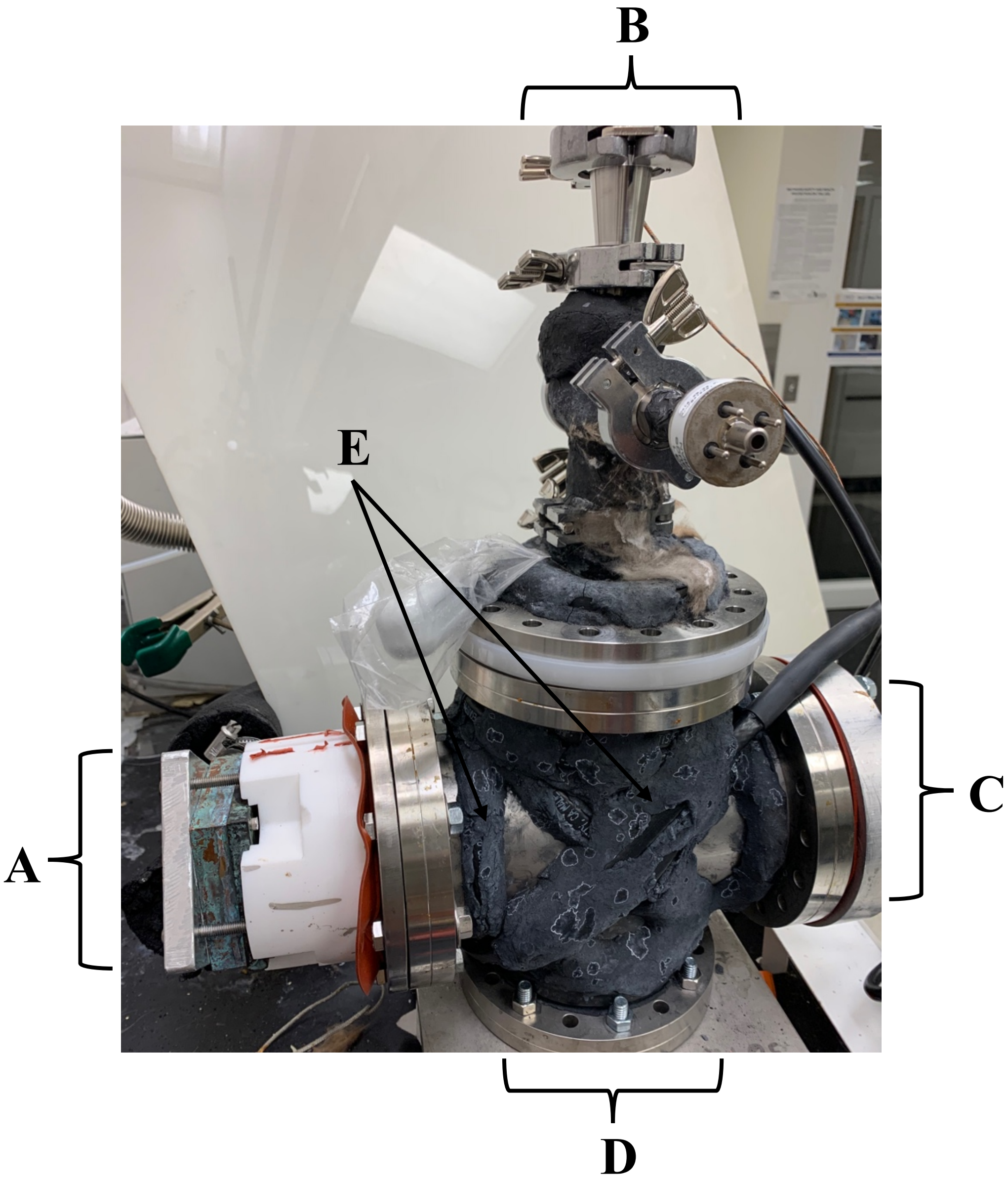

Figure 2.10: Outside view of the environmental test chamber. The main body is a stainless-steel cross with 4 openings. **A)** Sample mount with PID liquid controlled cooling. **B)** Measurement and vacuum stack which consolidates the vacuum measurement, temperature measurement, and vacuum port. **C)** Quartz viewing window that allows photographs and videos to be imaged of the sample at the back of the chamber. **D)** Base plated of chamber that has heaters for evaporating liquid and port to allow liquid into the chamber. **E)** Strip heaters attached to the outside of the stainless-steel cross with heat transfer putty to maintain the wall temperature and prevent preferential condensation on the chamber walls.

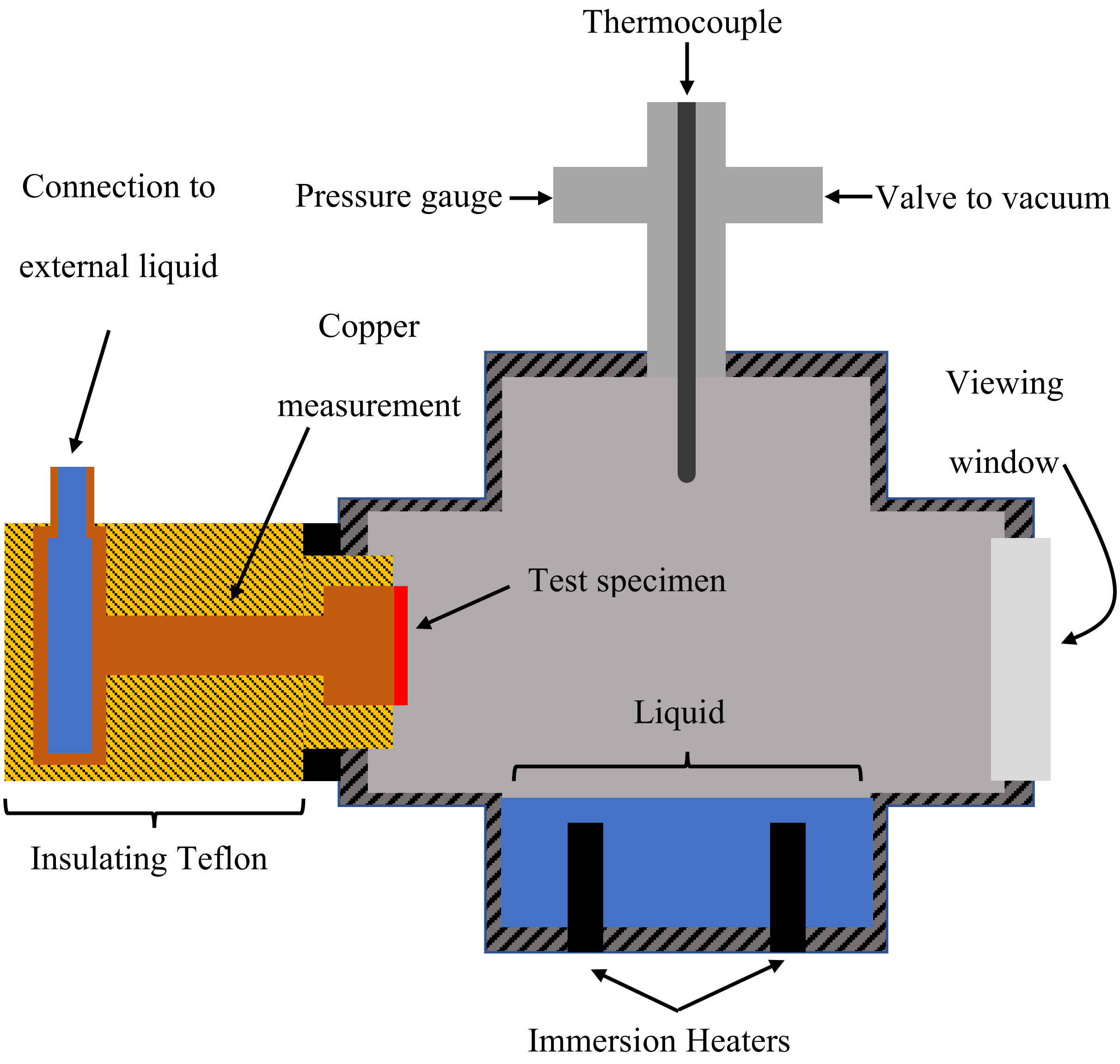

Figure 2.11: Schematic of a cross sectional view of the experimental chamber. Liquid at the base of the chamber is vaporized into the chamber. Liquid colling controls the test specimen surface and liquid condenses on the surface. Imaging can be performed through the viewing window. The heat transfer and temperature data are collected along the copper measuring block.

The heat transfer occurs in the copper shown on the left side of **Figure 2.11** with a detailed view in

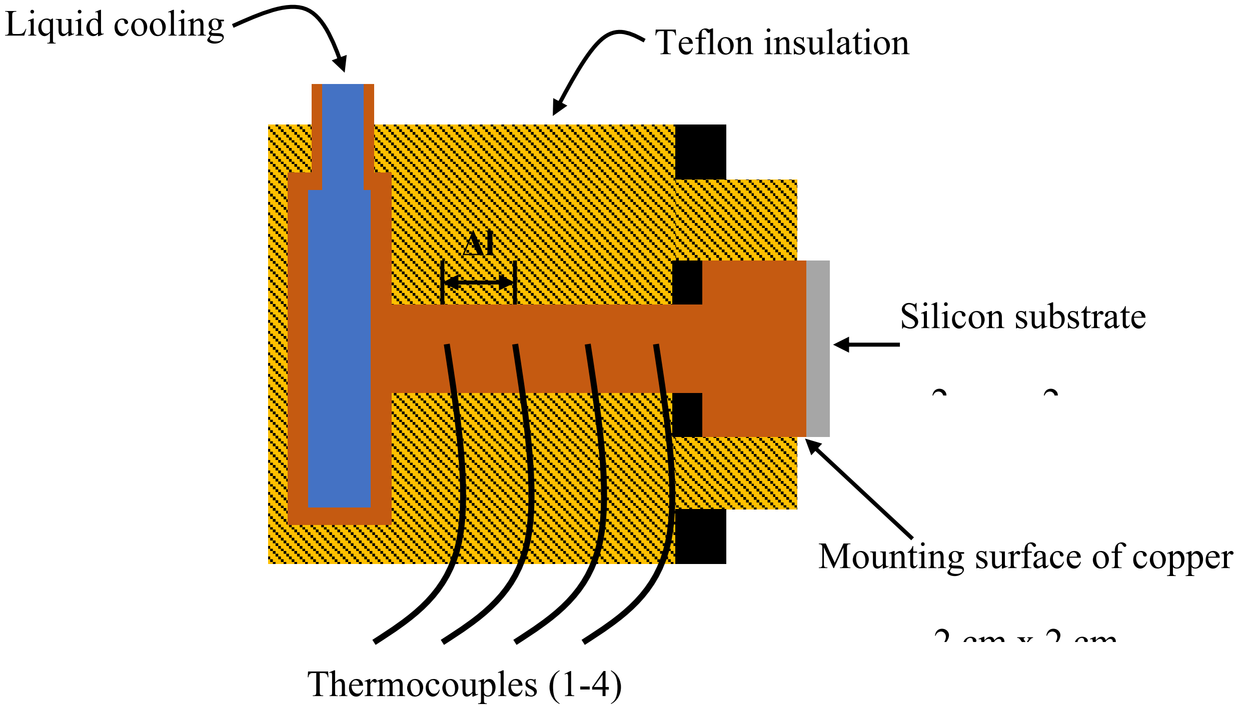

Figure 2.12. A silicon subsrate is attached to a length of copper with a tin and lead based solder. The backside of the silicon has 25 nm of NiCr followed by 250 nm of copper deposited on it, this allows the solder to strongly adhere to the silicon and introduce minimal interfacial resistance between the copper length and silicon. On the opposite end of the copper, liquid flow channels are attached which are connected to a recirculating chiller. The chiller can maintain a 50/50 water/ethylene glycol bath at a set temperature within 0.1°C. The chilled ethylene glycol mix is circulated through the cooling channels attached to the copper to constantly remove chill the substrate, creating the heat flux that is measured. Along the length of the copper, thermocouples are inserted to measure the temperature at known intervals (Δl) of 7.5 mm. Based on the temperature readings at each interval, the heat flux and surface temperature can be inferred. The copper is surrounded by a thick wall of Teflon. Since the conductivity of copper is more than

200x greater than Teflon, it can be assumed that any lateral heat transfer is negligible, and all heat transfer is through the surface of the substrate. The surface of the silicon substrate is treated with the target experimental coating. Since the heat transfer due to convection in a vacuum is negligible to that for phase transformation, the heat flux measured by the thermocouples can be attributed entirely to the condensation behavior of the surface. Along the perimeter of the Teflon insulation and the copper, there are FFKM gaskets to seal the chamber and maintain vacuum pressure.

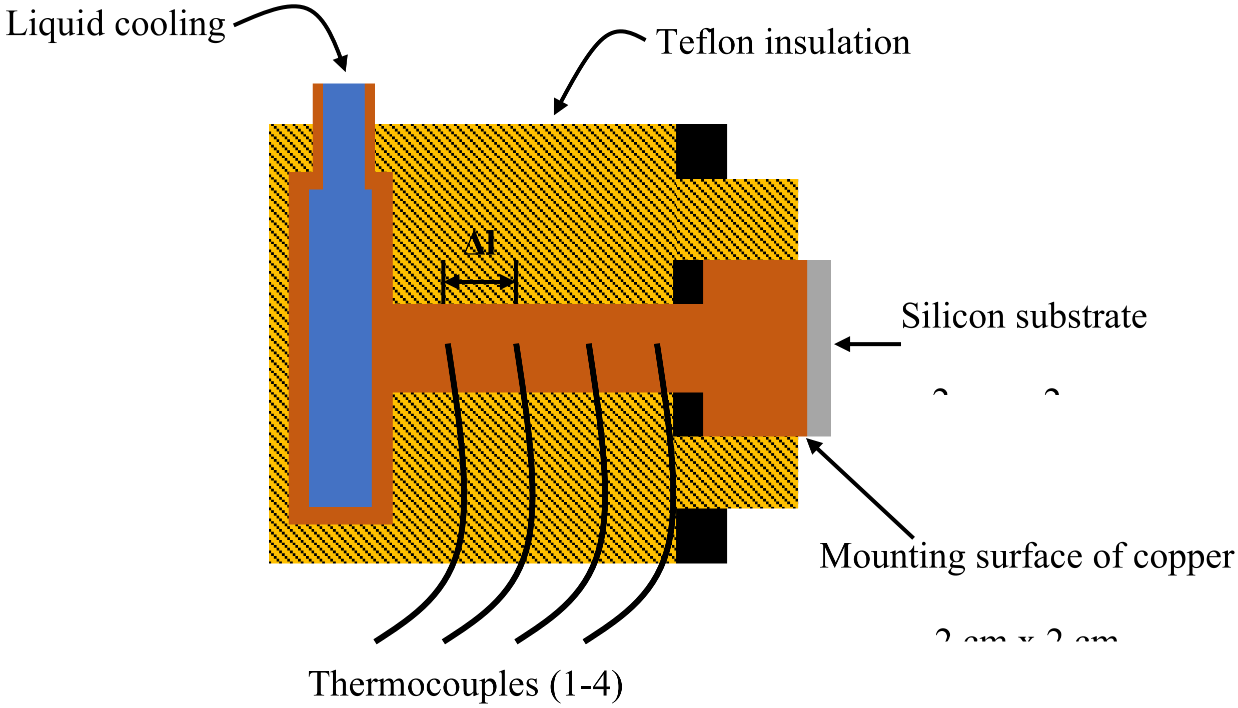

Figure 2.12: Detailed schematic of how the surface is cooled and heat transfer measured. The liquid cooling one the left provides the heat transfer out of the system while the silicon substrate condenses liquid due to the temperature differential with the vapor in the chamber. The thermocouples measure the temperature gradient between the sample and heat sink so the heat flux and surface temperature can be calculated.

During the experiment, the temperature readings of each thermocouple are recorded at various liquid cooling temperatures. For each thermocouple recording, data is averaged over 120 second at 100 readings per second. A linear fit is then applied to the 4 thermocouple readings and the slope of the line calculated (dT/dx). Based on the slope of the temperature differential (dT/dx) and the thermal conductivity of copper (k_{cu}), the heat flux through the narrow portion that the thermocouple were could be calculated by:

$$q''_{narrow} = -k_{cu}\frac{dT}{dx} \tag{2.4}$$

Since heat flux is dependent on area, this would not be the same as the heat flux at the surface. The heat flux through the narrow, round portion (d = 15 mm) can be converted to a total energy transmission and then scaled to the corresponding area of heat transfer, the 2 cm x 2 cm square substrate.

$$q''_{substrate} = q''_{narrow}\frac{\pi(7.5)^2}{20^2} \tag{2.5}$$

The surface temperature (T_{surf}) can also be calculated from the heat flux and thermocouple data. The temperature drop from the thermocouple nearest the substrate (T_4) to the surface of the substrate could be calculated as follows:

$$T_{surf} = T_4 + \Delta T_{narrow} + \Delta T_{mount} + \Delta T_{Si} \tag{2.6}$$

The temperature drop through the narrow portion of the copper, between the thermocouple (T_4) and the bottom of the mounting portion of copper, can be determined by the heat flux previously calculated and the distance between them (7.5 mm):

$$\Delta T_{narrow} = \frac{q''_{narrow}}{k_{cu}}(7.5) \tag{2.7}$$

The temperature drop through the mounting portion of copper (length = 15 mm) can then be calculated from the heat flux of the substrate as they are the same cross-sectional area:

$$\Delta T_{mount} = \frac{q''_{substrate}}{k_{cu}}(15) \tag{2.8}$$

Lastly, the temperature drop through the silicon can be calculated from the same heat flux and the thickness of the silicon substrate (500 μm):

$$\Delta T_{Si} = \frac{q''_{substrate}}{k_{Si}}(0.5) \tag{2.9}$$

The conductivity of copper is nearly constant at 400 W m^{-1} K^{-1}, but the conductivity of silicon is more temperature dependent in the working range for these experiments so it was estimated by:[149]

$$k_{Si} = 150(\frac{T_{surf}}{300[K]})^{-4/3} \tag{2.10}$$

Based on these calculated values, the heat flux (q'') and surface temperature could be used to determine the heat transfer performance of the surface. With the heat transfer coefficient being determined by the slope of the linear fit when heat flux (vertical axis) is plotted against surface subcooling (horizontal axis). The surface subcooling (δT) was calculated from the surface temperature and vapor temperature (T_{vapor}) measured by the thermocouple at the top of the chamber in **Figure 2.11**:

$$\delta T = T_{vapor} - T_{surf} \tag{2.11}$$

2.4.2 Significance of Non-Condensable Gases

All of the condensation experiments in this work were performed under vacuum, and a majority of work published by other researchers is also done under vacuum conditions. The reason for this is to remove as many non-condensable gases from the testing chamber as possible. Non-condensable gases (NCGs) (i.e. oxygen, nitrogen, etc.) inhibit the condensation on the surface and therefore reduce the heat transfer performance of the surface. Initial work to rectify this used rapid air streams or increased vapor flow rates to diminish the effect of NCGs,[150–156] but it wasn't well understood until a study in 2008 identified the mechanism by which NCGs inhibit heat transfer with a direct comparison of different ratios of NCGs present shown in **Figure 2.13**.[157] It found that there are two methods by which condensation is inhibited. The first is by way of forming a resistive boundary layer that increased the thermal resistance for heat transfer between the bulk vapor and surface. Just as a thick resistive coating, or a film of resistive liquid, inhibits heat transfer, a layer of gases covering the surface prevent heat transfer. The more NCGs that are present, the thicker and more resistive this boundary layer is. The second mechanism is by the creation of a diffusive layer that the vapor must move through. The layer of NCGs present near the condensing surface creates a gas phase diffusion layer that inhibits the movement of vapor to the surface, thereby inhibit the condensation of the vapor. These two factors, combined, can lead to a more than 50% decrease in heat transfer coefficient, bringing the performance of a dropwise condensing surface to a comparable level as filmwise condensation. Even a marginal 1% NCGs present can reduce the heat transfer by 30%. Therefore, extensive efforts were made to ensure that the test chamber in this work was sufficiently vacuum tight and to ensure non-condensable gases were minimized.

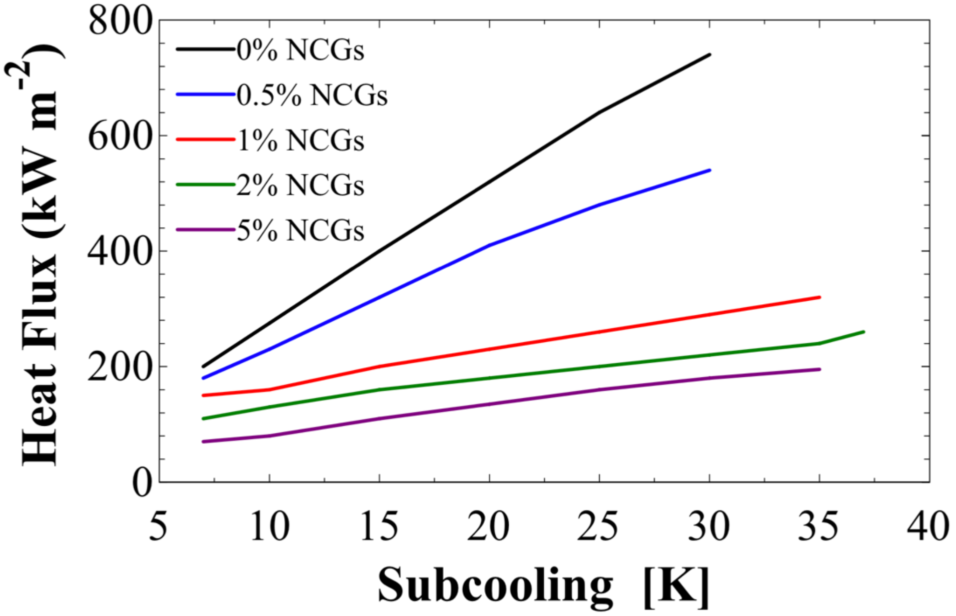

Figure 2.13: Effect that the presence of non-condensable gases have on the heat transfer performance of a surface. Tests were performed with a fluoropolymer coating and tested at atmospheric conditions. Plot is adapted from study in the International Journal of Heat and Mass Transfer.[158]

2.4.3 Experimental Procedure

Condensation experiments were conducted in a manner consistent with other research groups' studies. Silicon substrates were first mounted on onto the copper measurement block by heating to 190°C and using a tin and lead solder to adhere the two together. Prior to adherence, the double-sided silicon wafers were deposited with NiCr and Cu to enhance adhesion with the solder. The Cu backed wafers were then backed at 400°C to relax the internal stress and then the wafers were diced into 20 mm x 20 mm. Once the silicon substrate was mounted and cooled, the silicon was plasma cleaned and deposited with the desired coating. The Teflon enclosure with copper measurement block and mounted sample were mounted to the condensation chamber with the test surface flush with the chamber wall.

Prior to the test commencing, the chamber was evacuated down to a pressure of 1 Pa for 2 hours to ensure all non-condensable gases were sufficiently removed. At the same time, the strip heaters on the outside of the chamber were turned on at a voltage to maintain a chamber surface temperature 2-3°C above the expected boiling temperature of the liquid at 3 kPa. After the 2-hour evacuations, the chamber was sealed and a valve on the bottom of the chamber opened to allow the test liquid to enter the chamber. Once approximately 500 mL of liquid entered the chamber, the liquid valve was also closed, and chamber now isolated. The immersion heaters were turned on with a voltage to maintain the liquid and vapor temperatures were identical. The pressure of the chamber increased and stabilized between 2-3 kPa with saturated vapor. The liquid cooling was then initiated with a liquid set point temperature 5°C below the vapor temperature. Once the thermocouple readings stabilized, the data was readings were collected as described above. The liquid cooling was decremented by 2-5°C, depending on the proximity to the critical heat flux, and once the thermocouples stabilized, the readings were collected in the same manner. This procedure was repeated until the maximum heat flux was achieved which correlated with the maximum cooling capacity of the recirculating chiller (~100 watts).

While efforts were made to use similar test conditions to comparable studies, there were small variations, and in an attempt to better correlate the results, all results were extrapolated to atmospheric conditions for better comparison. To make the adjustment, the experimental data was divided by the ratio of the expected heat transfer from the model at test pressure and the expected heat transfer from the model at 101.3 kPa (atmospheric). The model calculated the heat transfer coefficient (HTC) from the heat transfer through individual drops q(r) and the distribution of the number of drops of a given radius.[159]

$$\mathrm{HTC}=\frac{q''}{\Delta T}=\frac{1}{\Delta T}\left(\int_{r_{min}}^{r_e} q(r)*n(r)dr+\int_{r_e}^{\hat{r}} q(r)*N(r)dr\right) \tag{2.12}$$

$$q(r)=\frac{4\pi r^2\left(1-\frac{r_{min}}{r}\right)\Delta T}{\frac{r}{k_c}+\frac{2}{h_i}+\frac{t_p}{k_p}} \tag{2.13}$$

$$n(r)=\frac{\left(\hat{r}/r_e\right)^{2/3}}{3\pi r_e^2\hat{r}}\left(\frac{r}{r_e}\right)\exp\left(\frac{r_e^2-r^2}{2a\tau}\right) \tag{2.14}$$

$$N(r)=\frac{\left(\hat{r}/r\right)^{2/3}}{3\pi r^2\hat{r}} \tag{2.15}$$

Where ΔT is the subcooling of the surface, r is the droplet radius, r_e is the radius of coalescence for the droplets, r_{min} is the minimum radius for a droplet to heterogeneously nucleate, $\hat{r}$ is the droplet departure radius and was assumed to be the capillary length, n(r) is the distribution of non-coalescing droplets, N(r) is the distribution of coalescing droplets, k_c is the thermal conductivity of the condensate, h_i is the interfacial heat transfer coefficient of a droplet, t_p is the thickness of the promoter layer, and k_p is the conductivity of the promoter layer. The first integral in equation S2 relates to the total heat transfer through droplets smaller than the coalescence length, and the second integral is that for droplets larger than the coalescence length. The nucleation density was assumed to be $2\times10^{11}\mathrm{m}^{-2}$ in accordance with other published assumptions.

For filmwise condensation, the Nusselt model was used estimate the HTC at the test pressure and atmospheric pressure[160]:

$$\mathrm{HTC}_{\mathrm{filmwise}}=0.729\left(\frac{g^{*}\rho_{l}(\rho_{l}-\rho_{v})k_{l}^{3}h_{fg}^{'}}{\mu_{l}(2r)\Delta T}\right) \tag{2.16}$$

$$h_{fg}^{'}=h_{fg}+0.68c_{p,l}\Delta T \tag{2.17}$$

Where g is the acceleration of gravity (9.8 m s^{-2}), ρ_l is the condensate liquid density, ρ_v is the vapor density, k_l is the thermal conductivity of the condensate, μ_l is the dynamic viscosity of the condensate, $h_{fg}^{'}$ is the modified latent heat of vaporization with the change in specific heat of the condensate, and $c_{p,l}$ is the specific heat of the condensate.

2.5 Results

2.5.1 Heat Transfer Results

Heat transfer performance was collected for liquids with water, dimethyl formamide, and toluene, which covered a range of surface tensions, 72.1 mN m^{-1}, 35.1 mN m^{-1}, and 27.5 mN m^{-1}, respectively. Given the wetting interactions of these liquids on the previously identified coatings, a direct comparison was able to be made for the effect the contact angle on HTC, effect that hysteresis has on HTC, and the effect that hysteresis has on CHF. **Table 2.4** summarizes the heat transfer results collected in all the experiments performed.

Heat Transfer Coefficient (kW m^{-2} K^{-1})

	Water **(γ_{lv}=72.1)**	**Dimethylformamide** **(γ_{lv}=35.1)**	**Toluene** **(γ_{lv}=27.5)**
Bare Si	10.26 ± 0.79	2.97 ± 0.16	1.87 ± 0.21

PEG-3	26.85 ± 0.89	--	--
1,3 cPDMS	21.34 ± 0.82	8.73 ± 0.58	DWC: 5.06 ± 0.25 FWC: 1.51 ± 0.22
F13Cl	--	5.48 ± 0.25	DWC: 3.73 ± 0.20 FWC: 1.63 ± 0.13
PFPE	--	6.52 ± 0.43	DWC: 6.88 ± 0.31 FWC: 1.52 ± 0.14

Table 2.4: Summary of heat transfer results for all combinations of liquid/surface coatings that were measured herein. The highest HTC achieved for water, dimethylformamide, and toluene were achieved utilizing the PEG-3, 1-3 cPDMS, and PFPE polymer brushes, respectively.

The first comparison can be done when examining the heat curve for water, which was condensed on the PEG-3, 1,3 cPDMS, and bare Si, shown in **Figure 2.14**. This study is the first to show sustained dropwise condensation with water on a surface with an apparent contact angle less than 60°. The PEG-3 monolayer combined all of the design factors outlined above: a thin chemically homogenous surface with minimal roughness to minimize thermal resistance and decrease hysteresis, a glass transition temperature of -70°C, ~100°C below the vapor temperature of water (~30°C), and a contact angle near the peak heat transfer in **Figure 2.7**. Although the contact angle is not at the maximum point, it is nearer the maximum than a hydrophobic surface, represented by the 1-3 cPDMS in this comparison. Given that the 1-3 cPDMS is a similar coating with similarly very low hysteresis (5° compared to 7° for 1-3 cPDMS and PEG-3, respectively) and is in an amorphous state with a T_g of -130°, the only distinguishable difference between these surfaces is the apparent contact angle. The contact angle displayed by the 1-3 cPDMS is

50° higher than the PEG-3 and is further from the maximum HTC peak indicating the hydrophilic PEG-3 should display a higher HTC compared to the hydrophobic 1-3 cPDMS.

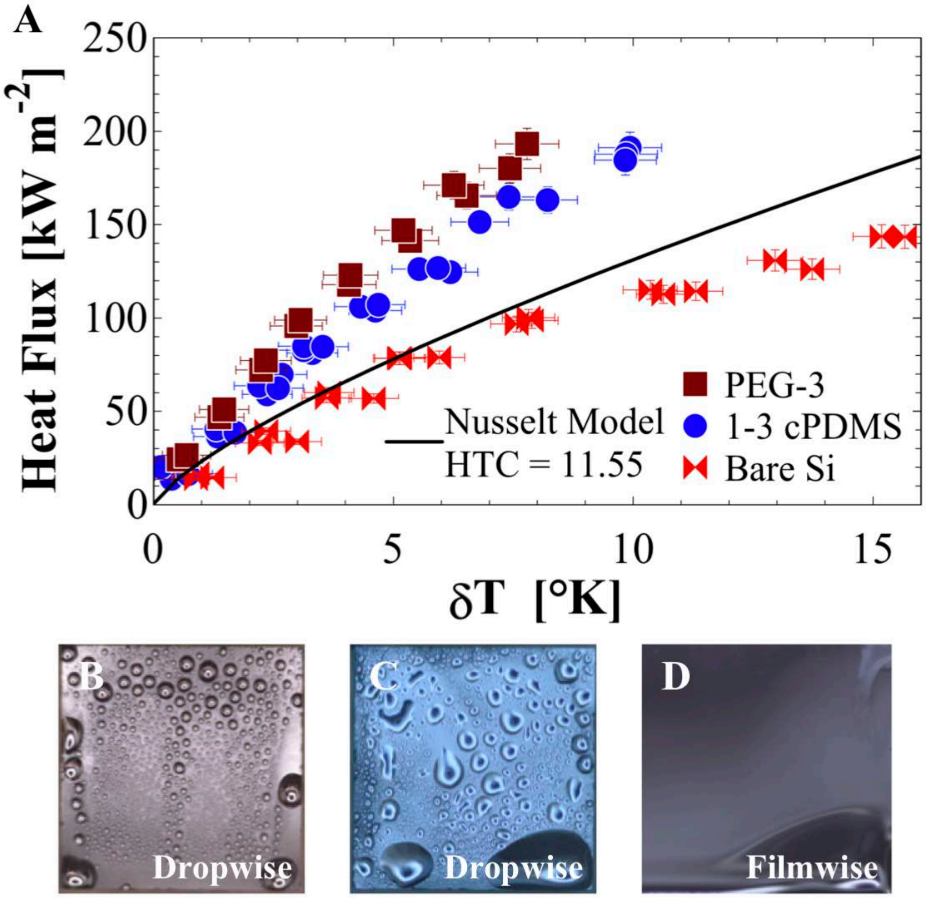

Figure 2.14: Condensation heat transfer results for water on PEG-3, 1-3 cPDMS, and bare Si. **A)** Heat curve with data collected for the 3 surfaces along with a representation of the Nusselt model, a numerical model predicting the heat transfer for filmwise condensation. **B-D)** Images of the condensation mode at 5°C subcooling on 1-3 cPDMS, PEG-3, and bare Si, respectively. PEG-3 and 1-3 cPDMS both displayed dropwise condensation for the entirety of the testing range, up to the maximum achievable heat flux of 200 kW m^{-2}.

The resulting heat curve shows that this hypothesis is correct, reducing the contact angle enabled greater heat transfer with minimal changes to hysteresis or other material properties. The PEG-3 had a heat transfer coefficient of 26.85 kW m^{-2} K^{-1}, a 26% improvement over the hydrophobic 1-3 cPDMS which only had an HTC of 21.34 kW m^{-2} K^{-1}. While both the PEG-3 and 1-3 cPDMS exhibited ultra-low T_g, hysteresis of 8° or less, and were able to sustain dropwise condensation, the higher surface energy of the PEG-3 enabled a greater condensation rate. When scaled to atmospheric conditions, this represents an HTC of 53.51 kW m^{-2} K^{-1}, which is a 373% improvement over filmwise condensation. Once scaled to atmospheric, this can also be directly compared to a study in Advanced Materials that condensed on smooth, hydrophobic, thin, polymer films which achieved an HTC of about 38 kW m^{-2} K^{-1}; the PEG-3 coating presents a 41% improvement in heat transfer performance compared to this published work.[132]

Moving on to lower surface tension, dimethylformamide (DMF) provides a direct comparison of the effect of contact angle and the effect of hysteresis. While all the sample tested exhibited contact angles in the previously identified, ideal range ($30° < \theta_a < 80°$), there was significant variation in the heat transfer performance which can be directly attributed to the differences in wetting properties.

First, examining the influence of contact angle, the importance of a hygrophilic surface is support again when comparing the 1-3 cPDMS and PFPE. Both of these polymer brushes have similar properties (ultra-low T_g, CAH ≤ 6°, thin film) with the only distinction between them is the 1-3 cPDMS has a contact angle 20° less than the PFPE. This leads to the 1-3 cPDMS exhibiting an HTC of 8.73 kW m^{-2} K^{-1}, 34% higher than the comparable PFPE (HTC = 6.52 kW m^{-2} K^{-1}). This difference can be visually seen in the images of these surfaces in **Figure 2.15** b and d. They have very similar droplet diameters scattered on the surface, but the density of these droplets is greater on the 1-3 cPDMS as predicted by the Gibbs free energy model.

Next, a direct comparison of the significance of hysteresis can be seen when comparing the F13Cl to the PFPE brushes. According to the Kim and Kim model and Gibbs free energy, the F13Cl should present a high heat transfer coefficient due to the marginally higher surface energy. In reality, the PFPE (HTC = 6.52 kW m^{-2} K^{-1}). achieved an HTC 19% higher than the F13Cl (HTC = 5.48 kW m^{-2} K^{-1}). This can be directly associated with the higher hysteresis of the

F13Cl. According to the design criteria, the hysteresis must be minimized to facilitate the departure of droplets from the surface; a high hysteresis will lead to delayed departure, increasing resistance and coalescence of droplets. This effect can be seen visually in **Figure 2.15** c and d in which the droplets on the F13Cl surface are significantly larger than on the PFPE surface and are already coalescing to form a film towards the base of the sample. While both coatings are thin, fluorinated silanes, there is a distinct difference in their glass transition temperatures. At the testing temperature (30°C), the PFPE (T_g = -110°C) would be in an amorphous state whereas the F13Cl (T_g = 175°C) would be in a crystalline "glassy" state. This displays the importance of the glass transition temperature in producing viable, hygrophilic surfaces for condensation.

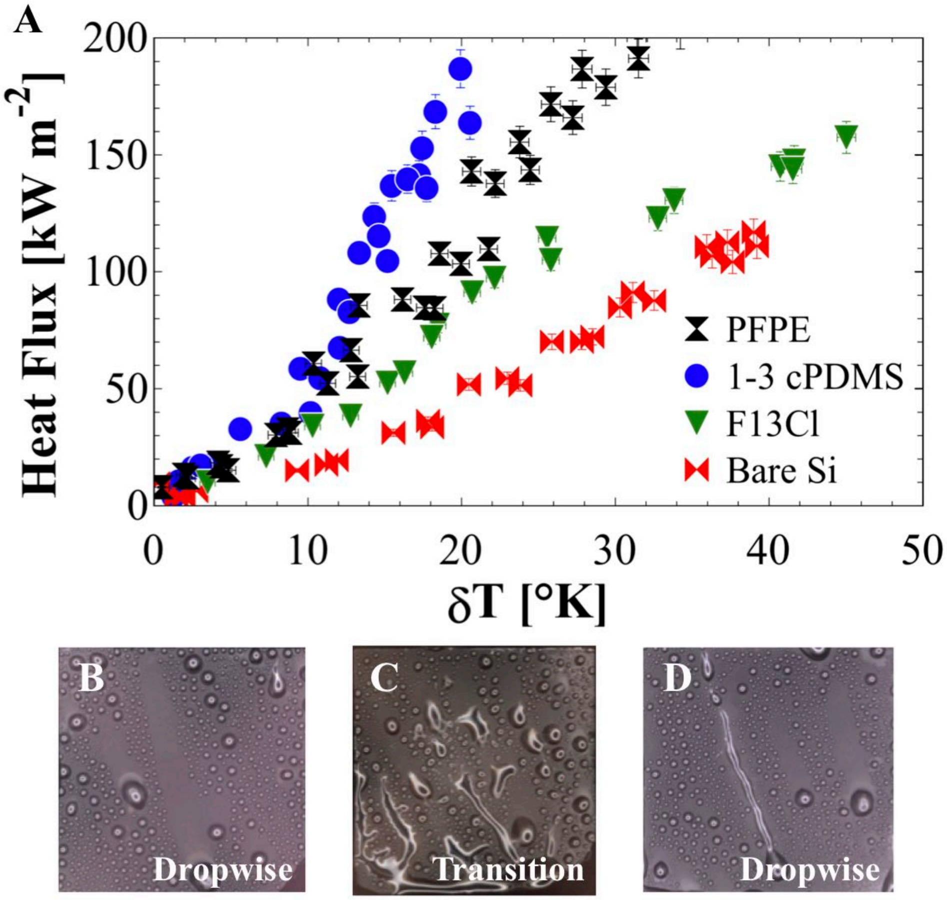

Figure 2.15: Condensation heat transfer results for dimethylformamide on PFPE, 1-3cPDMS, and F13Cl polymer coatings in addition to bare Si for a filmwise reference. **A)** The 1-3 cPDMS displayed the highest heat transfer coefficient due to the lower hysteresis compared to F13Cl and lower contact angle compared to PFPE. **B-D)** Images of the condensation mode at 10°C subcooling on 1-3 cPDMS, F13Cl, and PFPE. At 10°C subcooling, the F13Cl is already beginning to display a transition to filmwise condensation as the droplets are coalescing too quickly and delayed from departing.

Lastly, we examine the heat curve for toluene, a commonly used low-surface tension liquid. This was the only experimental liquid that had a clear and full transition from dropwise condensation to filmwise condensation as all three coatings eventually collapsed to the filmwise curve as shown in **Figure 2.16**. This provides a stark comparison between the F13Cl and PFPE coatings and the significance hysteresis can play. Despite having similar contact angles, the PFPE sustained dropwise condensation at 5 times higher subcooling and the HTC in the dropwise region for the amorphous PFPE was 85% higher than the glassy F13Cl. The importance of hysteresis played a most critical role with the 1-3 cPDMS, though. No previous study has shown dropwise condensation of any low surface tension liquids on a surface with a contact angle lower than 50°.[57] The 1-3 cPDMS coating maintained dropwise condensation with an advancing contact angle of just 31° due to the minimal 1° hysteresis. This becomes clear in the images of condensation on 1-3 cPDMS and PFPE in **Figure 2.14** b and c, respectively. Despite the contact angle of toluene on PFPE being more than twice as large, the droplet diameters are nearly identical as predicted in **Figure 2.5**.

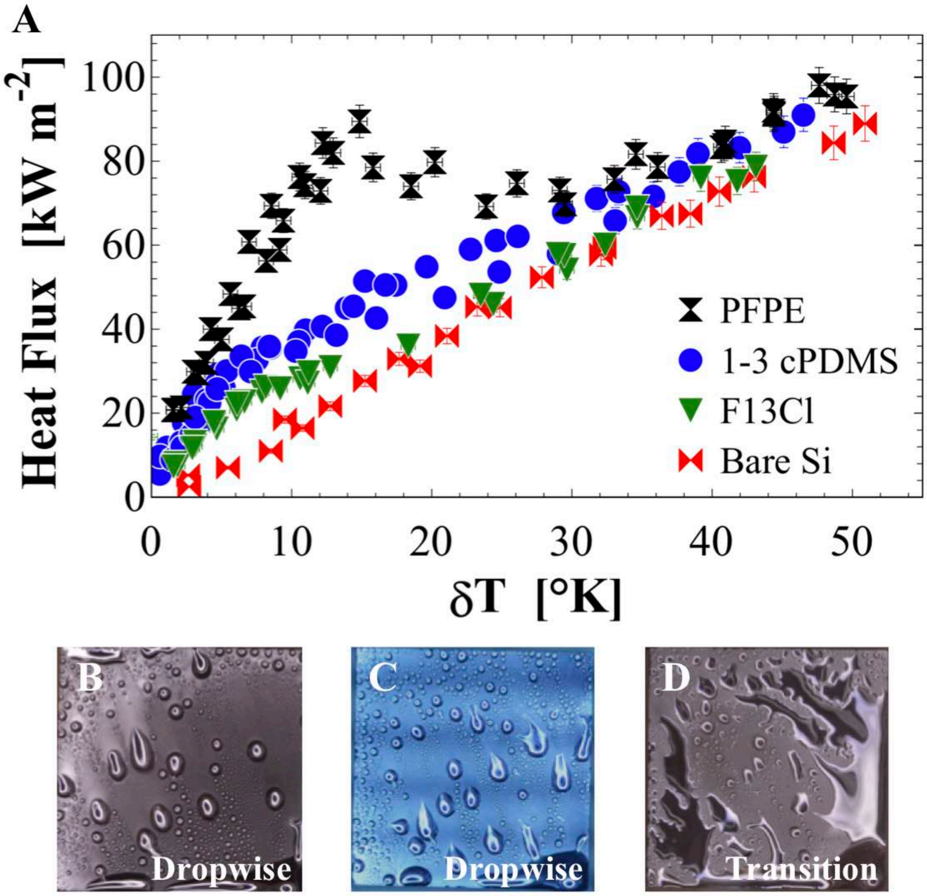

Figure 2.16: Condensation heat transfer results for toluene on PFPE, 1-3 cPDMS, and F13Cl coatings along with bare Si for filmwise reference. All coatings displayed a distinct transition from dropwise to filmwise condensation during this experiment. **A)** The PFPE displayed the highest HTC and CHF of all the surfaces, while the 1-3 cPDMS displayed dropwise condensation on the lowest reported contact angle. **B-D)** Images of the condensation at 5°C subcooling on 1-3 cPDMS, PFPE, and F13Cl. The F13Cl has already started transitioning to filmwise condensation.

2.5.2 Droplet Departure Analysis

The behavior of how droplets grow and depart is critical to the efficiency of heat transfer during condensation. As mentioned above, the size of droplets as they depart can be imaged and is important in verifying the analysis for the mechanism by which these coatings improve the heat transfer. In consideration of **Figure 2.5**, if the hysteresis is sufficiently low, as the polymer brush coatings are, then the departure diameter of droplets should be approximately the same regardless of surface energy. An analysis of the images for water and toluene support this when examining surfaces with similarly low hysteresis but very different contact angles.

Figure 2.17 compares the departure of water droplets from 1-3 cPDMS and PEG-3 coated surfaces.

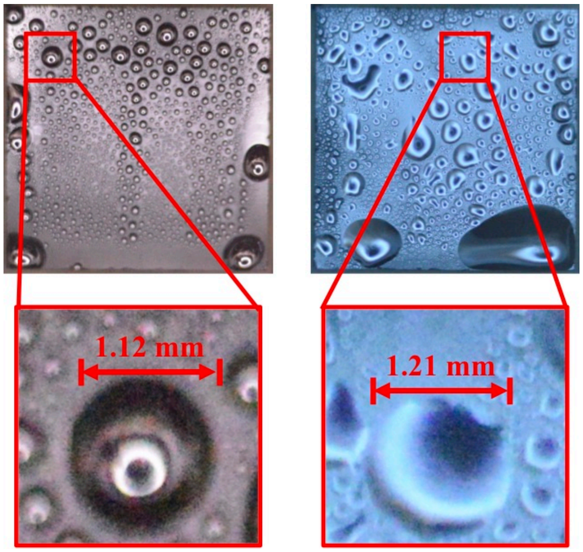

Figure 2.17: Water droplets departing the 1-3 cPDMS (left) and PEG-3 (right) coated surfaces. Despite surface energies and contact angles that are very different, droplets depart the surface at approximately the same diameter.

Despite PEG-3 having a surface energy twice as large, and a contact angle half that, of the 1-3 cPDMS, the droplets depart at nearly the same diameter. This analysis was performed on multiple droplets in

Table 2.5 on each surface and showed that the average departure diameters were nearly identical.

Table 2.5: Measured departure diameter for droplets on 1-3 cPDMS, PEG-3, and PFPE with two of the test liquids. Results show that when hysteresis is sufficiently low, the departure diameters are nearly identical.

	Water		**Toluene**	
	1-3 cPDMS	**PEG-3**	**1-3 cPDMS**	**PFPE**
Departure Diameter (mm)	1.19	1.22	1.01	0.85
	1.13	1.28	0.89	0.92
	1.12	1.14	0.91	0.87
	1.05	1.21	0.98	0.94

	1.08	1.29	0.99	0.93
	1.11	1.11	1.04	0.89
Average (mm)	**1.11**	**1.21**	**.97**	**.90**
Standard Deviation (mm)	**0.05**	**0.07**	**0.06**	**0.04**

The same analysis was performed with toluene to ensure that this is independent of the liquid. With 1-3 cPDMS and PFPE, shown in **Figure 2.18**, the droplets depart at nearly the same diameter and this proved true in the analysis of multiple droplets as well. Therefore, the hysteresis is the primary consideration in droplet departure; if the hysteresis is sufficiently minimized, dropwise condensation can be maintained on nearly any surface. Using this important design parameter, a surface could be customized to maximize condensation heat transfer for any liquid by tuning the surface energy. If that surface has minimal hysteresis, it will sustain dropwise condensation.

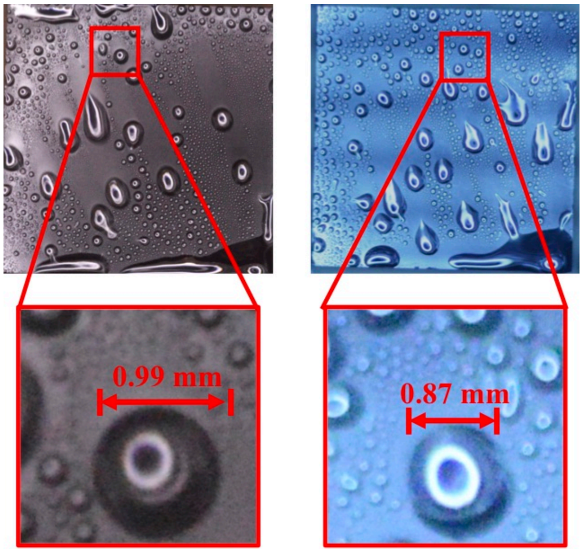

Figure 2.18: Toluene droplets departing the 1-3 cPDMS (left) and PFPE (right) coated surfaces. Again, the surface energy and contact angle becomes negligible when the hysteresis is sufficiently minimized.

2.5.3 Applicability to other substrates and other liquids

An important design consideration when considering the widescale use is the applicability of these coatings to a variety of surfaces and utilization with a variety of liquids. Condensation surfaces have potential use in numerous refrigeration and distillation applications. To display the applicability for such uses, two additional liquids were condensed on the surface in **Figure 2.19**, a common refrigerant R-30 (dichloromethane) (γ_{lv} = 26.5) and a low surface tension component of fuels, pentane (γ_{lv} = 15.6). Both liquids were condensed on the PFPE brushes and displayed dropwise condensation up to the maximum subcooling capability.

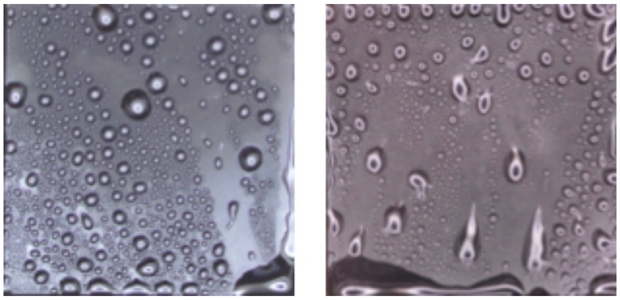

Figure 2.19: Condensation of dichloromethane (left) and pentane (right) on PFPE coated surface. Both liquids displayed dropwise condensation up to the maximum subcooling capability. Due to the volatility of these liquids, collecting a heat curve was difficult and inaccurate.

Widespread adoption of this classification of surfaces also requires the ability to apply to current machinery. Since most condensing surfaces are not made from silicon, copper pipes were coated and condensed on in **Figure 2.20**. The copper required a slightly different deposition method to activate the surface hydroxyl groups for silanization. The copper was first cleaned with toluene, acetone, and IPA. It was then plasma treated for 30 mins and placed in a 2 molar potassium hydroxide (KOH) base bath. After 2 hours in the base bath, the copper was rinsed with water, dried with compressed air, and then treated with the PFPE silane as described in section 2.3.1. After coating deposition, the pipe was attached to the liquid cooling with a vacuum sealed pass through which allowed the liquid to cool the copper pipe while maintaining vacuum in the chamber. Both water and toluene successfully condensed on the PFPE coated pipe, though no heat transfer data could be collected due to the minimal temperature drop in the cooling liquid.

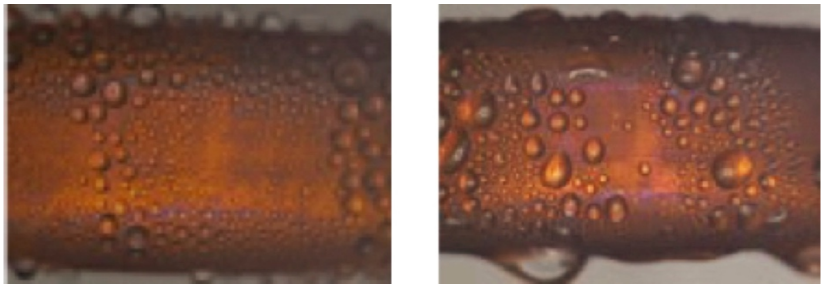

Figure 2.20: Condensation of water (left) and toluene (right) on a copper pipe coated with PFPE brushes. The coated copper sustained dropwise condensation with both liquids, though heat transfer measurements could not be reliable collected.

2.5.5 Comparison of Results to Prior Work

To make a proper comparison of this data to previously published data, all data was scaled to atmospheric conditions based on the analysis outlined previously. The enhancement shown in this study was directly compared to the highest enhancement in any prior study, summarized in **Table 2.6**. This comparison can be done in two ways, the first is comparing to the relative enhancement at the test pressure of the corresponding study, and the second is to scale all results to atmospheric pressure. Both the highest relative improvement and the highest improvement scaled to atmospheric are shown in the table. While the results herein do not exceed some of the highest improvements shown prior, it is important to consider the context for the enhancements. Many of these highest enhancements were performed using mechanisms other than a smooth surface, either through micro- and nano-textured surfaces or through lubricated surfaces. As has been previously discussed, these types of surfaces are limited in either their short time span on enhancement (as with SLIPs) or their narrow usability window (as with jumping droplets). It is important to consider the real-world use conditions of these surfaces and the next section goes to show that the coatings outlined in this study exhibit superior usability characteristics.

Table 2.6: Summary of the heat transfer enhancement of this study compared to the highest previously published enhancement. Note that this study focused solely on smooth films whereas prior studies have used other mechanisms like micro texturing and lubricated surfaces

	This Study						**Highest Results Previously Published**	
Condensate	**FWC HTC (kW m^{-2} K^{-1})**	**FWC HTC (Atm.) (kW m^{-2} K^{-1})**	**DWC HTC (kW m^{-2} K^{-1})**	**DWC HTC (Atm.) (kW m^{-2} K^{-1})**	**% Improvement**	**% Improvement (Atmospheric)**	**Previously Published Improvement**	**Published Improvement (scaled to atmospheric)**
Water	10.26	11.4	26.85	53.51	162%	373%	120%[150]	484%[161]
Toluene	1.87	2.09	6.88	9.44	270%	355%	450% (LIS)[162]	611% (LIS)[161]
DMF	2.97	--	8.73	--	294%	--	350%[163]	

2.6 Durability and Longevity

As mentioned above, while other surface treatments can yield greater heat transfer enhancements for condensation, these enhancements may not be feasible for actual use conditions because they either degrade rapidly or can easily be damaged. The tests were conducted in accordance with the procedures outlined in section 2.3.4. Abrasion testing was performed to validate the mechanical durability of the polymer brush surfaces. The results of evolution of contact angle for water and hexadecane are shown in **Figure 2.21**. There is a clear degradation in the glassy fluorinated surface compared to the negligible change in contact angle for all the amorphous surfaces. With crystalline surfaces, any defect caused by the abrasion becomes a pinning point where liquid can interact with the underlying substrate. Whereas the advantage of an amorphous coating is that when a defect occurs, the coating is mobile and can cover the exposed substrate so the liquid is still only interacting with the coating.

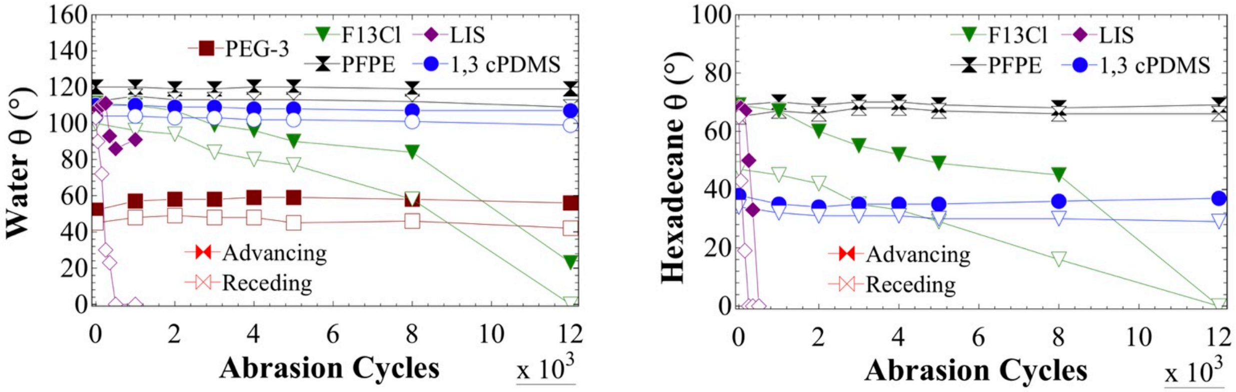

Figure 2.21: Mechanical durability testing where the dynamic contact angles, for water (left) and hexadecane (right), are plotted after a series of linear abrasion cycles for each of the surface coatings in this study. The amorphous polymer brush surfaces displayed negligible change in contact angles after 12,000 cycles, whereas lubricated surfaces degraded in less than 1,000 cycles and the glassy F13Cl degraded in less than 10,000 cycles. Note hexadecane contact angles were not collected on PEG-3 as the liquid fully wets the surface.

A similar trend was seen when testing the chemical stability of these coatings. An important property of any condensing surface is how long it can maintain its performance. As seen above, lubricated surfaces degrade in the matter of a few hours. To validate the stability of these surfaces, they were subjected to continuous condensation of water at a high heat flux. **Figure 2.22** shows that the amorphous coatings maintain condensation performance and remain in dropwise condensation, whereas the glassy F13Cl degraded to filmwise condensation rapidly. This can be attributed to the ability for amorphous surfaces to resist hydrolysis of the coating, and, just as with mechanical abrasion, “repair” any defect spots to prevent exposure of the condensate to the underlying substrate.

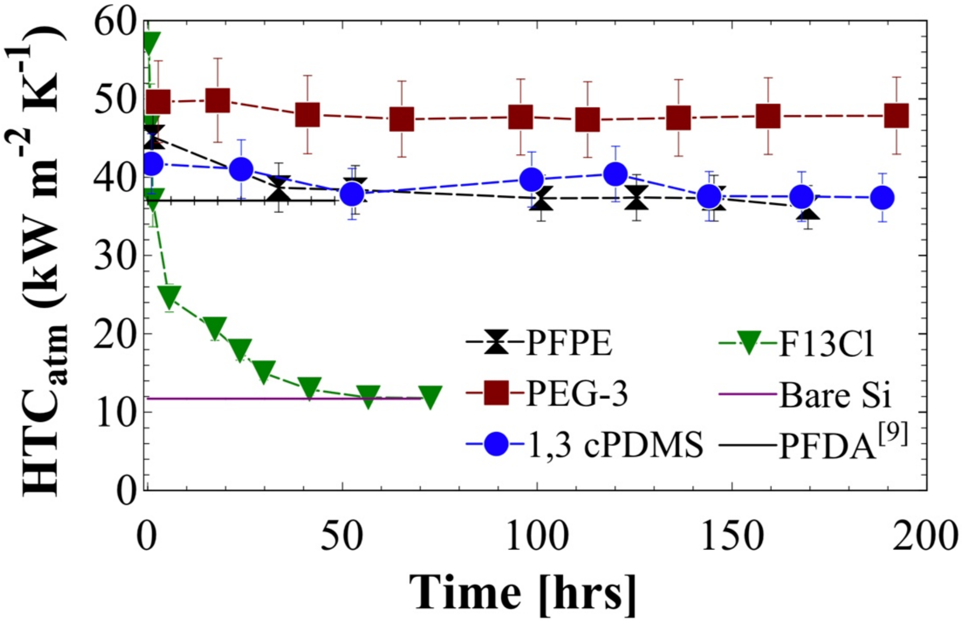

Figure 2.22: Chemical stability of test surfaces based on their ability to maintain condensation performance over extended periods of use. All amorphous surfaces had less than a 10% change in HTC over 200 hours, whereas the crystalline coating degrades to filmwise condensation in less than 50 hours.

2.7 Conclusion

In this study, we demonstrated new design criteria for enhanced heat transfer performance of condensation surfaces. By utilizing thin, amorphous polymer films, the surface energy of the coating can be tuned to maximize the heat transfer characteristics. This combination enables efficient departure of droplets while increasing the nucleation rate. We show that by minimizing contact angle hysteresis, the departure of condensate droplets can become independent of contact angle so the contact angle can be chosen, specific to the condensate, to maximize nucleation. While other studies have shown slightly higher enhancement of heat transfer properties, the coatings identified here are smooth and conformal coatings that could be easily applied to current infrastructure. Additionally, the amorphous coatings exhibited far greater durability and longevity of use, greatly expanding their applicable use cases. This tunable control of condensation demonstrates the importance of hysteresis in the rational design of condensation heat transfer surfaces and a new design and optimization approach with widespread applicability.

Chapter 3

Enhanced pool boiling performance of thermally and mechanically durable diamond-like carbon coating

This chapter is primarily adapted from an article submitted to *Nature Materials* and was part of a collaborative effort with John Heron and Ctirad Uher. Production of the target materials was performed by Trevor Bailey. Deposition and characterization were performed by Peter Meisenheimer, who is an equal first author on the manuscript.

3.1 Introduction

Boiling phase transformation is an important process in a variety of industrial processes and is critical in electric power generation, the world's largest CO_2 emitter. A majority of world energy consumption is used for power generation, with nearly 50% of power generated with a steam turbine cycle.[164,165] Even with the increasing use of renewable energy, steam power generation is still employed across nuclear, geothermal, and solar energy such that steam is expected to grow 25% over the next 20 years.[166] Even marginal improvements in the efficiency of steam generation can lead to the prevention of tons of CO_2 emissions each year.[167]

Boilers in fuel burning power plants are operating at increasingly hotter and hotter temperatures in search of greater efficiency. The next generation of fuel burning boilers will operate in excess of 600℃; this brings with it a necessity for all new materials that are heat stable and can operate at these severe temperatures.[168] A surface coating to enhance the heat transfer coefficient into the operating fluid would lead to reduced material cost, smaller machine footprint, and increased operating efficiency.[169,170]

Despite the shift towards renewable energy sources, the use of steam generated power is expected to continue to grow for the next 20 years, and enhanced surface performance is just as applicable to nuclear and solar thermal power. A major risk in the regular operation of nuclear boilers is the departure from nucleate boiling, or the shift from bubbles nucleating and departing the surface to coalescing and forming an insulating film over the surface (dryout).[171] Dryout of the fuel rods is directly related to their failure, uncontrolled temperature increase, and eventually, meltdown.[172,173] Nuclear boilers are limited in their operating temperature by this critical heat flux (CHF) point when the vapor film forms.[174,175] A non-insulating surface coating that can increase the critical heat flux would allow for greater operational efficiency of nuclear power production.

The efficiency of a boiling surface is quantified by the heat transfer coefficient (HTC), the ratio of heat flux across the surface and the superheat temperature, and the critical heat flux (CHF), the point at which bubbles coalesce to form a vapor film across the surface, sometimes referred to as dryout or departure from nucleate boiling.[83] Prior research on boiling has taken two directions, surface texturing and suspended nano-particulates in the fluid.

Numerous studies have been published regarding pool boiling on micro- and nano-textured surfaces, which has been shown in simultaneously increase HTC and CHF.[176–190] The heat transfer coefficient is primarily enhanced by surface texturing through an increase in both wetted area and nucleation sites. Since the heat flux is a measure of energy per unit area, it would follow that an increase in that area would lead to more energy transfer. In studies, heat flux is calculated by the projected area though, so surface texturing would increase the surface area in contact with liquid, but not in the reporting of heat flux. This increase in heat flux being correlated to the increased wetted surface area has been shown in multiple studies.[12,191,192] Not all increases in HTC can be attribute to the increase in wetted surface area, there is also a correlation with an increase in nucleation sites. Trapped air cavities act as additional activation sites for nucleation, and surfaces with nano-texturing creates additional cavities for air to be trapped.[193–195] These extra cavities increase the nucleation density of the surface, and since the heat transfer coefficient is correlated with the volume of liquid evaporated, the HTC increases with it.[196,197] The surface texture has an equally important role in enhancing CHF through both hydrodynamic pumping, and when textured, can create pathways for fresh liquid to wick in. Both mechanisms rely on expeditiously bringing cooler liquid across the surface to prevent dryout of any regions. When the texturing is smaller than the capillary length, the structure can wick liquid in from the sides and deliver it to the middle of the sample, which typically reaches dryout first. [109,198,199] While wicking utilizes the structure to draw in liquid from the sides, the surface texture can also be patterned to create non-nucleating regions that develop into liquid pathways for liquid to come down to the surface while vapor pathways have the enhanced nucleation sites.[8,105]

Fluids with very small fractions of nanoparticles in them have been shown to also increase HTC and CHF, though not as significantly as surface texturing. This is because the nanoparticles enhance the heat transfer for many of the same reasons. When a bubble forms, the particles suspended in the liquid, deposit on the surface and introduce increased roughness which increases the wicking and nucleation sites.[200–207] The nanofluids also see an increase in HTC due to the reduced surface tension of the liquid and increased fluid conductivity, but these improvements are small compared to surface texturing.[208–210] Despite these improvements, the enhancement from nanofluids is temporary as the nanoparticles eventual start scaling on the surface which leads to a decline in performance.[211–213]

Both surface texturing and nanofluids can add ever increasing complexity to the surface to enhance boiling heat transfer properties, but this deviates from common use cases and inhibits scalability. Therefore, this study focused on developing a smooth surface that can enhance HTC and CHF. This would not only be more scalable to industrial applications but could be conformally coated to any surface texturing to further enhance performance.

3.2 Design Criteria for Boiling

3.2.1 Optimized Surface Properties

There are two important physical properties for a boiling surface, a high heat stability and low thermal resistance. In all of the previous boiling studies, the surfaces are untreated, high surface energy materials. Self-assembled monolayers (SAMs) have been extensively used for other heat transfer applications for their ability to control the wetting properties and are sufficiently thin such that the conductivity becomes negligible.[131,214] There are few studies that reliably control the wettability of the surface, and those that do, typically do so with a fluoropolymer like Teflon (PTFE).[105,215,216] Unfortunately, these types of coatings are unsuited for industrial boiling due to the extreme operating temperatures in excess of 400°C; silanes and thiols begin degrading at temperatures well below this and even PTFE degrades at 400°C.[217,218] Any coating designed for boiling applications requires greater heat stability that is displayed by polymer and silane options, and it should be able to maintain performance up to at least 700°C to be viable for industrial boilers.

Low thermal resistance is the other critical design parameter for an efficient boiling surface. One of the major pitfalls of nanofluid enhancement is that the improvement is only temporary, as boiling progresses, the nanoparticles deposit on the surface creating a scale. This scale increases the thermal resistance for heat transfer and reduces the HTC as shown in **Figure 3.1**.[213] Just as the layer of scale inhibits heat transfer, any polymer coating would also reduce the heat transfer performance. Unfortunately, the rate of scale deposition increases with temperature making nanofluids even less viable for high temperature industrial applications.[219] Resistance is also important when considering PTFE, which is stable in lower temperature applications, though the resistance makes it an unviable solution. Consider a moderate heat flux of 200 kW m^{-2} across a 100 μm layer of PTFE ($k = 0.25$ W m^{-1} K^{-1}), the result would be an 80°C temperature drop across the PTFE layer nullifying any performance advantage it may otherwise produce.[220]

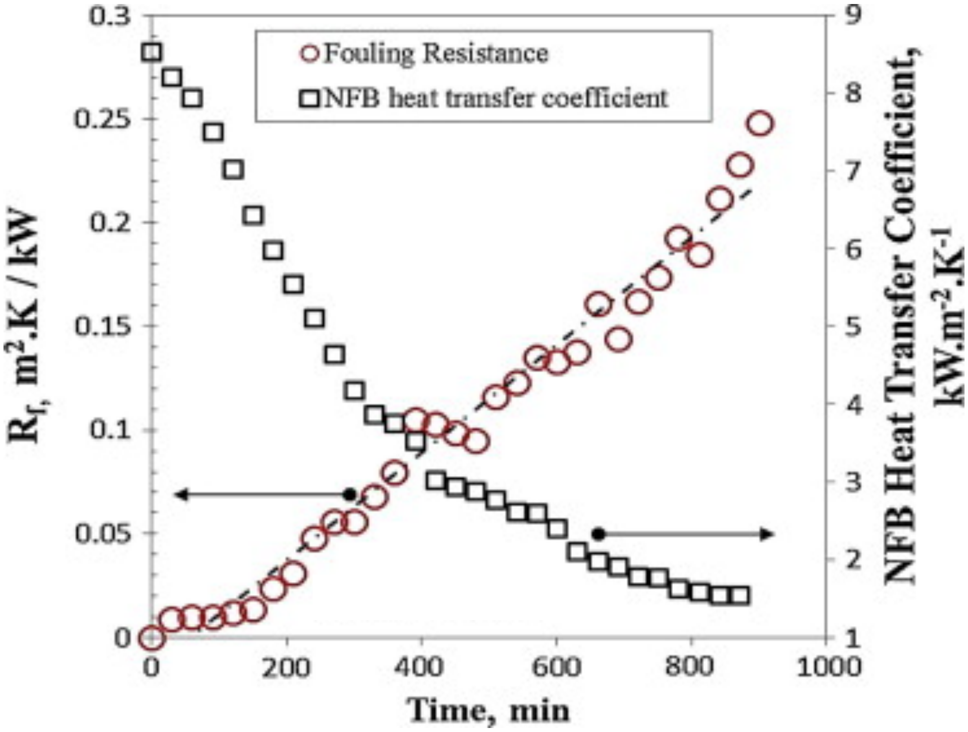

Figure 3.1: Correlation between thermal resistance of the scale and the heat transfer coefficient. The progressive deposition of scale on the surface has the same effect of any thick polymer coating in inhibiting heat transfer performance. Figure is adapted from study in *Experimental Thermal and Fluid Science.*[213]

3.2.2 Surface Energy

As described in section 1.4.2, the Gibbs free energy for a bubble to nucleate on the surface is highly dependent on the contact angle of the liquid on the surface such that as the contact angle increases, the Gibbs free energy for nucleation decreases. This trend can be captured by the nucleation density of a surface, which is shown as an inverse in **Figure 3.2**.[106,221] This in contrasted against the contact diameter of a bubble on the surface.[222] As the contact angle increases, the nucleation density increases, and the bubbles spread across the surface more.

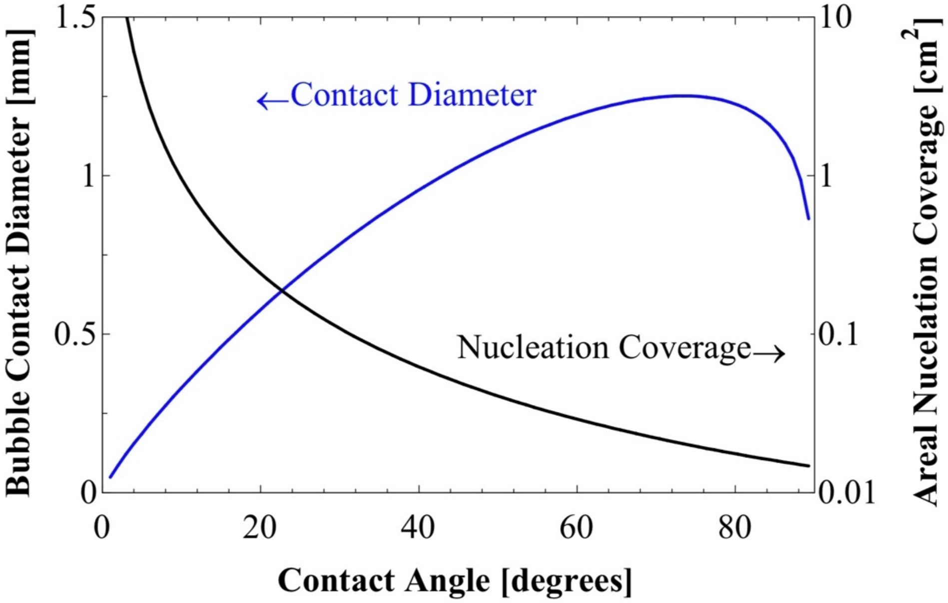

Figure 3.2: Plot comparing the areal nucleation coverage to the contact diameter for bubbles. The areal nucleation coverage represents the average distance between nucleation sites and is the inverse of the nucleation density. The contact diameter relates to the spreading of bubble on a surface. Since the vapor phase is now contained in a liquid, the trend is opposite of a droplet in that a bubble on a hydrophobic surface spreads whereas a bubble on a hydrophilic surface does not.

These trends in **Figure 3.2** can be directly correlated to the heat transfer coefficient and critical heat flux for a surface. With the enthalpy of vaporization significantly higher than the specific heat of a liquid, the amount of thermal energy transferred to the liquid is directly related to the amount of vapor that is formed. The nucleation density represents the rate of bubble formation and therefore is directly correlated to the heat transfer coefficient. As the bubbles spread out more and more, they also cover more of the surface in a vapor, and the narrower spacing between nucleation sites which leads to greater coalescence of bubbles. The contact diameter can be directly related to the onset of the critical heat flux, with some influence by the nucleation density. Therefore, a general correlation can be made that as the contact angle increases, the HTC increases and CHF decreases, and this has been modeled in **Figure 3.3**.

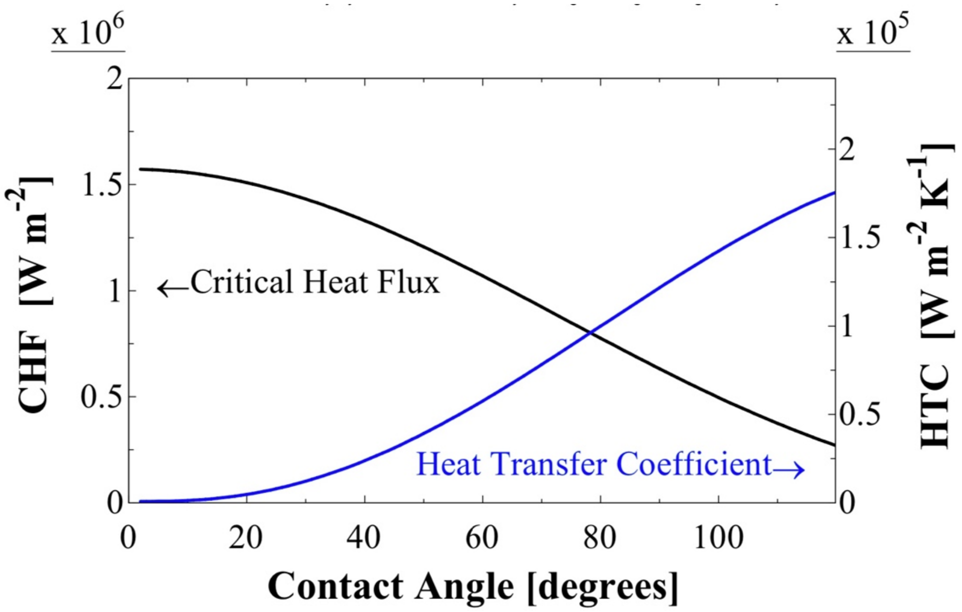

Figure 3.3: Correlation between the heat transfer coefficient and critical heat flux to the contact angle of the surface. This is a general estimation made form numerical models, though it does not account for the hysteresis of the surface.

From these models, a balance between high HTC and high CHF can be struck when the contact angle is between 70° and 90°, though it would appear that both HTC and CHF cannot be increased simultaneously. While these models can provide general direction of these two performance factors, no model incorporates the influence of hysteresis.

3.2.3 Contact Angle Hysteresis – Bubble Growth and Departure

Although the contact angle hysteresis is not incorporated into any of the numerical models, it is critical when considering the growth and departure of bubbles. Just as the hysteresis is determinant in the mobility of droplets on a surface, it is also important in the consideration of bubbles moving on a surface. As described in Section 1.4.2, the growth and departure of bubbles is the most critical consideration in the performance of a boiling surface. The rapid growth, departure, and re-nucleation of a new bubble are the driving factors of the heat transfer coefficient. Since the HTC is dependent on the volume of liquid vaporized, the faster a bubble grows and departs, the more liquid that can be vaporized, and therefore the higher the HTC. Similarly, the critical heat flux is also highly dependent on the behavior of bubbles on the surface. If bubbles grow too large, they cover the surface in a vapor layer which accelerates the onset of filmwise boiling. This can be attributed to either the contact angle being too large such that a relatively small bubble, in volume, spreads out and covers a large area of the surface, or to bubbles that are delayed from departing the surface and cover the surface in a vapor layer for long periods of time. It is clear that any surface that can accelerate the rate of bubbles growing, departing, and re-nucleating on the surface would thereby increase the HTC and CHF.

There is no prior study on the influence of hysteresis on a boiling surface, primarily because it is difficult to create tuned surfaces that can sustain their surface wettability during a boiling test. The only known study that assesses mildly hydrophilic surfaces ($30° < \theta < 90°$) does so with copper that has been oxidized to varying degrees, but this leads to high hysteresis, which will be shown later to inhibit heat transfer performance.[223,224] Although we cannot quantify the effects of contact angle hysteresis in this work, we can show the qualitative analysis that we use to structure the design parameters for a good boiling surface.

The first key to under is the growth of a bubble on the surface. As mentioned above, the behavior of a bubble is the inverse of that of a droplet, so the growth of a bubble is associated with the recession of the liquid contact line. Thus, the force for a bubble to grow and expand the contact area on a surface is dominated by the receding contact angle such that:

$$F_{expand} = \gamma w \cos \theta_{rec} \tag{3.1}$$

As the bubble grows larger, there is a tension force around the surface area of the bubble causing it to expand and this is counteracted by the force to move the 3-phas contact line across the surface (dictated by the receding contact angle. Increasing the receding contact angle, though maintaining it below 90°, would decrease this force and allow a bubble to more easily increase its contact area. Though, this would seem counter intuitive to what was described above because an increased contact area would cover more of the surface with vapor. That brings in the second consideration for the bubble in that we want the bubble to grow quickly. The evaporation of liquid primarily occurs as the 3-phase contact line which is the perimeter of the contact area.[225,226] This rate of evaporation of liquid to vapor (V_m) in the bubble has been modeled:[227]

$$V_m = \frac{2}{3}\pi R^3 \left(\frac{2}{C_2}\frac{\Delta T}{\phi}\frac{\nu_l^{\frac{1}{2}}}{C_1}\right) \tag{3.2}$$

In this model, C_1, C_2, ϕ, and ν_l are all liquid dependent, so they would not vary with the surface. The equation can be simplified down to $V_m \propto R^3$, where R is the radius of the contact area. Thus, a large contact area is actually desired as it rapidly vaporizes liquid and expands the bubble volume.

Though there is a limit to the desirability of bubbles to quickly grow in that they also need to quickly depart the surface. If a bubble expands and then remains on the surface, then it leads to dryout. This brings us to the final consideration with hysteresis that the bubble needs to quickly depart the surface. Opposite of bubble growth, the departure of a bubble is driven by the advancing contact angle as the water contact line progresses across the surface to eventually cover up the dry area where the bubble is in contact.[228] Overcoming the surface tension forces, the buoyancy force is now dominates; although buoyancy existed during bubble growth, in that phase, it was minimal, and the recession of the contact line was dominated by surface tension. This combined force can be represented by:

$$F_{contract} \;=\; \gamma\, w \cos\theta_{adv} + \frac{F_{buoyant}}{\tan\theta_{adv}} \tag{3.3}$$

Where the buoyant force is a function of the bubble volume (V_b) and the liquid and vapor densities (ρ):

$$F_{buoyant} = V_b(\rho_l - \rho_v)g \tag{3.4}$$

Accordingly, the force for the contact area to shrink is driven by the advancing contact angle and the force is minimized when the advancing contact angle is very small. Since the advancing contact angle must be larger than the receding contact angle, a dilemma arises in which a large receding contact angle and small advancing contact angle is most desirable. Since this is impossible, the best combination would be for the two angles to be identical. Therefore, we can get to the assumption that minimizing hysteresis is the best possible fulfillment of this dilemma such that $\theta_{rec} > \theta_{adv} > 90°$ and $\Delta\theta \approx 0°$. Combining this with our previous criteria for a moderately hydrophilic surface $50° < \theta < 90°$, we can assume that a surface with an advancing contact angle between 50° and 90° should balance good heat transfer coefficient and critical heat flux, while potentially being able to simultaneously increase both if the contact angle hysteresis is reduced.

3.2.4 Diamond-like Carbon

Diamond-like carbon (DLC) is a class of materials derived from metastable amorphous carbon-carbon bonding. It is characterized by a combination of sp^2 (graphitic) bonds and sp^3

(diamond) bonds. This combination of bonding provides a material significantly easier to create than diamond, but exhibits similar properties to diamond like exceptional physical, mechanical, and inert properties. Though not to the same extent as diamond, DLC is an excellent compromise between the favored properties of diamond and the cost effectiveness of graphite. DLC was identified as an exceptional candidate for boiling heat transfer because it exhibits good stability at high temperatures and can be doped with various elements to control its wetting dynamics.

Diamond-like carbon typically has an indentation hardness of 5-30 GPa, depending on the constituents and degree of sp^3 bonding present. While there are numerous variables that contribute to the difference in hardness exhibited by various DLC surfaces, the difference can typically be attributed to the dopants, deposition process, and degree of sp^3 bonding achieved. These parameters will be examined further in the methods section, but the high hardness of DLC is associated with the high degree of abrasion resistance. DLC has been shown to resist many thousands of harsh abrasion cycles with minimal deformation or material removal.[229] Additionally, DLC has also shown high temperature resistance, maintaining performance above 500°C.[230,231] Though there has been some evidence that fully carbon diamond-like carbon begins to degrade and oxidize above 500°C, the films can be stabilized with dopants, like silicon, that can retard the degradation of the material.[232] All-together, DLC exhibits very high mechanical and thermal resistance that is ideal for a thin boiling surface.

Although DLC does not exhibit very high thermal conductivity (1-3 $W\ m^{-1}\ K^{-1}$), just as with silanes for condensation, the conductivity becomes negligible at sufficiently small thicknesses (< 1μm).[233] With the high abrasion and chemical resistance inherent with DLC, coatings on the scale of just a few nanometers are sufficient as the additional protection of bulk materials is not necessary.[234]

3.3 Materials, Methods, and Characterization

3.3.1 Pulsed Laser Deposition (PLD)

DLC can be deposited in a variety of ways including plasma enhanced vapor deposition (PECVD), ion beam deposition, magnetron sputtering, and pulsed laser deposition. We have deposited utilizing pulsed laser deposition (PLD) which directs a high-powered laser at a carbon-based target in a vacuum chamber and ablates material in a directed flux towards a substrate. PLD offers advantages over PECVD, which is more commonly used for DLC deposition. Particularly the PECVD process employs hydrocarbon process gases for the carbon source which lead to hydrogenation of the film and less control over final stoichiometry. Hydrogen free diamond-like carbon is associated with a higher degree of sp^3 bonding and therefore a harder film.[235] PLD also creates higher energy carbon atoms that imping on the substrate which trends toward a higher degree in sp^3 bonding.[236]

Samples were deposited from stoichiometric targets by ablation from a 248 nm KrF excimer at 30 °C and in 20 mTorr Ar for 20,000 shots. Samples were deposited at a pulse rate of 20 Hz. Final film thickness of samples was approximated by a lift-off photolithography process, after which height was determined using AFM. The thickness correlation was approximately 10 shots per Å deposited for pure carbon DLC, and 12 shots per Å deposited for Si-DLC.

3.3.2 Target Forming

The pure carbon target was cut from a graphite rod 25mm in diameter. Silicon doped targets discs, 20 mm diameter by 5 mm high, were formed using spark plasma sintering. The target stoichiometry was achieved by mixing graphite powder with silicon carbide powder to achieve the desired carbon to silicon ratio. The mixed powder was consolidated in a 20 mm diameter graphite die lined with graphite paper under an axial compressive stress of 50 MPa in vacuum inside a spark plasma sintering furnace (KCE – FCT HP D 10 – SD spark plasma sintering furnace) for 10 minutes at a sintering temperature of 1700°C. After cooling and removal, targets were prepared for deposition by sanding with progressively finer sandpaper, starting at 500 grit, and progressing through 1000, 1200, 1500, to finish with 2000 grit sandpaper.

3.3.3 Contact Angle and Surface Energy

Advancing and receding contact angles for the liquids were obtained from a sessile drop method using a Ramé-Hart 200 F1 contact angle goniometer. A dispensing needle was placed just above the substrate surface and a 10 µL droplet was suspended from the needle. The volume of the droplet was then increased to obtain advancing contact angles and decreased to obtain receding contact angles. DROPImage Advanced software was used to obtain the contact angle using a circular drop fit. Three points on each substrate were measured, and the mean value reported in **Figure 3.4** with a standard error of ±2°.

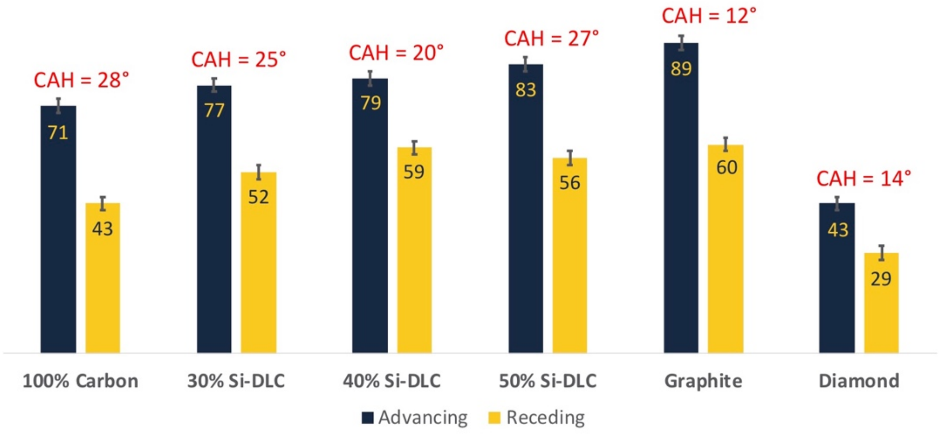

Figure 3.4: Dynamic water contact angles for each of the films deposited in this study. The contact angles reported in other studies is also shown for comparison for graphite (pure sp^2 bonded)[237] and diamond (pure sp^3 bonded)[238].

To estimate the surface energy of each substrate, we used the Owens-Wendt Method.[35] After depositing each surface, the Owens-Wendt analysis was performed with water (dispersive surface tension, γ_{lv}^{d}=21.1 mN m^{-1}, and polar surface tension γ_{lv}^{p}=51.0 mN m^{-1}) and diiodomethane (γ_{lv}^{d}=50.8 mN m^{-1} and γ_{lv}^{p}=0.0 mN m^{-1}). Using the mean static contact angles of each liquid on the surface, the dispersive (γ_{sv}^{d}) and polar (γ_{sv}^{p}) components of the solid surface energy can be calculated by:

$$2\begin{bmatrix} \sqrt{\gamma_{\text{water}}^{d}} & \sqrt{\gamma_{\text{water}}^{p}} \\ \sqrt{\gamma_{\text{hexadecane}}^{d}} & \sqrt{\gamma_{\text{hexadecane}}^{p}} \end{bmatrix}\begin{bmatrix} \sqrt{\gamma_{sv}^{d}} \\ \sqrt{\gamma_{sv}^{p}} \end{bmatrix} = \begin{bmatrix} (1+\cos\theta_{\text{water}})\gamma_{\text{water}} \\ (1+\cos\theta_{\text{hexadecane}})\gamma_{\text{hexadecane}} \end{bmatrix} \tag{3.5}$$

Table 3.1: The advancing (θadv) and receding (θrec) contact angles are reported along with the calculated polar (γp) and dispersive (γd) surface energy determined by the Owens-Wendt Method, for each of the deposited films.

Si Ratio	**θ_{adv} (°)**	**θ_{rec} (°)**	**γ_d (mN/m)**	**γ_p (mN/m)**
100% C-DLC	71 ± 2	43 ± 3	38 ± 1.1	12.4 ± 1.2
30% Si-DLC	77 ± 3	52 ± 4	33 ± 1.3	11 ± 1.1
40% Si-DLC	79 ± 3	59 ± 3	32 ± 1.2	9.3 ± 1.1
50% Si-DLC	83 ± 2	56 ± 2	30.5 ± 1.0	7.2 ± 0.9

3.3.4 Nano-indentation

Hardness was measured by nanoindentation using a Hysitron TI 960 TriboIndenter fitted with a Berkovitch probe. Indentation was performed on each sample in 5 different regions of the sample, and to a depth of 50nm, or about 20% of the film thickness, to avoid any contribution of the underlying silicon substrate. The hardness was calculated from the unloading curve of the force-displacement plot following principles published by Oliver and Pharr.[239] The fit function was calibrated prior to each use by indenting a fused quartz standard. The hardness for each of the deposited films, as measured by nano-indentation, is shown in **Figure 3.5**.

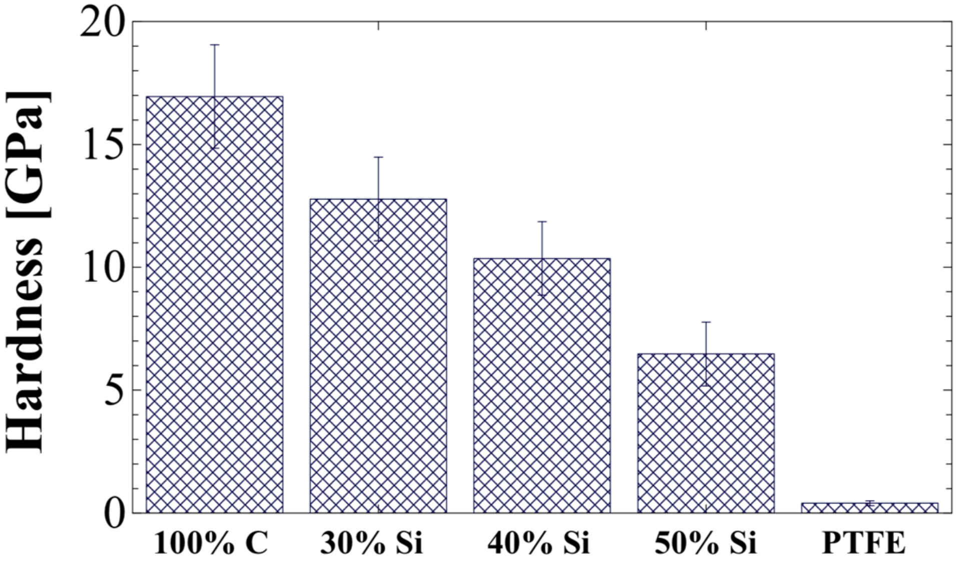

Figure 3.5: Hardness of each deposited film as measure by nanoindentation. The hardness for PTFE is provided for comparison, as reported in journal *Strain*.[240]

3.3.5 Abrasion

The abrasion testing was performed using a Taber Model 5750 Linear Abrader with a CS-10 tip (~6.6 mm diameter), which has aluminum oxide particles embedded in a rubber matrix, and 500g of applied load, equivalent to about 150 kPa of pressure. The abrasion head was moved across a one-inch length of the surface in a reciprocating fashion at 60 cycles/min. After a set number of abrasions, the system was stopped, the surface was rinsed with acetone, IPA, and water, and the contact angles with water were measured at three different places along the 1-in abrasion length. The sample was then placed back into the machine for additional abrasion cycles, and the cycle was repeated until the surface displayed significant degradation in contact angles compared to the as deposited.

3.3.6 Additional Characterization

X-ray photoelectron spectroscopy (XPS) was performed on the samples to measure the relative composition of the samples and the chemical bonding structure. Spectra were obtained using a Kratos Axis Ultra XPS with monochromated Al source and using a charge neutralizer. Spectra were taken from 0 to 500 (Si-DLC) eV to determine relative composition of each of the four films in **Table 3.2**. High-resolution scans were taken about the C 1s peak to quantify sp^2/sp^3 character; data was processed and fit in CASAXPS analysis software. The bonding curves along with the processing and fit are displayed in **Figure 3.6** for the 100% carbon and 40% Si-DLC.

Table 3.2: Summary of the carbon and silicon composition of each of the deposited films, as measured by XPS.

Composition	Carbon Content (%)	Silicon Content (%)
100% Carbon DLC	100	0
30% Si-DLC	78.4	21.6
40% Si-DLC	63.7	36.3
50% Si-DLC	54.6	45.4

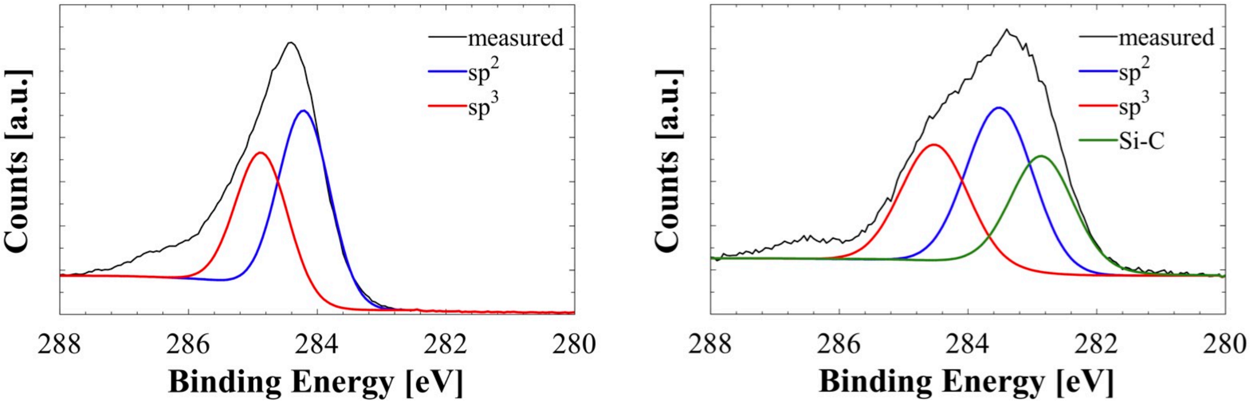

Figure 3.6: Spectra collected for the 100% carbon DLC sample (left) and the 40% Si-DLC (right), which exhibited the lowest hysteresis of the deposited films. The black line represents the as measured spectra, with the sp^2 and sp^3 curves fit in post processing.

Atomic force microscopy (AFM) was performed to measure roughness and thickness of the films. Samples were measured using and ND-MDT NTEGRA Prima AFM in contact mode and analyzed using Gwyddion AFM analysis software. As described in the deposition method, part of the film was lifted-off with photolithography so the thickness of the deposited film could be measured with AFM. AFM was also used to measure the roughness of the films. **Figure 3.7** shows the evolution of the roughness of the 40% Si-DLC film. Even after deposition, the film is extremely smooth with an RMS roughness of just 1.7 µm, but the film gets even smoother with longer and longer annealing times at 700°C. After 50 hours at 700°C, the film has an RMS roughness of 0.89 µm. We believe the smoothing of the film isn't caused by any actual mobility of the material, but rather any substances that are laying on the surface, but not part of the actual amorphous carbon, get baked off during the annealing leading to fewer larger particulates on the surface.

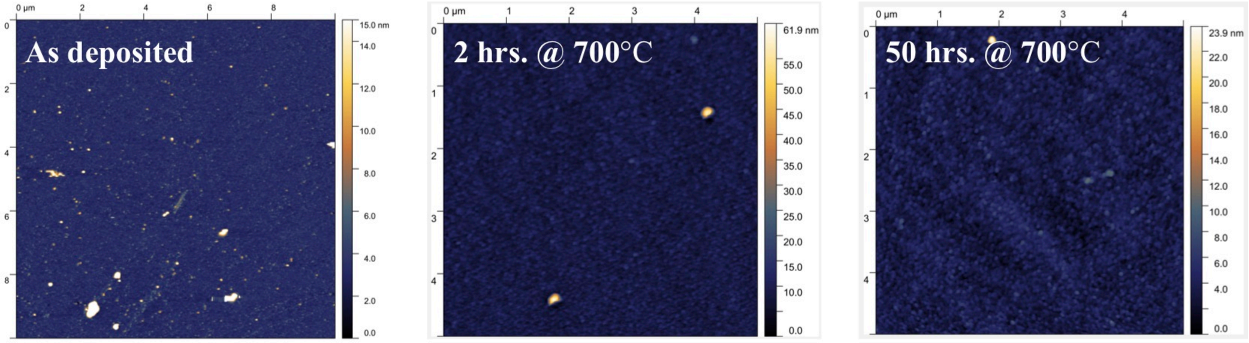

RMS = 1.7 µm **RMS = 1.1 µm** **RMS = 0.89 µm**

Figure 3.7: Evolution of surface roughness of the 40% Si-DLC sample after deposition (left), after 2 hours at 700°C (middle), and 50 hours at 700°C. The longer annealing time produces an extremely smooth film.

3.3.7 Heat Transfer Measurements

The testing apparatus for boiling heat transfer measurements is shown in **Figure 3.8** with a schematic of the same structure in **Figure 3.9**. The apparatus consists of a column of copper that contains immersion heaters which provide a thermal source to the system, up to 2 kW of heat. The immersion heaters are connected to a continuously variable voltage controller so the heat flow can be controlled from 0-100% power. The thermal energy is conducted up the copper to the top which contains the substrate. Between the heaters and the substrate are four equally spaced thermocouples which measure the temperature at each point. Surrounding the copper is a Teflon jacket to insulate and prevent any convection. Since the thermal conductivity of Teflon is about 200x lower than copper, any conductance through the Teflon can be neglected.

Surrounding the exposed substrate is a column of liquid contained within a quartz cylinder and stainless-steel plates on each end. At the top of the column is a port leading to a condensation column. The recondensed liquid returns to the column of liquid at the base of the lower containing plate. The recondensed liquid is returned to the liquid to maintain a constant liquid level throughout the collection for the heat curve. Any variation in the height of the liquid would affect the pressure at the surface and thereby change the forces acting on bubbles. Lastly, an immersion heater is submerged in the liquid and connected to a PID controller. The PID controller used a thermocouple in the liquid to maintain a liquid temperature of 99°C; this ensures the heat transfer from the substrate was due solely to the vaporization and not from convective heating of the liquid.

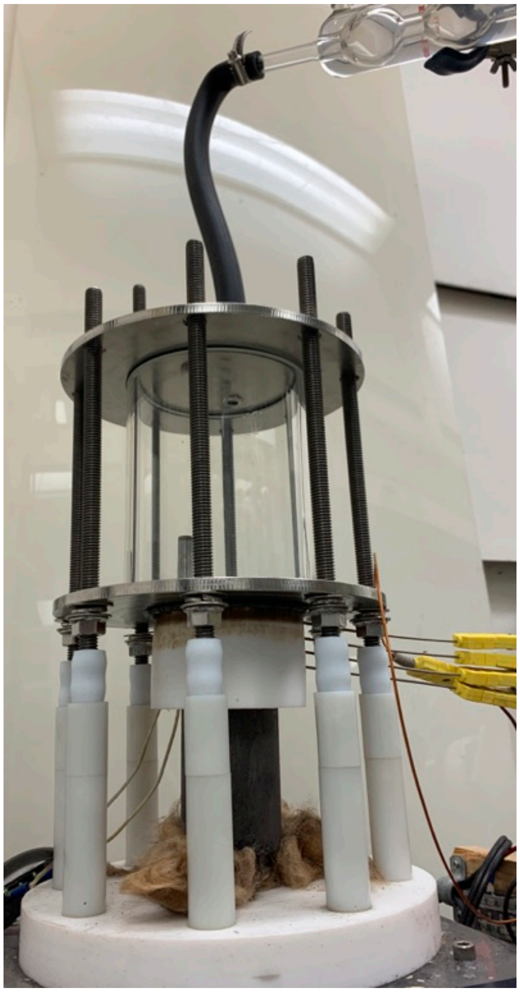

Figure 3.8: Image of the testing apparatus that was used for heat transfer measurements. The chamber containing the liquid is surrounded by a quartz cylinder between two stainless steel plates. The sample is inside this cylinder with the heat source embedded in copper and extending below the bottom plate. At the top is a tube leading to a condensation column that fees the recondensed liquid back into the liquid chamber.

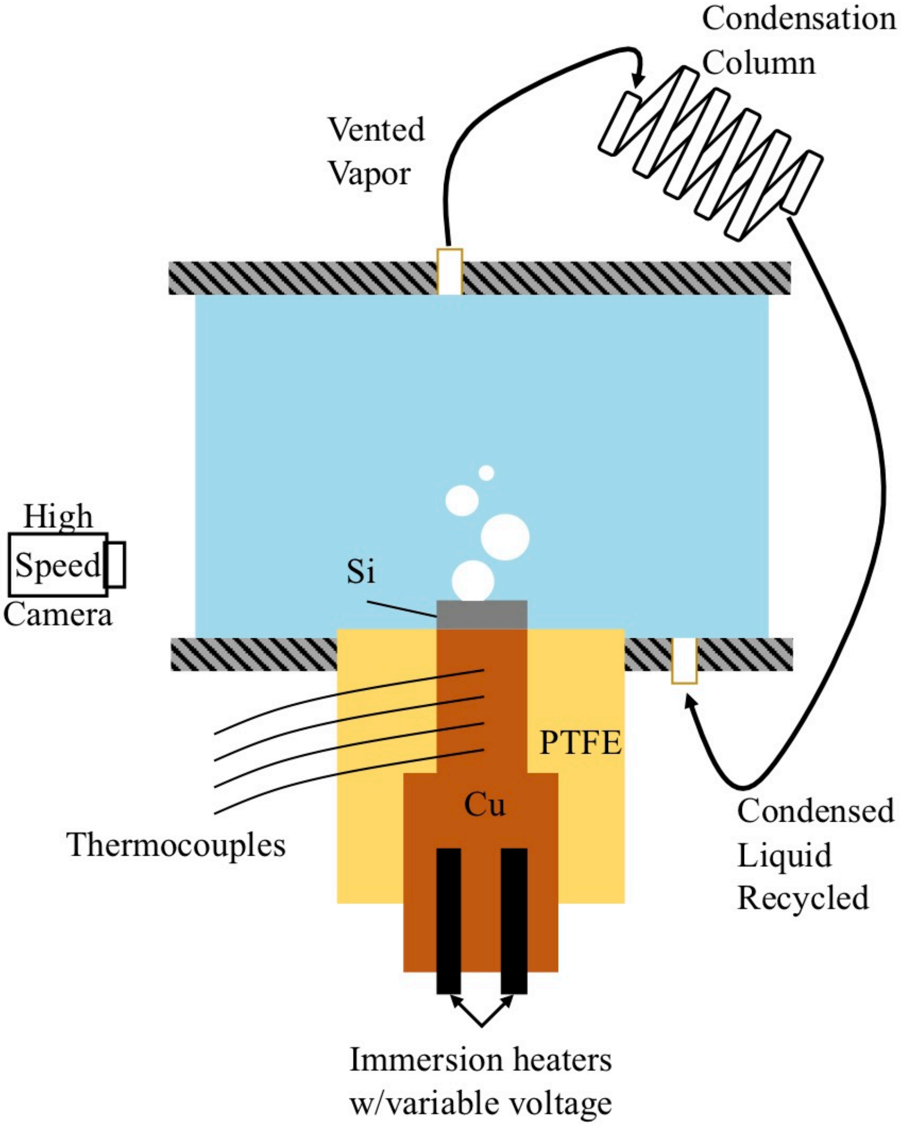

Figure 3.9: Schematic of the apparatus used to collect heat transfer measurements. Heat is added from the immersion heaters at the base of the copper. As the heat conducts up to the sample, the thermocouples measure the heat flux. The heat then transfers from the sample into the liquid in the chamber, vaporizing it. The vapor leaves the chamber at the top to condensation column where the vapor condenses, and the liquid is then returned to the base of chamber so the liquid level does not vary during the experiment.

A silicon substrate (2 cm x 2 cm) is soldered to the copper heating column, as shown in **Figure 3.10**, using a tin and lead solder; we assume zero contact resistance in our calculations as the solder should provide a good heat transfer interface. On the other end of the heating column are 4 immersion heaters connected to a variable AC power supply. By controlling the input voltage, the thermal flux can be varied. Between the heaters and substrate are 4, equally spaced, thermocouples from which the heat flux can be determined based on the thermal conductivity of copper and the temperature difference between the thermocouples. Lastly, the surface temperature can be extrapolated from the thermocouple measurements, heat flux, and conductivities of copper and silicon. The copper is insulated by a Teflon jacket to prevent any lateral heat transfer since the thermal conductivity of Teflon is less than 1% of that of copper. The Teflon jacket is mounted under the lower stainless-steel plate such that the soldered substrate is level with the top of the steel plate. Water is contained in a column above the steel plate such that the substrate is exposed to the liquid.

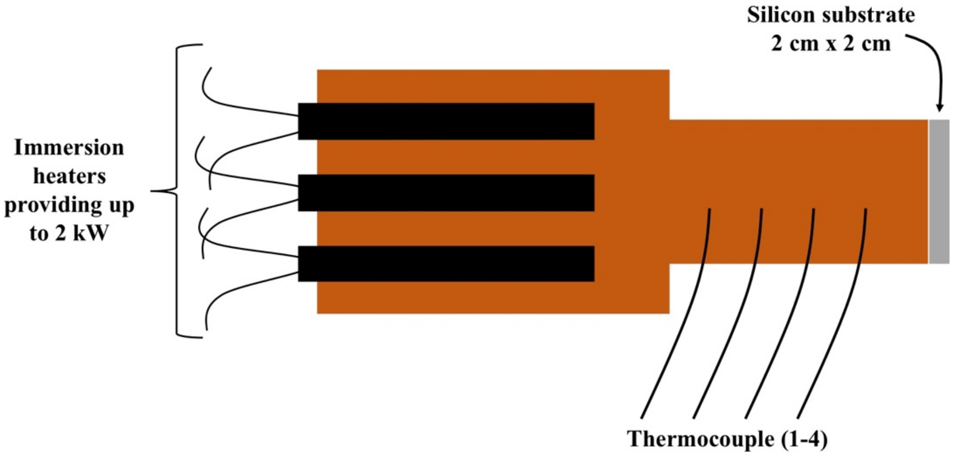

Figure 3.10: The copper is the most critical portion of the apparatus. The immersion heaters in the base provide the heat which is transferred into the liquid from the substrate opposite the heaters. The data is collected from the thermocouples to determine the heat flux and surface temperature.

To create the heat curve, data is collected as the variable power source is adjusted. The variable power supply is set to 10% power and the system allowed to reach steady state. Once the thermocouples reach a steady state temperature, the temperature readings of the thermocouples are recorded (averaged over 60 seconds with 100 readings measured per second). A linear fit was used to calculate the average temperature variation over the measurement length such that the heat flux could be calculated by:

$$q'' = -k_{cu}\frac{dT}{dx} \qquad (3.6)$$

The surface temperature could then be extrapolated by estimating the temperature drop from the thermocouple nearest the substrate (T_4) to the substrate surface as follows:

$$T_{surf} = T_4 + \Delta T_{Cu} + \Delta T_{Si} \tag{3.7}$$

The temperature drop through the copper, between the topmost thermocouple and the top of the copper (17.5 mm) can be easily calculated from the heat flux previously calculated:

$$\Delta T_{Cu} = \frac{q''}{k_{cu}}(17.5) \tag{3.8}$$

Lastly, the temperature drop through the silicon can be calculated from the same heat flux, since the heat flux is constant regardless of material and the thickness of the silicon substrate (500 μm):

$$\Delta T_{Si} = \frac{q''}{k_{Si}}(0.5) \tag{3.9}$$

The conductivity of copper is nearly constant at 400 W m^{-1} K^{-1}, but the conductivity of silicon is more temperature dependent in the working range for these experiments so it was estimated by:[149]

$$k_{Si} = 150\left(\frac{T_{surf}}{300[K]}\right)^{-4/3} \tag{3.10}$$

Based on these calculated values, the heat flux (q'') and surface temperature were used to determine the heat transfer performance of the surface. With the heat transfer coefficient being determined by the slope of the linear fit when heat flux (vertical axis) is plotted against surface subcooling (horizontal axis). The surface superheat (δT) was calculated from the surface temperature and vapor temperature (T_{vapor}) assumed to be 100°C since the experiments were conducted at atmospheric pressure:

$$\delta T = T_{surf} - T_{vapor} \tag{3.11}$$

After each data collection at the incremented power ratio, the variable power supply was then incremented up with additional readings collected after steady state of each incremental increase in power. As the heat flux approached the critical heat flux, the power was increased in smaller and smaller increments to capture the CHF, once the surface formed a vapor film and the CHF was reached, the temperature readings increased rapidly, and the power was cut to the system. The last stable temperature measurement was used as the CHF point. The heat flux was then plotted against the surface superheat with the heat flux on the vertical axis and δT on the horizontal axis. The HTC was determined by the average slope of the plotted heat curve.

It is important to note the size of the sample chosen for this study (2 cm x 2 cm). A study was performed that compared the critical heat flux that can be achieved by identical surfaces to the length of a square heated surface with the plot adapted in **Figure 3.11**. As the length gets shorter and shorter, the critical heat flux increases exponentially, but the increases levels off after the heater length is 2 cm or longer. Therefore, the length of the sample chosen in this study is 2 cm to avoid this length influence in artificially inflating the CHF value. It is also an important consideration when comparing to other studies as numerous pool boiling studies utilize heated surfaces less that 2 cm long, some down to just 5 mm. Although they display very high heat fluxes, it is important to put the improvement in context, there may be specific applications that these short lengths are valuable, but in consideration of industrial boilers, long length scales should be considered.

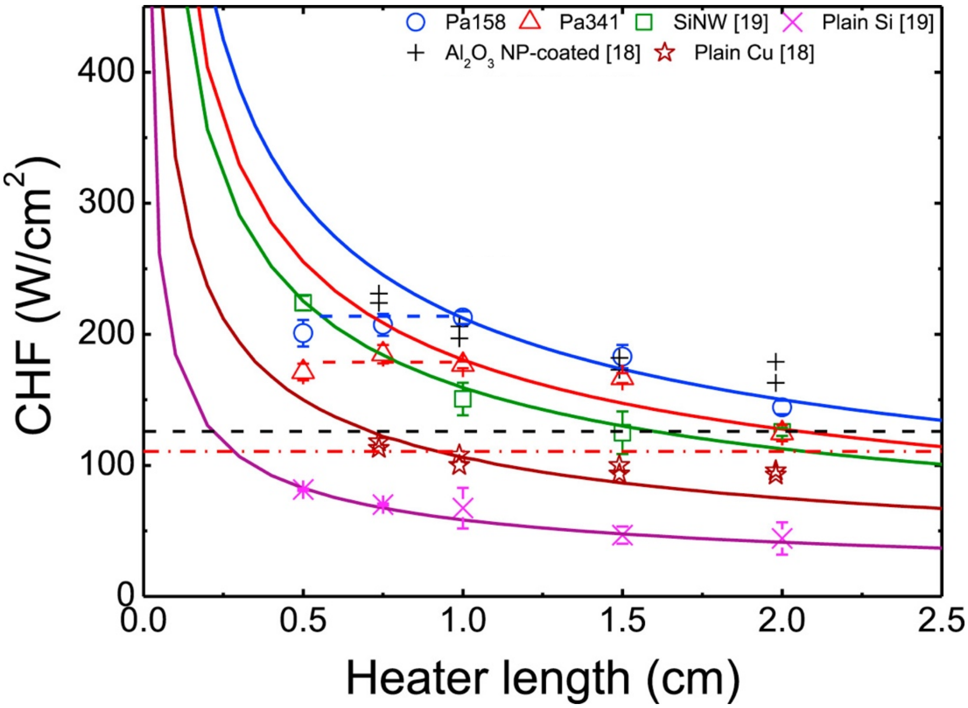

Figure 3.11: Plot comparing the critical heat flux achievable by identical surfaces to the length of the heated surface. As the length of the heated surface decreases, the critical heat flux that the surface can achieve increases in an exponential fashion. Steady state is reached when the heater length is approximately 2 cm or longer. Figure is adapted from a study in the *International Journal of Thermal Sciences*.[241]

3.3.8 High Speed Imaging

High speed videos on bubbles departing were imaged using a Fastec Imaging HiSpec camera with a 105mm lens attached. Videos were taken at 1,000 frames/sec to provide each image as 1 millisecond in time. All bubble analysis was done when the surface heat flux was at a constant 1.5 kW m^{-2} to focus on a singular bubble and this provided a surface in which a singular nucleation point was consistently nucleating, growing, and departing a bubble. Length measurements were performed using ImageJ, and in each video, a 3mm diameter metal disk was suspended in the liquid to provide a scale reference for image analysis to measure lengths.

Bubble nucleation, growth, and departure analysis

There were two analysis done on the bubble dynamics, the first was to analyze the growth characteristics of the bubble and the way the contact area changed during the growth phases. The data analyzed were captured at five distinct instances in the growth of a bubble. Instance 1, nucleation of a new bubble, was captured immediately after a prior bubble departed and a new bubble could visibly be seen forming. Instance 2 was captured the first moment the new bubble maintained a stable shape and the contact diameter could be measured. Instance 3 was captured as the largest contact diameter the bubble presented, before the contact diameter started to recede. Instance 4 was captured during recession of the contact diameter when the bubble was not actively departing. Instance 5 was captured immediately prior to the moment the bubble fully departed from the surface. As the bubble leaves the surface, there is a wave that ripples through the surface area of the bubble, instance 5 was captured just before this wave. This analysis was performed at five different bubbles to ensure consistency amongst them, the analysis displayed was representative of all bubbles analyzed.

The second analysis was performed to measure the departure time of bubbles from the surface. The data displayed was performed by recording elapsed time from the moment a bubble visibly nucleates to the moment it detaches from the surface. Seven different bubbles were analyzed for elapsed time to capture an average time from nucleation to departure.

Volume calculation

In all of the data presented analyzing the bubbles using high speed imaging, the bubble volume was reported. This analysis in approximated using the data captured from ImageJ using a solid of revolution “disc method”, an approximation for the integral revolution. First, the image brightness, contrast, and color threshold were adjusted to provide a clear boundary along the perimeter of the bubble (barrier between vapor and liquid). The data was then exported as an image file which listed each pixel value in a comma separated value matrix. In this file, the white background of the liquid was displayed as a value of 255 and the black of the bubble was displayed as a value of 0. The values corresponding to the bubble could then be located. Using the scale bar, the approximate length per pixel could be measured, typically around 110 pixels per millimeter. Using the number of pixels per row of pixels for the bubble, the radius could be determined and a volume for that layer of the disc calculated. Then summing the volume of each of these discs for the entire volume provides an estimation for the total volume of the bubble.

3.4 Results

Based on the design analysis, it was determined that the 40% Si-DLC sample presented the best opportunity for enhanced boiling heat transfer performance as it had a contact angle in the “balanced” range identified and had the lowest hysteresis. For these reasons, the results shown below were performed using the 40% Si-DLC sample.

3.4.1 Heat Transfer Results

The results of the following data were first predicated on the useability of the surfaces. Any surface that improves boiling heat transfer performance but is not stable at high temperatures has far less utility for industrial applications. Therefore, the high temperature stability was tested first. To verify the high temperature stability of the 40% Si-DLC, the sample was subjected to thermal stresses and compared to a perfluoropolyether based silane that displayed exceptional properties for condensation heat transfer. **Figure 3.12** shows that after just 1 hour at 400°C, the silane coating was completely degraded and the surface fully wetting. This is a stark contrast to the 40% Si-DLC which was subjected to 12 hours at 400°C, 50 hours at 700°C, and 5 boiling cycles to the critical heat flux, and displayed negligible change to the dynamic contact angles after these stresses.

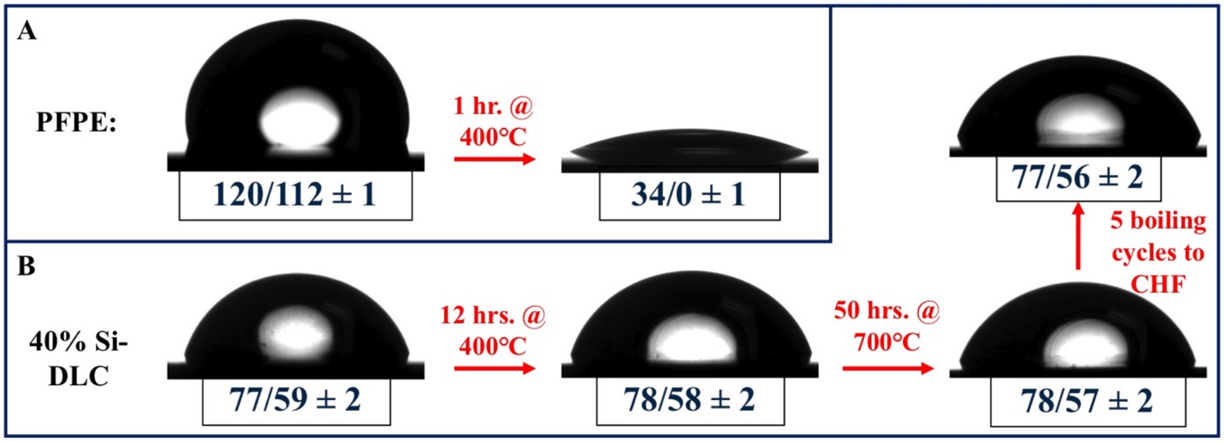

Figure 3.12: Contact angle evolution of surfaces subjected to high heat with a droplet image and corresponding dynamic contact angles shown. **A)** A perfluoropolyether based silane degraded from fully hydrophobic to fully wetting after just 1 hour at 400°C. **B)** The 40% Si-DLC sample showed negligible changed in contact angles after 50 hours at 700°C and multiple boiling cycles.

More importantly, the 40% Si-DLC displayed clear improvements in both HTC and CHF compared to an uncoated surface. **Figure 3.13** shows the heat curve for the 40% Si-DLC and a bare Si sample that would be representative of the high surface energy copper surfaces typically used as boiling surfaces currently. The 40% Si-DLC enhanced both HTC and CHF by more than 40% over the bare Si and maintained these improvements even after annealing at 700°C. This coated sample also surpassed the CHF of nearly all other smooth surfaces previously studied, except for one study on titania (TiO_2), though the titania had to be activated by ultraviolet light and last only a few minutes before the contact angles returned to those akin to bare Si.

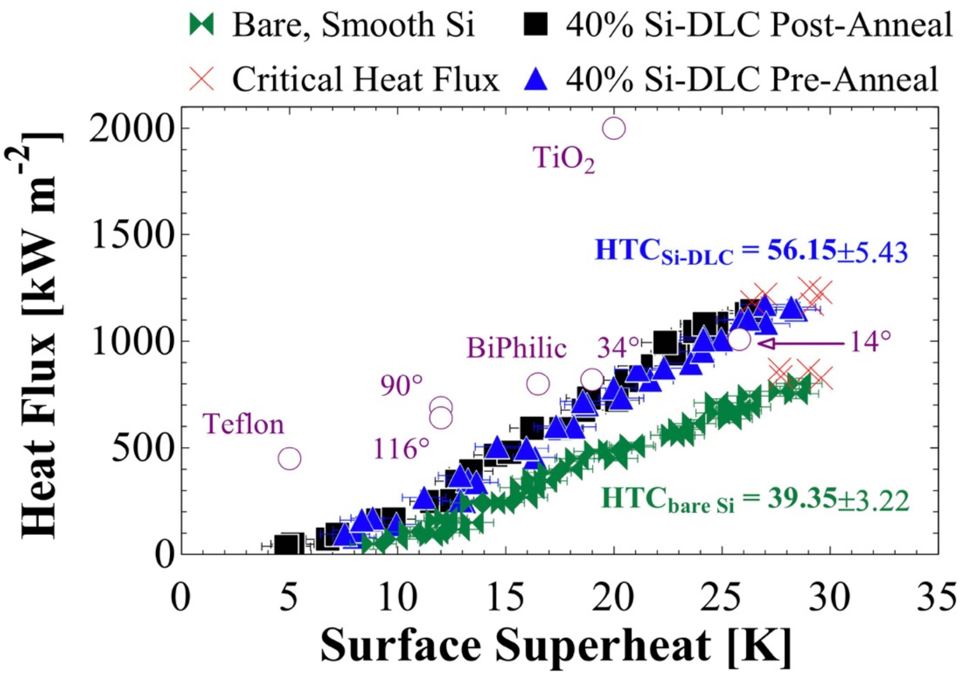

Figure 3.13: Heat curve measured for bare Si (hydrophilic) substrate, 40% Si-DLC before annealing at 700°C, and 40% Si-DLC after annealing at 700°C. The 40% Si-DLC exhibited an HTC 43% higher and a CHF 42% higher than bare Si, and it maintained its performance after the 700°C anneal. This plot has been overlayed with various other studies on smooth surfaces including a biphilic[105], Teflon[216], titania (TiO_2)[242], and surfaces with contact angles of 18°, 34°, 90°,[243] and 116°[215].

This is an important progression for boiling surfaces as this 40% Si-DLC displays three key characteristics for widespread application: high heat stability, long term stability, and simultaneous improvement of HTC and CHF. Furthermore, this surface displays the highest CHF of any smooth, stable surface that has been previously published.

3.4.2 Bubble Growth and Departure Dynamics

The key to understanding why this surface can simultaneously increase both HTC and CHF comes in understanding the bubble dynamics on the surface. The cycle of a bubble from nucleation, growth, to departure was captured and is shown in using high speed imaging, and has been divided into five characteristic phases:

1. Nucleation- this is the point that a bubble is first visible on the surface

2. Initial Bubble- the time at which a bubble is formed and stable on the surface, this is the first point the dimensions of a bubble can be reliably measured
3. Bubble Growth- growth phase of the bubble where the contact are is increasing and the contact line is receding in the liquid
4. Bubble Recession- the bubble is continuing to grow, but the buoyancy forces are now dominating. The contact area is shrinking, and the contact line is advancing in the liquid.
5. Bubble Departure- bubble departs from the surface

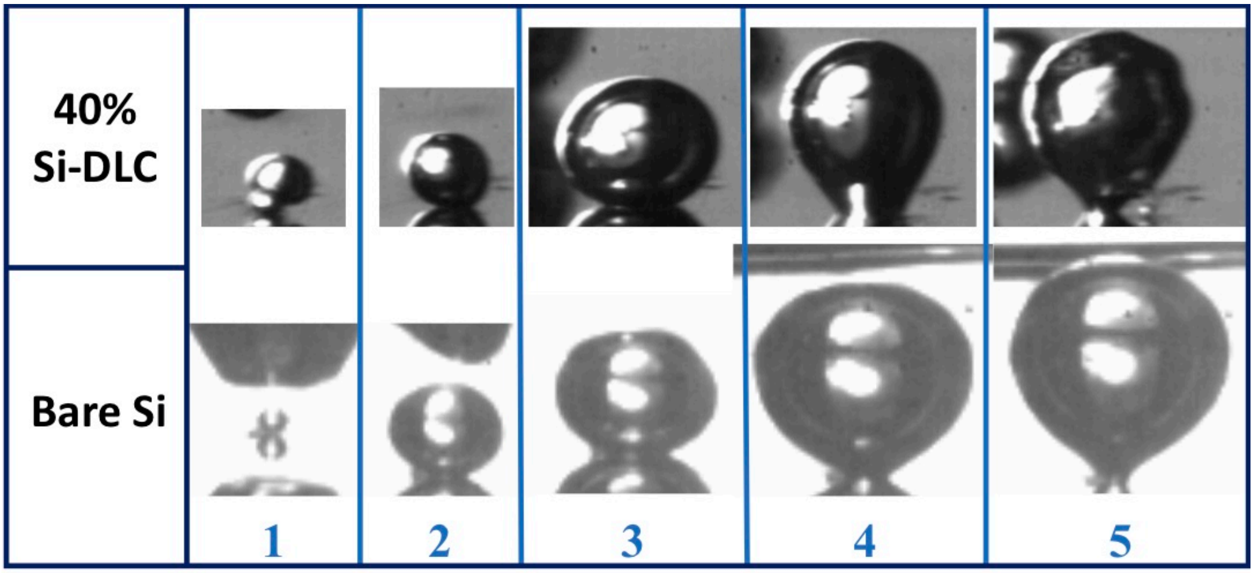

Figure 3.14: Progression of bubble growth from nucleation to departure for a bubble on 40% Si-DLC surface (top) and bare Si (bottom). The cycle can be divided into 5 phases which are described above.

Further analysis of these phases was performed to measure the elapsed time, contact diameter, and bubble volume during each of these phases. The parameters were measured for five bubbles on each surface, with the resulting data is shown in **Table 3.3**. There is a clear trend in the data that the contact diameter of the 40% Si-DLC grows and then contracts during the growth of the bubble. This is a stark comparison to the bare Si, which had a near constant diameter throughout the bubble cycle, caused by the pinning of the liquid at the 3-phase contact line.

		40% Si-DLC			Bare Si		
Instance	Growth Stage	Elapsed Time (ms)	Contact Diameter (mm)	Bubble Volume (mm^3)	Elapsed Time (ms)	Contact Diameter (mm)	Bubble Volume (mm^3)
1	Nucleation	0	Nucleation		0	Nucleation	
2	Initial Bubble	3.2	0.46	0.71	6.4	0.46	1.00
3	Growth	6.7	1.28	3.21	13.4	0.51	3.66
4	Recession	9.7	0.73	4.81	19.6	0.50	7.14
5	Departure	11.6	0.39	5.13	22.1	0.34	7.94

Table 3.3: Data collected for each of the bubble cycle phases for 40% Si-DLC and bare Si. The nucleation, growth, and departure of individual bubbles was captured at low heat flux using high speed imaging. The imaging was then analyzed to calculate the elapsed time, contact diameter, and bubble volume at each of the five instances identified in **Figure 3.14** This data was collected for 5 individual bubbles on each surface with the averages shown.

A further analysis was performed by only examining the departure time and volume with the data shown in **Table 3.4**. This shows a similar trend in which the bubbles on the 40% Si-DLC departed the surface 40% faster and departed with 30% less volume than on the bare Si.

Table 3.4: Boiling at a very low heat flux was used to isolate individual bubbles and measure the growth time and departure volume from the two surface of interest, bare Si and 40% Si-DLC. Seven different instances of a bubble nucleating, growing, and departing the surface were captured and analyzed for departure time and volume at departure. The departure volume was calculated from the projected cross-sectional area.

Bare Si		40% Si-DLC	
Time to Depart (ms)	Volume at Departure (mm^3)	Time to Depart (ms)	Volume at Departure (mm^3)

	21.3	8.34	11.6	5.13
	22.1	7.94	10.9	4.96
	24.6	9.15	14.5	6.35
	18.7	7.13	12.8	5.87
	19.6	7.68	11.3	5.39
	22.9	8.36	13.4	6.03
	26.1	9.27	12.9	5.88
Average	22.2 ± 2.61	8.27 ± 0.77	12.48 ± 1.28	5.66 ± 0.51

From the above data, it is clear why the 40% Si-DLC enhances both HTC and CHF. With faster growth of bubbles, the heat transfer coefficient is enhanced because the liquid can be vaporized in a shorter period of time. The rapid departure time reduces the residence time of bubbles on the surface and inhibits the coalesces of bubbles. This leads to the increase in CHF seen in the data as the surface is covered by less vapor. An analysis of each of these phases showed that the 40% Si-DLC allows the bubbles to grow more rapidly, depart from the surface in a shorter length of time, and the volume at departure was lower. This combination of rapid growth, facilitated by the receding contact angle, and the rapid departure, facilitated by the advancing contact angle, lead to the simultaneous enhancement of both HTC and CHF of the 40% Si-DLC surface.

3.4.3 Abrasion Resistance

In addition to the enhanced heat transfer performance and high temperature stability displayed by the 40% Si-DLC sample, it also demonstrated exceptional mechanical durability. A comparison was again made against two silane coatings, a crystalline and fluorinated monolayer and an amorphous PDMS based silane. The two silanes degraded rapidly under the harsh abrasion and were completely wetting after just a few tens of cycles. By 100 cycles, both were nearly completely wetting. Compare this to the 40% Si-DLC which saw nearly no change in the dynamic contact angles after 2000 abrasion cycles, and even after 10,000 cycles still presented a receding contact angle greater than 30°. When considering a coating for industrial use, it must be able to withstand significant abuse and maintain its performance. The 40% Si-DLC displays the exceptional durability necessary for widespread use.

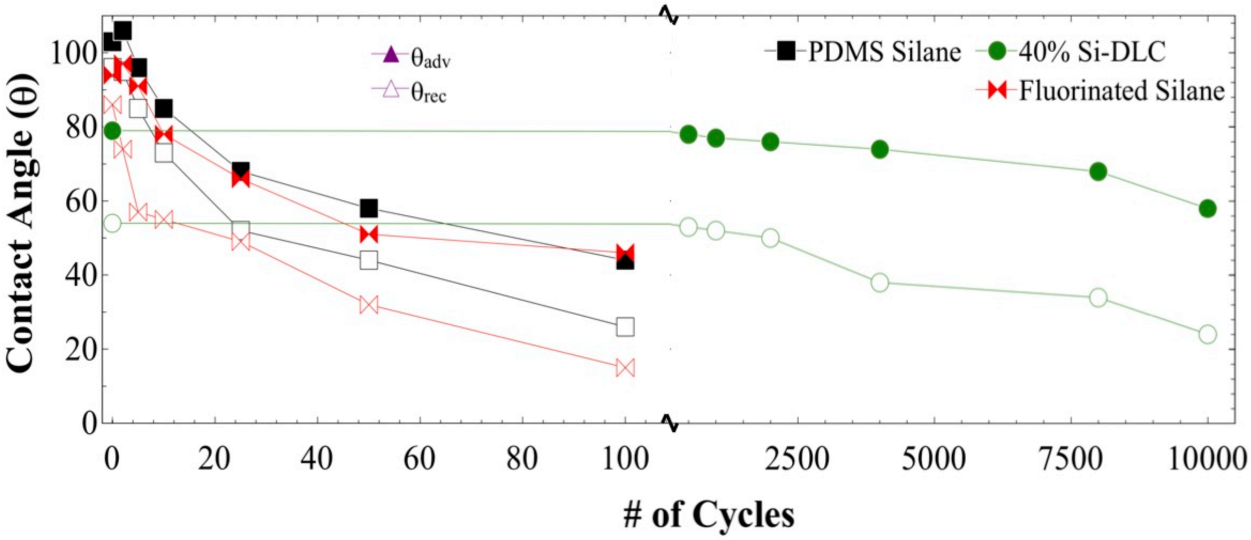

Figure 3.15: Plot comparing the wettability of surfaces to the number of abrasion cycles by aluminum oxide particles in a rubber matrix. Traditional surface modifiers degraded in a matter of a few cycles whereas the 40% Si-DLC maintained wettability properties for thousands of cycles.

3.5 Conclusion

In this chapter, we have explored the development of a novel, high temperature stable, boiling surface that can simultaneously enhance both the heat transfer coefficient and critical heat flux for boiling heat transfer. This surface was deposited from a silicon and carbon target using pulsed laser deposition to create a silicon doped diamond-like carbon surface. The resulting surface exhibited very high temperature stability with no noticeable degradation after 50 hours at 700°C, and exceptional mechanical durability under harsh abrasion by aluminum oxide particles. There is no previously published surface that exhibits the stability shown on the 40% Si-DLC surface while also maintaining increased boiling heat transfer. The mechanism believed to allow for this enhancement is a unique combination of a mildly hydrophilic surface, low hysteresis, and high durability. The moderate contact angle assists in the rapid growth of bubbles on the surface that cause them to spread slightly on the surface which enhances the vaporization rate into the bubble. The low hysteresis then allows the 3-phase contact line between the bubble and surface, to rapidly recede allowing the bubble to depart quickly and with a low volume. These surfaces and design parameters will usher in a new material that can be used to significantly improve boiler efficiencies in a variety of industrial applications, with significant utility in steam-based power generation.

Chapter 4

Ice prevention using bound water to inhibit crystal formation

This chapter is primarily adapted from an article submitted to *Science Advances* which was equally co-authored by Brian Macdonald and Abhishek Dhyani. Data collection and characterization was performed in part by Jiayue Huang.

4.1 Introduction

Ice and frost accretion is a serious problem affecting a wide range of industries which include but are not limited to: aircraft, ships, refrigerators, and heat exchangers.[115,244–246] Frost on climate controlling heat exchangers result in a decrease of heat transfer efficiency by up to 75%.[247,248] To combat this, recent efforts have sought various methods to suppress ice formation rather than facile removal of bulk ice. However, the performance of recent frost prevention innovations remained limited and are difficult to utilize in real world applications.

Ice formation and nucleation is relatively simple process and becomes more complex when involving a surface. In homogeneous nucleation processes, supercooled water molecules will achieve hydrogen bonding for successively longer durations until a compact nucleus is formed. Once the ice nucleus reaches a point termed the critical radius, spontaneous crystallization occurs within the entire system.[114] In most industrial, transportation, and residential sectors, homogeneous nucleation does not occur. Heterogeneous ice nucleation occurs when water freezes upon a surface at the solid/liquid interface. The presence of a solid/liquid interface reduces the energy barrier of ice nucleation, facilitating freezing to occur notably easier than in the homogeneous form.[249] Therefore, surface design strategies which increase the thermodynamic barrier of ice nucleation to, or in some cases beyond that homogeneous ice nucleation, are necessary to prevent the icing of surfaces.

Initial surface design efforts included the reduction of surface energy and tuning of surface roughness and geometric structures. It was found that for a perfectly flat substrate, the free energy barrier of ice nucleation is reduced by a geometric factor compared with the free energy barrier of homogeneous nucleation. This geometric factor scales with increasing water contact angle to limit of perfect non wettability (ie 180º), whereby the homogeneous nucleation state is reached.[114] Generally, the more nonwetting a substrate is, the lower the ice nucleation temperature. However, perfectly flat substrates are unrealistic, and surface features will facilitate nucleation. Although surface geometry and roughness tend to aid in ice nucleation, achieving sufficiently small features can reduce the ice nucleation temperature.[250,251] Once features reach the size of the critical nucleation radius, the process reverts to that of homogeneous nucleation. Superhydrophobic surfaces displayed an icing delay with liquid water, but this can be attributed to the reduced heat transfer across the composite interface in a cassie-baxter state.[77,252] Lubricant infused surfaces (LIS) have also been show to resist icing by allowing water and ice droplets to easily slide off the surface on the lubricant layer.[253] Both of these hydrophobic surfaces rely on shedding water or ice (applicable to freezing rain) rather than inhibiting frost growth from humid air and suffer from deteriorating performance during icing/deicing cycles due to surface damage or lubricant depletion.[10,116,254]

Recent advances have been made utilizing molecules that suppress ice crystals by either preventing formation or preventing growth. Anti-freeze proteins have been of particular interest since the discovery of the mechanism in plants and fish to survive subzero temperatures.[119,255,256] These helical proteins bind to the crystal planes of ice and inhibit growth of the crystal.[120,121,257,258] Proteins are susceptible to depletion, similar to the lubricated surfaces, as the surface goes through multiple ice/deice cycles, and experience a decrease in performance when surface confined, due to the necessity of the protein to bind to the crystal face.[259] Polyelectrolyte brushes with a substituted counterion have shown to significantly inhibit ice formation. The counterion in the hydrogel is used to suppress the ice nucleation temperature and delay ice crystallization.[260] The useability of these brush surfaces is limited by the complex process to create them, and the inability to scale the thickness to further enhance anti-icing properties.[123,261]

We have developed a simple, 1-step coating that can easily be applied to surfaces, inhibits ice formation for longer than 4,000 seconds, and maintains its performance through multiple ice/deice cycles. Poly-zwitterionics contain both a cation and anion, similar to a counterion coating, but the ions are bound together on a monomer chain. The ionic monomer assists in strong hydrogen bonding with water molecules that condense on the surface, which have been shown to be non-freezing when strongly bound.[262,263] Meanwhile the bound ions prevent any ionic depletion when the ice melts and water runs off the surface.

4.2 Design Criteria for Anti-Icing Surfaces

4.2.1 Hydrophilicity and implications for non-freezable water

There are two effects of the contact angle on heterogeneous icing on a surface. The first, similar to condensation and boiling, is the influence of contact angle on the Gibbs free energy. Just as with condensation, as the contact angle of a surface decreases, frost formation on the surface is more energetically favored.[264] Also, as a surface becomes smoother and the roughness (R/r_c) is reduced, then heterogeneous nucleation becomes less energetically favored, both shown in **Figure 4.1**.[114]

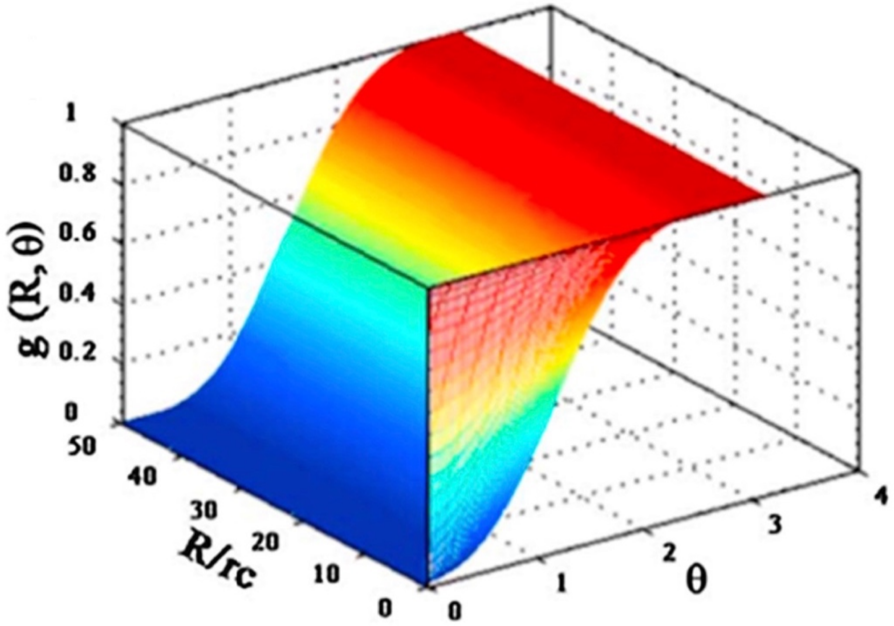

Figure 4.1: Three-dimensional graph comparing the contact angle (θ), surface roughness (R/r_c), and the free energy barrier for heterogeneous nucleation (g). As a surface becomes smoother or more hydrophilic, then heterogeneous ice nucleation is more energetically favored. Figure adapted from article in *Progress in Materials Science*.[114]

This correlation between contact angle and heterogeneous ice nucleation (HIN) would seem to imply that a hydrophilic surface would be unfavorable for anti-icing. Thus, we get to the second effect of contact angle, the binding of water. Hydrophilic polymers have been shown to bind water to the polymer in various states: free water, freezable bound water, and non-freezable bound water.[265,266] The free water acts as one would expect and freezes at approximately the freezing point (0°C) at atmospheric pressure. The freezable, bound water exhibits a slightly depressed freezing point, typically about 2-3°C, but is still freezable once the temperature drops sufficiently. The state of most interest in this study is the non-freezable, bound water. This is water that is tightly bound to the polymer and will never freeze. More importantly, the ability for a polymer to bind water in this non-freezable state is directly correlated to the hydrophilicity of the polymer.[267] In the case of anti-icing, if a coating can absorb enough water in the non-freezable, bound state, then this becomes the dominant mechanism for anti-icing, and the inhibition of icing can be greater than that induced by the surface energy alone.

4.2.2 Crosslinking polymer network

Based on the above analysis, a very hydrophilic polymer network should produce a surface with maximum ice inhibition. Prior studies have shown this by grafting thin layers of polyelectrolyte brushes and exchanging the ions to increase the hydrophilicity of the surface.[268] By tuning the ion used, the ice nucleation temperature can be suppressed and bound water increased, this is due to the higher polar bonding between the water and ions.[269,270] A similar effect can be achieved with zwitterionics though, in which the ions are not separated but actually contained along the same monomer chain.[271] These zwitterionics can be crosslinked into a network and exhibit superhydrophilicity with good water binding properties.[272] A network of poly-zwitterionics presents additional ease in production as the ions do not require exchange as is needed in the counterion hydrogels. Therefore, a polymer network consisting of a poly-zwitterionic would produce a viable anti-icing coating by strongly binding water in a non-freezable state within the superhydrophilic network.

4.3 Materials and Methods

All samples were created as 3 cm x 3 cm squares. The measured area was 2 cm x 2 cm, with the overhang allowing for proper clamping to the copper cooling post. Adhesive foam was placed along the 2 cm x 2 cm perimeter of the contact area to isolate the sample area outside of the cooled surface area.

4.3.1 SBMA

The zwitterionic selected for the polymer network was a [2-(Methacryloyloxy)ethyl]dimethyl-(3-sulfopropyl)ammonium hydroxide (SBMA). This zwitterion contains both the polar groups necessary for strong water bonding and the functional groups for crosslinking, as shown in **Figure 4.2**. SBMA has repeatedly been shown to be able to form superhydrophilic networks with strong interactions with water which is necessary to bind water in a non-freezable state.[273–275]

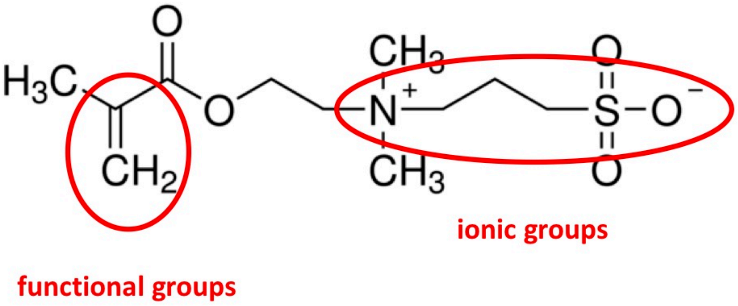

Figure 4.2: Molecular structure of [2-(Methacryloyloxy)ethyl]dimethyl-(3-sulfopropyl)ammonium hydroxide (SBMA). The molecule contains both functional groups for crosslinking into a polymer network and ionic groups for strong binding to water in a non-freezable state.

4.3.2 Hydrogel Casting

Anti-ice SBMA coatings were generated by: oxidizing the surface of aluminum substrates, reacting the silane linker to the oxidized aluminum, dissolving reagents in water, and casting the solution onto the activated aluminum. The casted samples were then heated to polymerize the SBMA network and bond to the aluminum.

Functionalized Aluminum

M-D building products 0.019-inch aluminum was cut to 32x32mm squares. The aluminum squares were cleaned with isopropyl alcohol (IPA), wiped dry with a kim wipe, and rinsed with more IPA. The samples were then blown dry with air. The dry samples were then placed clean side up within water on a hotplate turned to 150C. Once the aluminum samples chaned from grey metallic in color to a brass color, sufficient oxidation existed for the linker reaction. 3-(Trimethoxysilyl)propyl methacrylate (TMSPMA) purchased from Sigma Aldrich CAS# 2530-85-0 , was chosen as the linker between the oxidized aluminum and bulk coating. 50 µL of TMSPMA was mixed with 10ml of anhydrous ethanol and 400µL of 1:10 (v/v) acetic acid/water solution (silanization catalyst). After sufficient mixing, 350 µL of the linker solution was dispensed onto the oxidized aluminum squares and allowed to react for 25 minutes. Once complete, unbound silane was rinsed off with IPA and dried with compressed air.

SBMA Solution

1 gram of [2-(Methacryloyloxy)ethyl]dimethyl-(3-sulfopropyl)ammonium hydroxide (SBMA), purchased from Sigma Aldrich CAS# 3637-26-1 was mixed into a 20ml glass scintillation vial containing 2ml of deionized water. A 40mg/ml solution of thermoinitiator potassium persulfate (KPS) CAS# 7727-21-1 purchased from Sigma Aldrich, and deionized water was separately generated. 75 µL was added to the SBMA solution. Bifunctional crosslinkers N,N′-Methylenebis(acrylamide) (MBA), CAS# 110-26-9 and polyethylene glycol diacrylate (PEGDA) CAS# 26570-48-9, Mn: 250 both purchased from Sigma Aldrich were added to the SBMA solution in desired proportions. For low concentrations of 0.5% and 0.25%

crosslinker, 20mg/ml (crosslinkers/water) were developed and added to the SBMA solutions. The aggregate solution sonicated for 10minutes and gyrated for 20 minutes to fully solubilize all reagents.

Anti-Ice SBMA Network Coated Aluminum

The solubilized SBMA solution containing thermoinitiator KPS and crosslinker were dispensed onto the functionalized aluminum in the necessary amount to achieve 100 µm, 150 µm, and 200 µm thick coatings. The solutions were spread across the entire area of the functionalized aluminum with a rubber squeegee upon a glass stir rod. Once fully applied, the aluminum with SBMA solution was placed on top of a hotplate set to 80ºC and covered with a glass Corning petri dish with a 53mm diameter and 15mm height. The samples were allowed to cure for 20 minutes. Unflushed samples were tested without further modification. Flushed samples were created by submerging cured SBMA coated aluminum within water and stirring for 1hr to remove free, uncross-linked SBMA.

4.3.3 Alternate Surface Fabrication

The bare aluminum surface was cut from 6061 T6 Aluminum alloy (McMaster-Carr), and was sonicated in Acetone, IPA, and water before testing.

The slippery lubricant infused porous surfaces (SLIPs) was manufactured from an aluminum substrate (6061 T6 Aluminum Alloy, McMaster-Carr) which was first etched in 2.5 molar hydrochloric acid (Fischer Scientific) for 20 minutes to create nano-structure. It was then agitated in a bath sonicator for 10 minutes to remove loose aluminum particles and placed in boiling water to convert the outer layer to boehmite nano-crystals (γ-AlO(OH)). The textured aluminum was reacted with a vapor of (heptadecafluoro-1,1,2,2-tetrahydrodecyl)triethoxysilane (Gelest) in a vacuum oven at 100°C and ~5 mTorr for 24 hours. After rinsing with Vertrel XF, Toluene, and IPA, Krytox GPL-100 perfluoropolyether oil (Miller-Stephenson Chemical Company) was drop cast onto the surface, and the sample inverted for 12 hours to allow excess oil to be removed.

4.3.4 Contact Angle Measurement

Contact angles were measured with a Ramé-Hart 200 F1 goniometer. A droplet of 2.5 µL of water was dispensed on the coating. Measurements were taken on 3 different spots across the coating at 10 seconds, 1minute, and 5 minutes in order to assess wettability and absorption properties.

4.4 Data Collection

4.4.1 Chamber Configuration

The same environmental chamber that was used for condensation (described in section 2.4) was used for icing tests, with some minor modifications shown in **Figure 4.3**. Experiments were no longer conducted under vacuum, and the humidity and temperature were closely monitored with a ¼ second refresh time. The humidity of the chamber was controlled by flowing dry air through a box with water in it, then into the chamber. By varying the flow rate of the dry air, the residence time in the water box was varied, and the humidity varied inversely of the flow rate. To prevent pressurization in the chamber, a second valve at the base of the chamber was opened to allow for exhaust air to exit the chamber. Using this configuration, the humidity in the chamber could be controlled to ±1% relative humidity (RH).

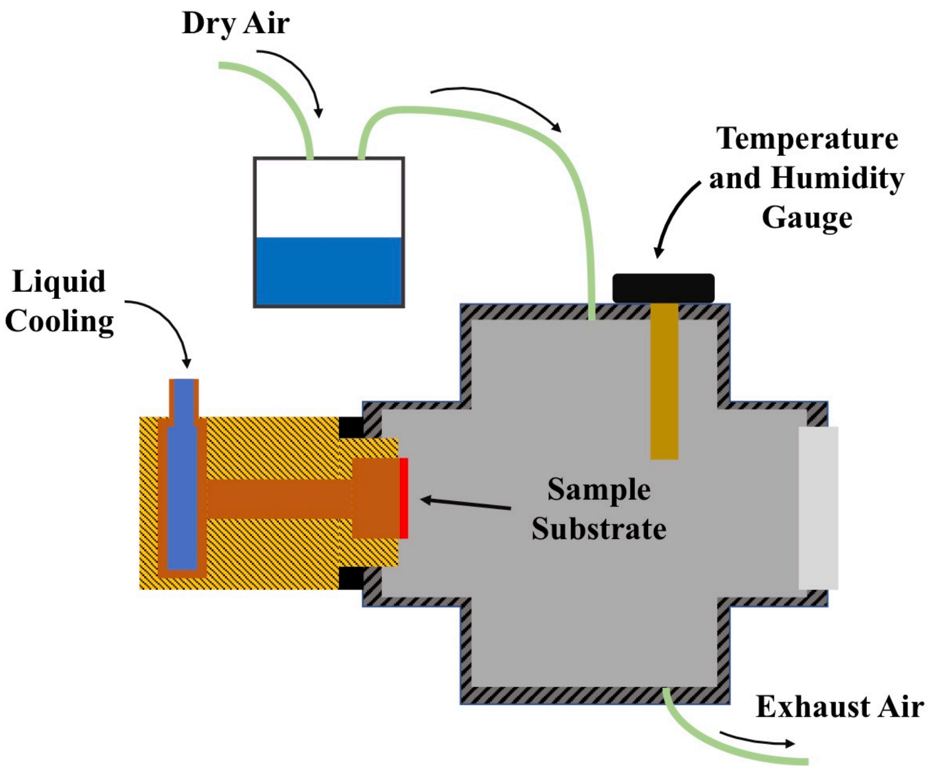

Figure 4.3: Schematic of the testing chamber that icing tests were performed in. The same environmental chamber, as was used for condensation experiments (section 2.4), was used for icing with some minor modifications. The humidity of the chamber was controlled by flowing dry air through a box containing water to humidify the air before entering the chamber. The same liquid cooling channels were used with a sample adhered to the copper using silver paste.

The air temperature in the chamber was not controlled and left at ambient temperature and pressure (~20 ± 0.5°C). Samples were tested at ambient temperatures to accelerate the icing tests and allow for more rapid data collection. We attempted tests at reduced air temperatures but found that the icing times for samples were unreasonably long. Since the absolute humidity reduces significantly with the air temperature, even at 100% RH and an air temperature of 5°C, there is less water in the air than at 20°C and 45% RH.[276] When one of the experimental samples was tested at 5°C and 75% RH, the surface did not ice after 48 hours, therefore it was unrealistic to test in these conditions. The higher air temperature and absolute humidity means that water condenses on the surface more rapidly leading to quicker icing.

Lastly, the same liquid cooling channels that were used for condensation were used for icing as well. Since the heat flux across the surface is so low, there is a negligible temperature drop between the sample and the liquid cooling channels, therefore the surface temperature is approximately the same as the recirculating liquid temperature. The samples were mounted to the copper with silver paste and then pressed together with Teflon frame that surrounded the perimeter of the sample. Silver paste was used instead of solder since the system would be operating at such a low heat flux. Given the low heat flux, the interfacial resistance is not as critical and silver paste allowed for rapid sample changes. The copper was still surrounded by a Teflon jacket to prevent any lateral heat transfer ensuring the surface temperature was nearly equivalent to the liquid temperature. This created a sandwich structure, as shown in **Figure 4.4**, in which the screws fastened together the substrate to the copper, the Teflon frame distributed the force evenly around the substrate, and the insulating foam between the sample and Teflon isolated the experimental area that was cooled. The completed assembly can be seen in **Figure 4.6**.

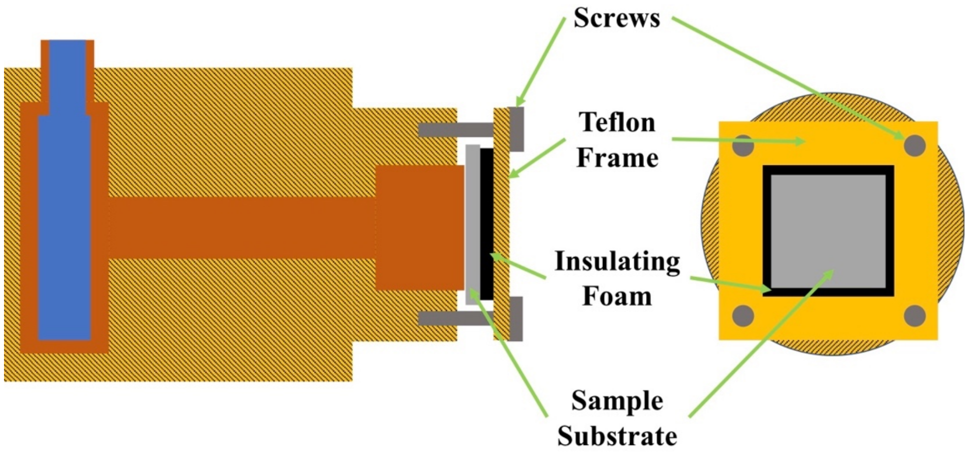

Figure 4.4: Schematic of the assembly adhering the sample substrate to the copper cooping post. Four screws fastened a Teflon frame around the perimeter of the sample. The Teflon frame pressed together the insulating foam and substrate to the copper cooling post. Schematic not drawn to scale.

4.4.2 Icing Time Collection

Surface icing times were determined visually by the sudden opacity change of the surface. Video of the surface was recorded from the moment liquid recirculation commenced and continued until the surface was completely iced. After the surface was iced, the video was accelerated 200x and the ice initiation time was determined to be the instance that icing commences. Since the propagation of ice across the surface varied by sample, it was determined that the formation of the first crystal was the best indicator of ice inhibition.

4.4.3 Cyclic Testing

Cyclic testing was performed to be representative of the cycles a condenser coil would be subjected to in an industrial freezer. A typical condenser coil would go through a series of on and off cycles before being heated to melt any ice formation. A single cycle consists of 8 “on” periods, each follow by an “off” period with the period following the final “on” period being the heating. With each period lasting for 20 minutes, therefore a full cycle of on/off cycles lasts 5 hours followed by the 20 minutes heating period. To simulate this cycle, during the “on” periods, the liquid cooling was set to -20°C and during the “off” periods, the liquid cooling was set to 0°C. The off cycle was set to 0°C instead of completely off since the air temperature was significantly higher than what would be experienced by the coil in the freezer. This ensured the surface experienced comparable conditions to those of a freezer and the results would be representative of the anti-icing performance in a real freezer. During the simulated heat period, the surface was heated to 20°C to allow any ice to melt. A depiction of 2 simulated cycles and corresponding surface temperature set points are shown in **Figure 4.5**.

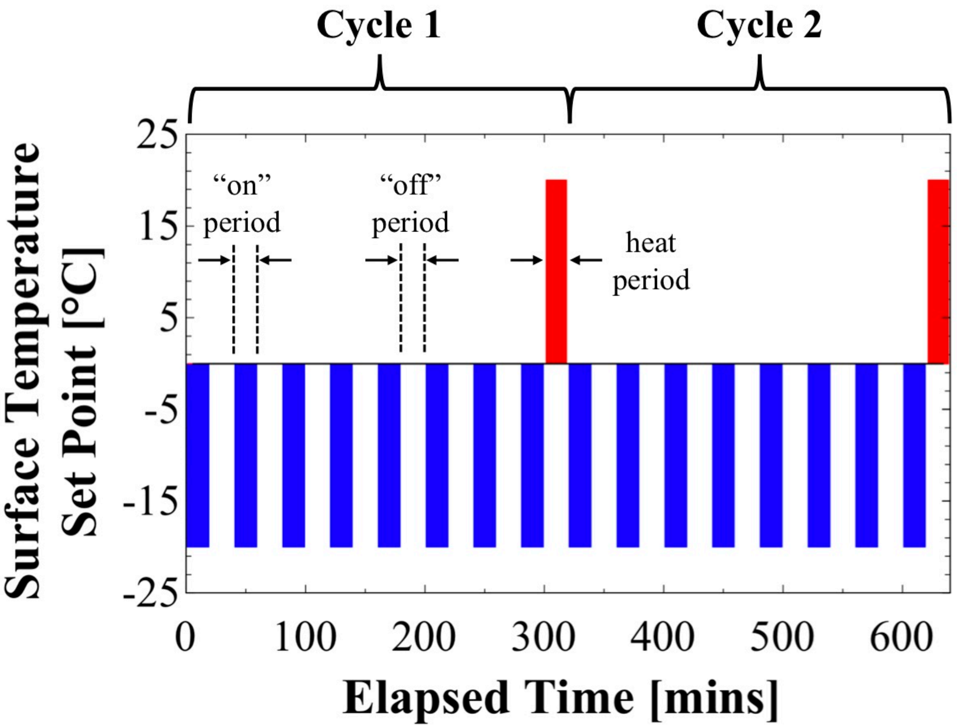

Figure 4.5: Depiction of the thermal periods for cyclic ice testing to simulate the thermal cycles of a commercial condenser coil in a freezer. A single cycle consists of 8 "on" periods (surface temperature of -20°C), each followed by an "off" period (0°C), with the final period as a heat period that thaws the ice. Each period lasts 20 minutes, making one full cycle 5 hours and 20 minutes long.

4.4.4 Droplet Freezing Time

One commonly used method to quantify the anti-icing capabilities of a surface is to measure the heterogeneous ice nucleation (HIN).[116,122,123,123,277–281] To perform a comparable experiment, observed the freezing time of a droplet on the sample surface and recorded the elapsed time to freeze the droplet. The same assembly described in **Figure 4.4** was placed on a flat surface such that the sample was level. A 20 μl droplet was placed in the middle of the sample as shown in **Figure 4.6**. Simultaneously, cooling liquid began flowing through the cooling channels to reduce the surface temperature to -20°C and a camera placed directly above the sample began imaging at 15 second intervals. Using a polarizing film on the camera lens, the freezing time could be determined by a sudden change in opacity of the droplet between subsequent pictures. The first picture with a noticeable opacity change was determined to be the freezing time as this would be accurate to within 15 seconds.

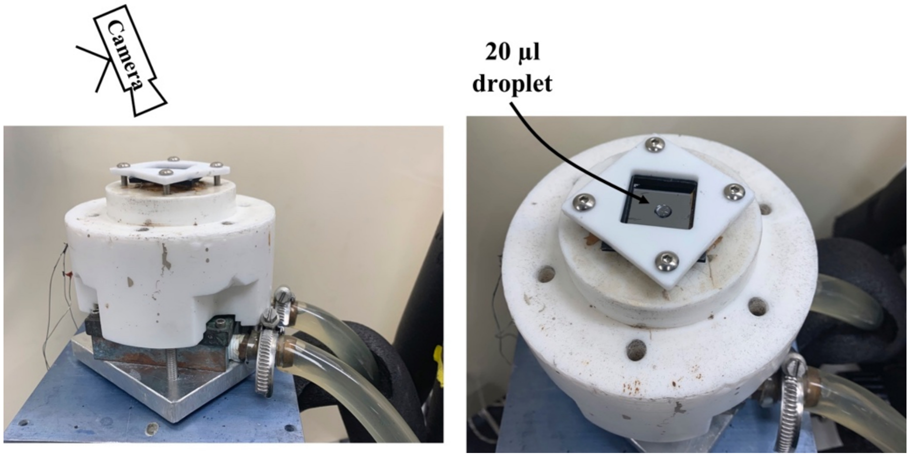

Figure 4.6: Image of the experimental set-up used to measure droplet freezing time. The same sample assembly described in **Figure 4.4** was placed on a flat surface and a 20 µl droplet was placed in the middle of the sample (right). A camera was placed directly above the sample to image the droplet at 15 second intervals (left).

4.5 Results

4.5.1 Effect and Selection of Crosslinker

There are two viable crosslinkers, PEGDA and MBA, that have been shown to be suited with SBMA that we examined further, both are shown in **Figure 4.7**.[282,283] A short chain version of the PEGDA was chosen such that the molecular weights, and therefore the reactive sites per gram, were approximately the same for each crosslinker.

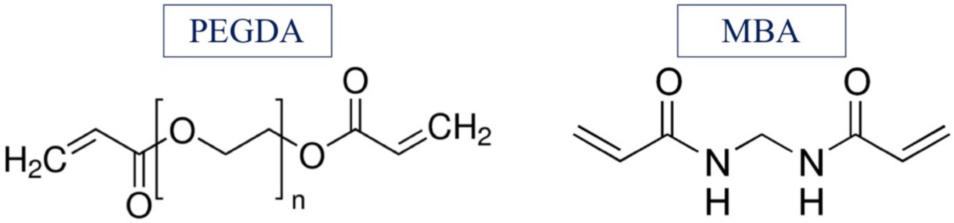

Figure 4.7: The two cross linkers examined for this study were poly(ethylene glycol) diacrylate (PEGDA, left) and N,N′-Methylenebis(acrylamide) (MBA, right).

Next, a series of coatings were created with these two crosslinkers, all with 1% of the respective crosslinker in them, and the icing times were compared. Some samples were flushed, in that they were soaked in water after the reaction to extract any free, unreacted SBMA, whereas other samples were unflushed in that the excess SBMA remained within the network. **Figure 4.8** shows the results of these icing tests, and the PEGDA crosslinked coatings inhibited icing for significantly longer than the MBA crosslinked coatings. In the flushed network, without the excess SBMA, the PEGDA crosslinked coating delayed the onset of icing by nearly 20% longer.

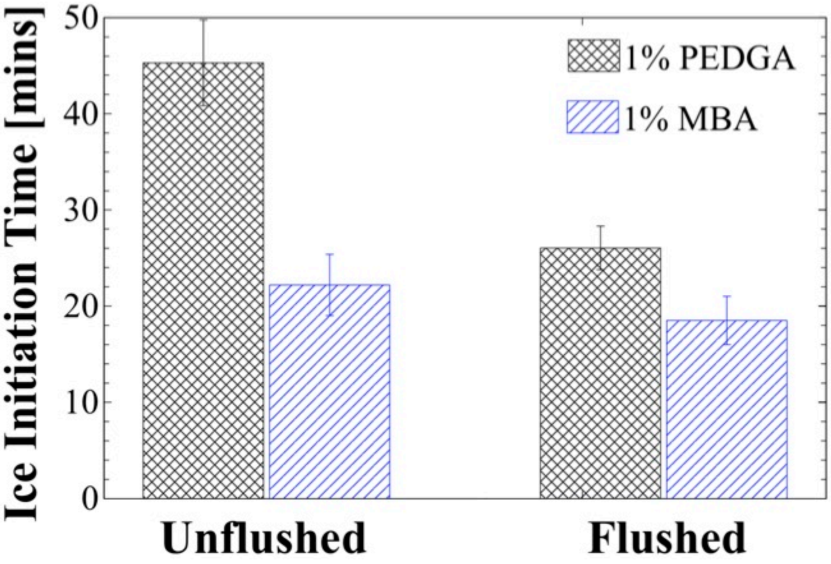

Figure 4.8: Icing time results comparing the effectiveness of the two crosslinker options, PEGDA and MBA. Regardless of the inclusion of the excess SBMA (flushed vs. unflushed network), the PEGDA crosslinked coatings performed significantly better.

This can be explained by comparing the wetting behavior of water on networks crosslinked with the PEGDA and MBA, shown in

Table 4.1. The PEGDA crosslinked networks consistently displayed a contact angle about 20° lower than that of the equivalently crosslinked MBA networks, and the equilibrium contact angle was always more hydrophilic. Referring back to section 4.2.1, it is clear why the more hydrophilic network (PEGDA crosslinked) can delay icing for a longer period of time as it can bind more water in a non-freezable state. Therefore, the PEGDA networks, for identical network volumes, can absorb a greater amount of water into it before the free and freezable bound water become dominant and induce icing.

Table 4.1: Contact angles for SBMA networks crosslinked with varying amounts of PEGDA and MBA. The droplets on the PEGDA crosslinked networks consistently displayed a more hydrophilic contact angle compared to MBA. Since the network is a hydrophilic hydrogel, it partially absorbs water, and the contact angle evolves with time. Contact angles were recorded immediately after contact with the surface (10 sec.), 1 minute after, and 5 minutes after. The contact angle stayed constant after 5 minutes.

	Time on surface (seconds)	**Crosslinker Ratio (%)**			
		0.25%	**0.5%**	**1%**	**3%**
PEGDA	10	51.1 ± 0.76	59.3 ± 1.28	85.7 ± 0.53	89.4 ± 0.83
	60	40.9 ± 0.77	41.1 ± 0.69	75.8 ± 0.5	84.2 ± 1.07
	300	20.6 ± 0	24.9 ± 0	42.4 ± 0	58.6 ± 0
MBA	10	76.3 ± 8	87.9 ± 3.96	94.9 ± 3.43	
	60	51.9 ± 5.76	63.1 ± 9.6	86.7 ± 4.7	
	300	24.8 ± 4.37	43.4 ± 7.81	56.2 ± 6.85	

4.5.2 Tuning the Surface for Maximum Frost Delay

Based on the previous section, it is clear that PEGDA is the optimal crosslinker to enhance the icing delay time, but there are other characteristics that can further affect the performance of the network. As described in section 4.2, the ability for these SBMA networks to delay icing is dependent on the amount of water that the surface can absorb into a non-freezable, bound state. This was supported by the correlation between thickness and icing delay time, shown in **Figure 4.9**, which follows a linear trend and correlates to an icing delay of 30 seconds for each μm of coating. This follows our assumptions that a larger volume would be able to absorb more water into a non-freezable, bound state due to the greater number of binding sites.

The linear trend also has a negative intercept which agrees with our assumption that as the thickness gets sufficiently thin, the Gibbs free energy barrier dominates the ice formation. Therefore, to maximize the performance of an SBMA network, the thickness should be maximized, though there will be an upper limit at which the diffusion of water through the surface is inhibited by the thickness and delaying will not be delayed further. This also implies that the thickness can be tuned to the specific needs of the application, take for example, a freezer condensing coil will need a balance of icing inhibition (requiring a thick coating) and the heat transfer to the air (requiring a thin coating).

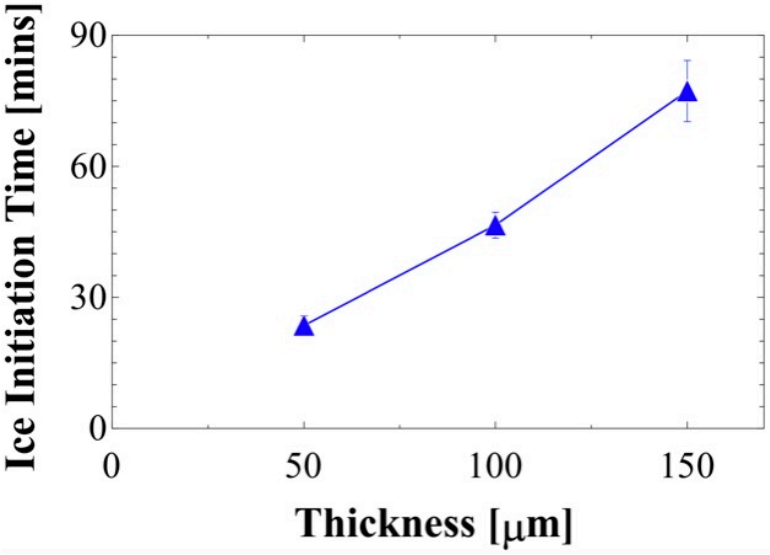

Figure 4.9: Correlation between ice initiation time and thickness of the SBMA network crosslinked by 0.25% PEGDA. The correlation follows a linear trend implying that for every μm of coating, the icing time will be delayed approximately 30 seconds.

The diffusion of water and accessibility of binding sites was also directly investigated. As the crosslinker ratio increases, the crosslink density of the network would also increase, and the network more tightly bound. This would have a two-fold effect, a reduction in diffusion and reduction in binding sites. As the network gets more tightly bound with increasing crosslinker, the diffusion of water through the network to reach the binding sites slows down. Additionally, as more of the reactive sites on the SBMA are occupied by the crosslinker, there is a reduction in the number of binding sites. Both of these factors combine to reduce the amount and the rate at which water can be absorbed into the network and reduces the ice initiation time, as shown in **Figure 4.10**. Once the crosslinker ratio is high enough, the crosslink density of SBMA reaches steady state and does not vary significantly with the amount of crosslinker. At this point, the icing time remains mostly constant, showing the direct correlation between the icing time and crosslink density.

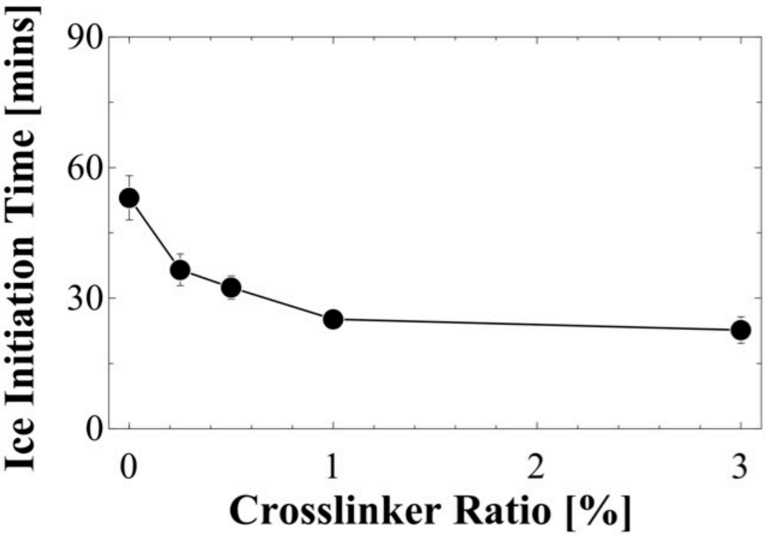

Figure 4.10: Correlation between the icing time and crosslinker ratio of PEGDA. Increasing the crosslinker ratio, increases the crosslink density of the network. Eventually the network reaches a steady state crosslink density, and the icing time remains constant.

4.5.3 Performance of Optimized Surface

Based on the analysis in sections 4.5.1 and 4.5.2, it is clear that an optimized SBMA network for anti-icing would be a crosslinked by PEGDA, maximally thick, and the excess SBMA monomer would not be flushed from the network (unflushed). Using this optimized coating, we were able to make direct comparisons of the anti-icing ability which is displayed in **Figure 4.11**. The optimized 0.25% PEGDA, 150 μm coating far exceed the performance of any other surface, delaying icing by 600% more than a current state of the art technology of lubricated porous surfaces. It is also notable that the SBMA silane, a monolayer of SBMA, still delayed icing by about 25% compared to an untreated surface, further exemplifying the water binding capabilities of the SBMA and the thickness correlation to the volume of water bound.

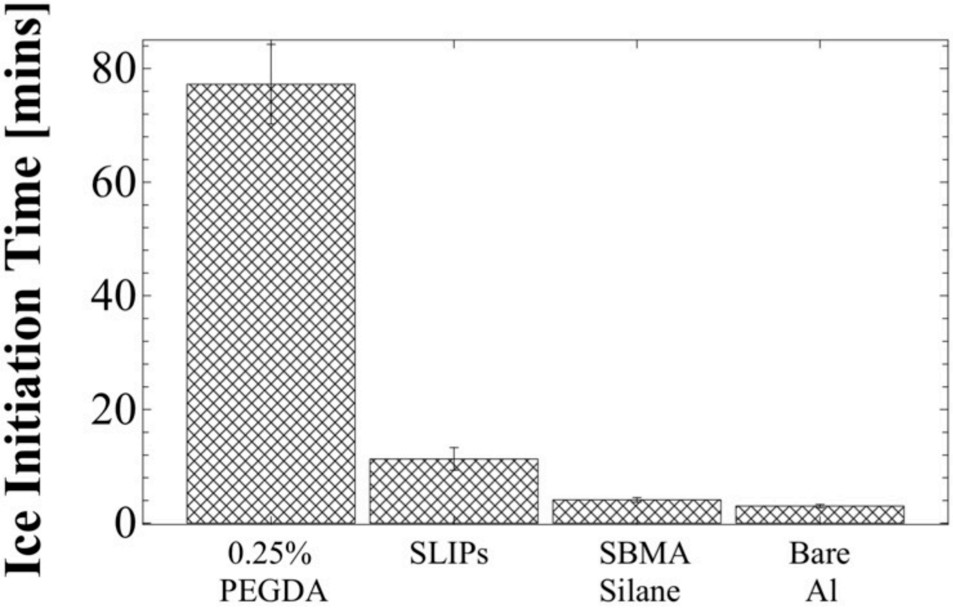

Figure 4.11: Performance comparison of icing delay of various surfaces. The 0.25% PEGDA is our optimized surface at 150 µm thick, SLIPs is a lubricated surface, SBMA silane is a monolayer of SBMA, and the bare aluminum is untreated.

It was equally important to display the longevity of an anti-icing surface as any coating for widescale use would go through thousands of freeze-thaw cycles in its lifetime, and the cyclic performance of the SBMA networks is shown in **Figure 4.12**. A counterion or lubricated surface would degrade over time as the anti-icing constituent (lubricant or free ions) are susceptible to removal by the liquid water during the thaw cycle. Whereas the SBMA networks would maintain their performance since the SBMA is bound into a network. Although an unflushed surface would see a decline in performance as the free SBMA is removed with melting ice, the performance would not drop below that of the flushed surface.

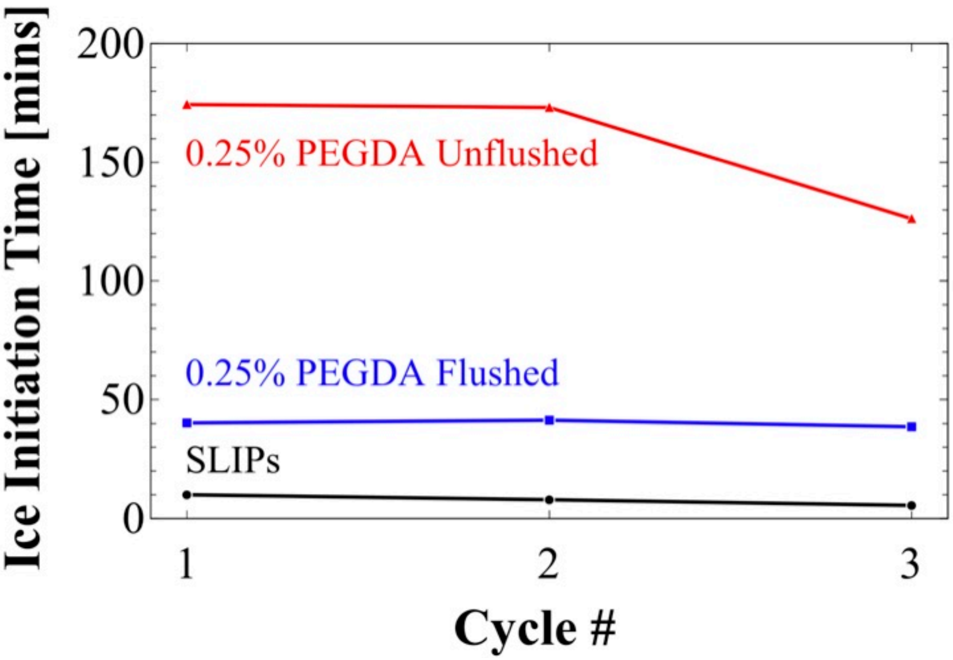

Figure 4.12: Cyclic performance of a flushed and unflushed SBMA network compared to SLIPs. Where the SLIPs saw a decline in performance of 50%, there was no change in the performance of the flushed network. The unflushed network saw a minor decline, though it would not drop below that of the flushed network.

Lastly, we compared the performance of the SBAM networks at different subcooling conditions. As mentioned previously, prior publications have used a wide variety of experimental conditions, so we wanted to check for any temperature dependence of the coating. Interestingly the icing time is dramatically extended by a marginal shift from -20°C to -10°C surface temperature, as shown in **Figure 4.13**. This is important when considering the absolute performance of each surface. As mentioned in section 4.4.2, these tests were performed in an accelerate fashion, in actual use conditions, the ambient temperature and humidity would be significantly lower, slowing the rate of water absorption into the network. **Figure 4.13** shows that the icing delay time increases non-linearly with the surface-ambient temperature differential indicating these SBMA networks could exhibit ice resistance for many hours in actual use. Interestingly, there also appears to be a crossover point at which the MBA crosslinked networks begin performing better than the PEGDA networks. It is unclear what is leading to this relative performance different, though they are within the standard error of each other and the difference may not be as pronounced as it appears.

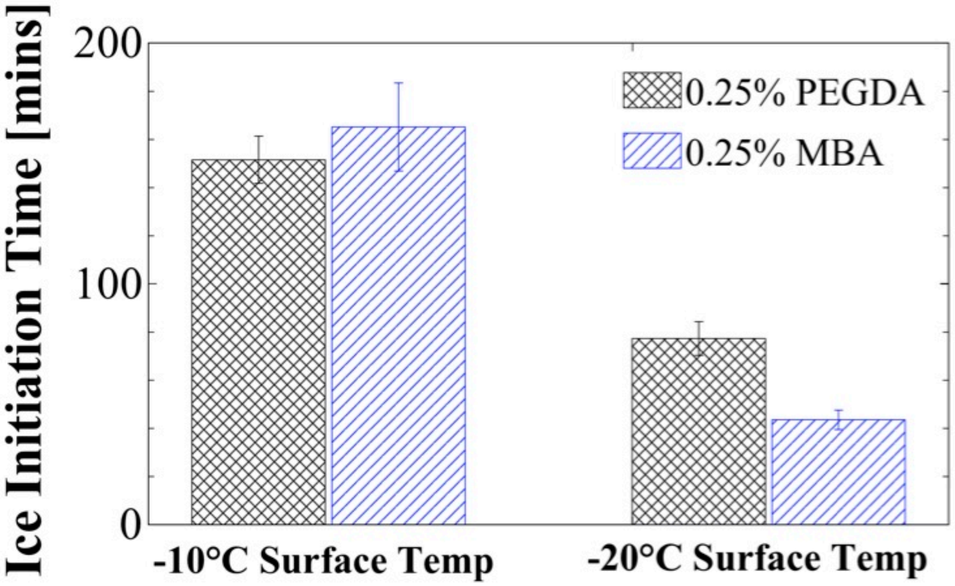

Figure 4.13: Comparison of 0.25% crosslinker, 150 μm SBMA network with PEGDA and MBA at different surface cooling temperatures. The performance of each surface increases dramatically with a marginal increase in surface temperature indicating very good performance in real world conditions. There is also a crossover in performance between the two crosslinkers between -20°C and -10°C.

4.5.4 Heterogeneous Ice Nucleation Suppression

A good test of ice inhibition is in measuring the time for heterogeneous ice nucleation to commence. Since the droplet is the same volume for all the surfaces, the test is independent of the rate of condensation or absorption on the surface, which is dependent on contact angle. The elapsed time for a 20 μl droplet of water on a surface to initiate ice nucleation is shown in **Figure 4.14**. The SBMA based surfaces all outperformed the lubricated surface despite the droplets spreading out more which would accelerate the heat transfer out of the water. This indicates that there is not only strongly bound, non-freezing water, but also a suppression in the heterogeneous ice nucleation of water since not all of the liquid is absorbed into the network. This is likely caused by a suppression in the ice nucleation temperature by weakly bound water which inhibits ice formation for many times longer than on the untreated surface. The unflushed network also likely had free SBMA diffusing into the droplet, thereby further suppressing the ice nucleation compared to the unflushed network. This far surpasses the HIN inhibition time for a counterion surface, previously published at 2200 seconds, or about 38 minutes.[122,123]

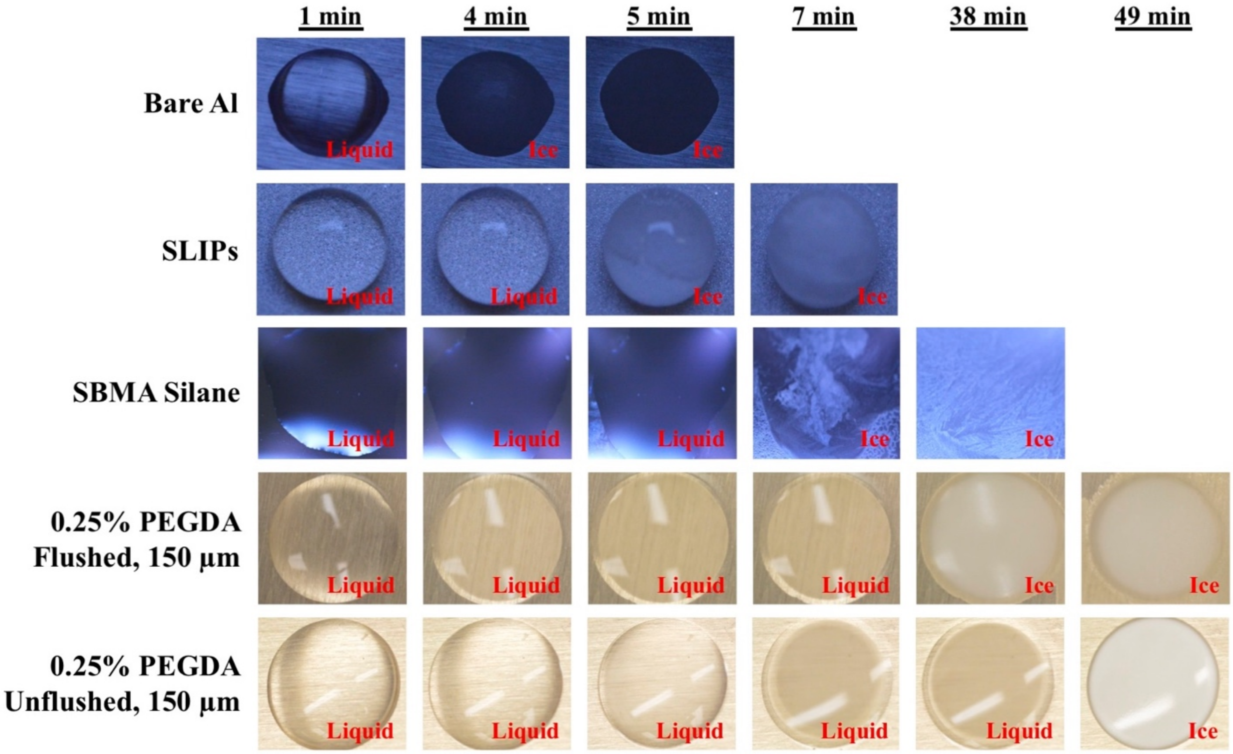

Figure 4.14: Elapsed time for the commencement of heterogeneous ice nucleation of a 20 µl droplet on a variety of surfaces. The time corresponding to the first instance of ice in the images is the time at which icing initiated. The SBMA surfaces all outperformed the SLIPs surface while the unflushed SBMA network delayed HIN by more than 1000%.

4.6 Conclusion

We have successfully demonstrated a very simple and effective anti-icing coating developed from an SBMA network that can be easily scaled based on the desired performance parameters. By selecting a more hydrophilic crosslinker, we were able to optimize the performance of the network. The coating can then be customized for each application by varying the thickness for desired anti-icing properties or heat transfer performance, and by varying the crosslink density for anti-icing performance or durability. Lastly, we successfully demonstrated superior anti-icing performance compared to prior state of the art technologies. Although there is variability in experimental conditions, under consistent conditions in this study, we demonstrated longer ice initiation times, superior durability in repeated freeze-thaw cycles, and great heterogeneous ice nucleation delay. The simple, 1-step application of this SBMA coating makes this an easily scalable materials that exhibits exceptional anti-icing performance.

Chapter 5

Heat Resistant Super-Hydrophobic Coating for High Boiling Heat Transfer Coefficient

This chapter is primarily adapted from an article drafted for *Nature Materials* and was part of a collaborative effort with John Heron and Ctirad Uher. Production of the target materials was performed by Trevor Bailey and Yinying Zhang. Deposition and characterization were performed by Peter Meisenheimer, who is an equal first author on the manuscript.

5.1 Introduction

Development of durable, hydrophobic surfaces has been a significant focus over the past several decades as it would have a wide range of useability like commercial condensers, cookware and ovens, automotive, naval drag reduction, and many more.[284–287] While the functionality of super-hydrohpobic surfaces has made significant progress, the durability and usability of these surfaces have hindered by complex geometries and/or the coating stability, preventing their widespread adoption.[214,288–291] Self-healing surfaces were developed to withstand damage but continuously renew the surface with hydrophobic properties[292–295]. Recent advances have been made to develop materials with hydrophobic properties throughout the bulk which maintain their hydrophobic properties even after wear and damage[296–298]. These types of surfaces all cover up the effects of damage to the surface caused by mechanical or chemical attack. This work presents a material that is, instead, resistant to damage so it can be applied at nanoscale thickness and maintain hydrophobic properties in harsh environments. Such a coating would be particularly useful in boiling applications that require high heat transfer coefficients.

Demand for industrial heat sinks that can rapidly remove large amounts of heat have become a focus with electronic chips.[299] The trend towards smaller and smaller microelectronics has driven the need for larger heat removal capacity over a smaller area.[300] Microelectronics and micro-electromechanical systems (MEMS) require high heat dissipative rates, and pool boiling in a non-conductive liquid is recognized as an effective technique due to the high heat fluxes that can be achieved.[301,302] Since the performance of such systems deteriorates with heat, it is desirable to dissipate heat at low superheat (temperature above the boiling temperature of the liquid).[303]

Diamond-like carbon (DLC) is of particular interest because it exhibits exceptional physical, mechanical, and inert properties that no other low surface energy coating has displayed. DLC, also referred to as amorphous carbon, is characterized by a combination of sp^2 and sp^3 bonds with the former contributing to a more "graphitic" and the later forming a harder, more "diamond-like" film[304]. It offers excellent compromise between graphite and diamond in that it is significantly harder and more durable than graphite but easier and cheaper to produce than diamond[305].

DLC has been studied extensively since it was discovered in 1971[306], but much of the research since its discovery has focused on optimizing the film's optical, dielectric, abrasion, and/or friction properties[307–315]. While some work has been done to investigate surface energy modification of DLC, this has certainly not been the focus, and it has been exclusive to films deposited by plasma enhanced vapor deposition (PECVD)[316–321]. The addition of fluorine into the DLC reduces the hardness of the film, and the deposition using PECVD introduces contamination with hydrogen and/or oxygen further reducing the hardness and durability of the film[322–324].

This introduction of hydrogen into the film is the most significant hinderance in creating a durable, scratch resistant, and hydrophobic coating as increased hydrogen content leads to graphitization which softens the film and creates a more “polymer-like” hardness[325,326]. The PECVD process inherently includes hydrogen into the films since the process gases are hydrocarbon based[327]. Pulsed Laser deposition (PLD) has been used recently to create hydrogen free DLC films; this method uses a high-powered laser directed at a carbon-based target inside a vacuum chamber. The plume of ablated material from the laser creates a directed flux at a relatively low temperature target[328]. The high energy carbon atoms impinging on the surface, combined with the limited atom mobility on the cold surface contributes to a high degree of sp^3 bonding, up to 85%[236]. This combination of a fluorinated, high sp^3 content carbon film should provide for a durable hydrophobic film that can resist high temperature degradation.

5.2 Design Criteria for Heat Stability

Diamond-like carbon has also shown high temperature resistance, maintaining performance above 500°C.[230,231] Though there has been some evidence that diamond-like carbon begin to degrade and oxidize above 500°C, this would still be in excess of the current limits for superhydrophobic coatings.[232] The addition of dopants would allow for control over the wettability of the coating. In Chapter 3, we examined the influence of silicon as a dopant, though this did not impart a significant enough drop in surface energy to create a hydrophobic surface.

Therefore, fluorine dopant is necessary to create a hydrophobic surface with a high enough contact angle to maintain a superhydrophobic cassie-baxter state. This high contact angle should lead to a high heat transfer coefficient with a large heat flux at low superheat temperatures.

5.3 Materials and Methods

5.3.1 Pulsed Laser Deposition

The DLC was deposited using PLD with the same tool as described in section 3.3.1. Samples were deposited from stoichiometric targets by ablation from a 248 nm KrF excimer at 30 °C and in 20 mTorr Ar for 2,000 shots. Samples were deposited at a pulse rate of 1 Hz. Final film thickness of samples was approximated by a lift-off photolithography process, after which height was determined using AFM. The thickness correlation was approximately 1 shot per Å deposited for fluorinated DLC.

5.3.2 Target Forming

There has been no prior work to deposit a fluorinated diamond-like carbon film using pulsed laser deposition. One of the difficult barriers in creating such a film is creating the target material. In PECVD, the flow rates of the hydrocarbon and fluorocarbon gases can be varied to achieve different fluorination ratios, but with PLD, the target must be created with the intended stoichiometry[329,330]. This presents additional difficulty as there are limited pure fluorocarbon solids that contain no additional elements, the ones that do exist are difficult to create a dense target to be used for PLD, and it is difficult to create targets with tunable ratios as substance, like PTFE, have fixed F:C ratios (2:1). For this study we used graphite powder for the carbon source, and a fluorinated graphite, $CF_{1.1}$, for the fluorine source and mixed the powders to achieve the target stoichiometry. The difficulty comes in that carbon typically anneals around 1800°C whereas the fluorinated graphite degrades at 550°C. This created significant difficulty in creating viable targets as they needed to be hard and rigid for deposition to be performed properly. Targets were formed with a variety of stoichiometries to determine if the variation in graphite and fluorinated graphite changed the annealing properties. A series of different target forming methods were used as outlined below:

1. Targets were pressed in a 20 mm diameter stainless steel die with 24,000 pounds of force. After the force was removed, the target was removed from the die and annealed at 350°C for 100 hours.
2. Targets formed using spark plasma sintering. The mixed powder was consolidated in a 20 mm diameter graphite die lined with graphite paper under an axial compressive stress of 50 MPa in vacuum inside a spark plasma sintering furnace (KCE – FCT HP D 10 – SD spark plasma sintering furnace) for 4 hours at a sintering temperature of 400°C.
3. Targets formed using spark plasma sintering, described in #2, but a small fraction (2-10%w) of Teflon AF was dissolved in Vertrel XF with the mixed powder. The XF was then allowed to evaporate so the powder was evenly coated with Teflon AF to serve as a binder.
4. Targets formed using spark plasma sintering, described in #2 above, but the mixed powder was a combination of Teflon and graphite. Teflon powder was mixed with graphite to achieve the desired fluorine to carbon ratio and the Teflon would serve as a binder and fluorine source. These targets were pressed at 250°C, above the glass transition temperature but below the melting temperature of Teflon.

Ultimately, none of the above procedures produced targets hard enough for deposition. All of the targets either fell apart when impacted by the laser, or in the case of those with Teflon, the

Teflon melted when struck by the laser which caused the target to fall apart. The best targets formed were made from pure fluorinated graphite and pressed using spark plasma sintering, as described in #2 above, for 4 hours at 400°C. Although this did not allow for stoichiometric variation of the samples, it did lead to a target with only fluorine and carbon, both about 50% stoichiometrically.

5.3.3 Contact Angle

Advancing and receding contact angles for the liquids were obtained from a sessile drop method using a Ramé-Hart 200 F1 contact angle goniometer. A dispensing needle was placed just above the substrate surface and a 10 μL droplet was suspended from the needle. The volume of the droplet was then increased to obtain advancing contact angles and decreased to obtain receding contact angles. DROPImage Advanced software was used to obtain the contact angle using a circular drop fit. Three points on each substrate were measured, and the mean value and drop images shown in results.

5.3.4 Surface Characterization

Hardness was measured in accordance with the nano-indentation procedure outlined in section 3.3.4. XPS and AFM were also performed on the sample, in accordance with the procedures outlined in section 3.3.6.

5.3.5 Abrasion

The mechanical durability test was performed by comparing the θ_{adv} and θ_{rec} with both water after a series of linear Taber abrasions. A sample was coating with the fluorinated DLC as described in section 5.3.1. The sample was then mounted to a Taber model 5750 Linear Abrader which had a CS-5 (~12.5 mm diameter) abrasive felt tip attached, and a 500-gram load was applied which produced an equivalent pressure of about 40 kPa. The abrasion head was moved in a reciprocating fashion back-and-forth across the surface in a one-inch length at a speed of 60 cycles/min. After a set number of abrasions, the system was stopped, the surface rinsed with acetone, IPA, and water, and the sample was dried with compressed air. The contact angles were measured at three different places along the abrasion length using both water and hexadecane. After the contact angles were measured, the sample was returned to the abrader for additional abrasion cycles. The contact angles were collected after every 1000 abrasion cycles initially, and then every 3500 cycles thereafter.

The F-DLC sample was compared to a fluorinated monolayer (F13Cl, deposition described in 2.3.1) and a superhydrophobic aluminum. The superhydrophobic aluminum was manufactured from an aluminum substrate (6061 T6 Aluminum Alloy, McMaster-Carr) which was first etched in 2.5 molar hydrochloric acid (Fischer Scientific) for 20 minutes to create nano-structure. It was then agitated in a bath sonicator for 10 minutes to remove loose aluminum particles and placed in boiling water to convert the outer layer to boehmite nano-crystals (γ-AlO(OH)). The textured aluminum was reacted with a vapor of (heptadecafluoro-1,1,2,2-tetrahydrodecyl)triethoxysilane (Gelest) in a vacuum oven at 100℃ and ~5 mTorr for 24 hours. After cooling, it was rinsing with Vertrel XF, Toluene, and IPA.

5.3.6 Heat Transfer

Heat transfer measurements were collected by the same method outlined in section 3.3.8. No variations to the method were employed for this chapter.

5.4 Results

Many of the target combinations outlined in section 5.3.2 resulted in targets that could not be deposited by PLD due to being too soft, or targets that when deposited, resulted in large particulates being deposited on the surface and not forming a diamond-like coating. The target that gave the best results was the pure fluorinated graphite target pressed at 400°C for 4 hours. The resulting coating was slightly rough, as displayed by the AFM results in **Figure 5.1**, with an RMS roughness of just over 50 nm. Although not as smooth as pure carbon diamond-like carbon, this is significantly smoother than the microscale roughness on many textured boiling surfaces.

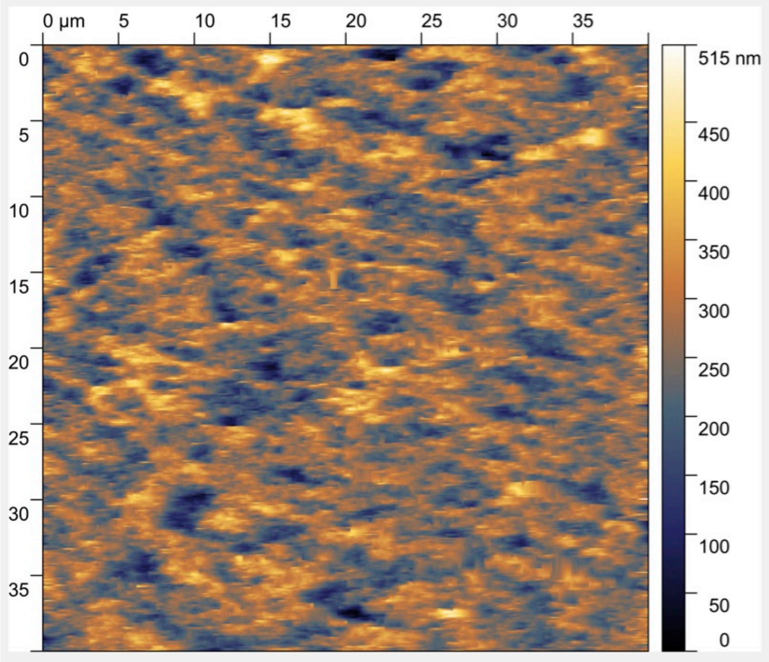

Figure 5.1: Atomic force microscopy (AMF) measurement of the as deposited fluorinated DLC from the pure fluorinated graphite target. The measured RMS roughness is 52.9 nm.

The XPS results of the deposited film also show high sp^3 bonding in the coating, as shown in **Figure 5.2**. The composition is nearly 40% sp^3 with less than 5% sp^2. There also exist three other peaks which comprise the remaining ~50% of carbon bonding, and these peaks are associated with various carbon-fluorine bonding groups. These irregular XPS peaks are known to come from pulsed laser deposition of polymers and are due to various local arrangements of carbon and fluorine groups.[331]

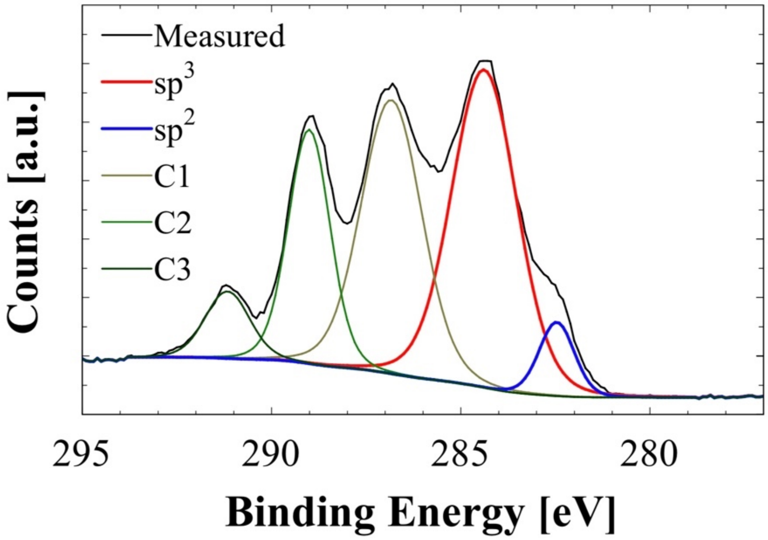

Figure 5.2: Carbon peaks of the collected XPS data. In addition to the sp^2 and sp^3 peaks, three additional carbon peaks were present which represented different carbon-fluorine bonding in the material that is not represented in the C-C bonding.

Although the resulting film is relatively smooth, the roughness present does induce a Cassie-Baxter wetting state, and shows good heat stability in **Figure 5.3**. The apparent contact angle of the coating was 154° with a 155° advancing contact angle and a 153° receding contact angle. The films also maintained its superhydrophobicity after thermal cycles to 400°C and 500°C, in atmospheric, conditions for 12 hours each. There was nearly no change in the contact angle or hysteresis after the thermal cycles indicating a good thermal stability of the final film compared to the fluorinated silane which degraded quickly at elevated temperature. A test was performed to heat the F-DLC to 700°C but the material appears to have evaporated off from the surface indicating that the thermal limit for the material lies between 500°C and 700°C.

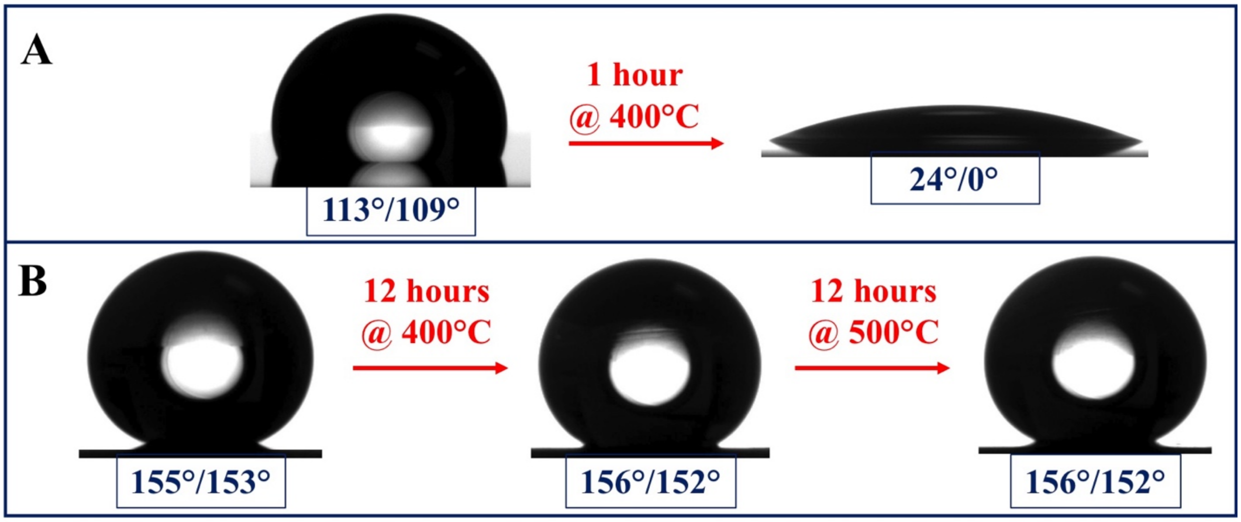

Figure 5.3: Apparent contact angle collected by goniometry, of an **A)** fluorinated monolayer (F13Cl) and **B)** the fluorinated diamond-like carbon film. The fluorinated monolayer was wetting after just 1 hour at 400°C whereas the F-DLC remained superhydrophobic after 12 hours at 400°C and 500°C each.

Expectedly, the high contact angle of the F-DLC translated to a large improvement in the boiling heat transfer coefficient, as shown in **Figure 5.4**. The F-DLC displayed an HTC of 86.1 kW m^{-2} K^{-1} compared to just 39.5 kW m^{-2} K^{-1} for the bare Si, a 120% improvement. This performance was achieved while the critical heat flux was decreased by only 23%, from an average of 848 kW m^{-2} to 651 kW m^{-2}. This presents significant performance improvements for heat transfer, especially when considering microelectronics as the F-DLC can transfer that same amount of heat from the surface at a temperature about 20°C cooler than an uncoated surface.

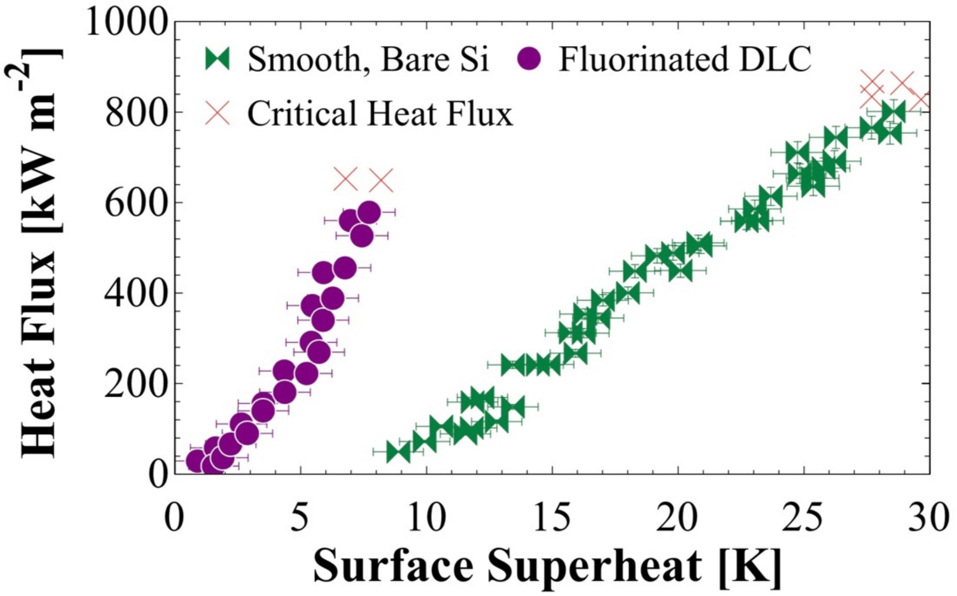

Figure 5.4: Boiling heat curve comparing the performance of fluorinated diamond-like carbon to an uncoated, high surface energy sample (bare silicon). The F-DLC displayed a heat transfer coefficient 120% higher than the bare Si while achieving a critical heat flux just 23% lower than the bare Si.

Lastly, mechanical durability was compared to a smooth hydrophobic surface (F13Cl) and a superhydrophobic, etched aluminum (SHP Al), shown in **Figure 5.5**. The F-DLC exhibited exceptional durability and sustained water in a Cassie-Baxter wetting state even after 10,000 linear abrasion cycles. This was a stark comparison to the etched aluminum which transitioned from a Cassie-Baxter state after just 4,000 cycles and was partially wetting after 8,000.

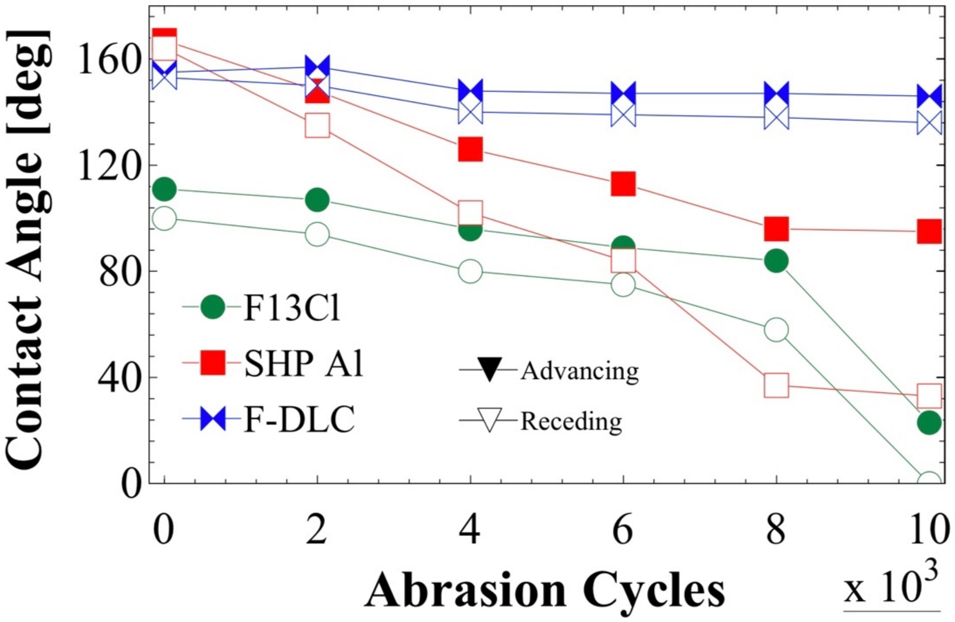

Figure 5.5: Apparent contact angle of water on fluorinated, diamond-like carbon (F-DLC) compared to a flat hydrophobic (F13Cl) and nanotextured superhydrophobic (SHP Al). The F-DLC had minimal change to the advancing and receding contact angles after 10,000 abrasion cycles and remained superhydrophobic whereas the fluorinated monolayer degraded to fully wetting, and the superhydrophobic aluminum transition to hydrophobic and eventually to partially wetting.

The culmination of these results show that a fluorinated diamond-like carbon surface can be produced that exhibits good thermal and mechanical durability while increasing the thermal transport rate for nucleate boiling. The deposited coating had a variety of bonding, though it was dominated by sp^3 C-C bonds which leads to the superior mechanical durability compared to a representative superhydrophobic surface. This also provides for the surface to maintain its superhydrophobicity after high temperatures where other fluorinated compounds would otherwise degrade. Lastly, due to the high contact angle and high thermal stability, the F-DLC enhanced the heat transfer coefficient more than 2-fold for boiling heat transfer and maintained its performance after repeated tests.

5.5 Conclusion

In this chapter, we present a novel method of depositing fluorine doped diamond-like carbon (F-DLC) with a high degree of sp^3 C-C bonding. This novel surface is superhydrophobic, with an apparent contact angle above 140°, and sustains water in a Cassie-Baxter wetting state. Where a traditional superhydrophobic surface would degrade at high temperatures or under harsh abrasion and be unable to sustain superhydrophobicity, the F-DLC remains superhydrophobic. One of the key applications for such a high temperature stable, hydrophobic surface, would be in microelectronic applications. Microelectronics utilize nucleate boiling to cool the systems and they require high thermal transport at low superheat temperatures. We show that the deposited F-DLC dramatically increases the heat transfer coefficient as compared to an uncoated surface and can transport a similar amount of heat at about 20°C cooler. This difference can lead to significant efficiency and performance gains for electronics cooling and similar applications.

Chapter 6

Summary and Future Outlook

6.1 Hygrophilic Condensation Surfaces

The condensation work published in this thesis is groundbreaking and presents major advances in the breadth of surfaces capable of being used for condensation heat transfer. Not only did we successfully display dropwise condensation on multiple surfaces with contact angles never before used for this mode, but we also showed increases in both HTC and CHF with these surfaces. This work ushers in a new classification of solid surfaces that can be used to maximize the capabilities of condensation heat transfer.

There is still room for additional work to make these surfaces fully scalable and useable on an industrial scale. First, we were unable to identify a truly “optimal” surface for some liquids. Examining **Figure 2.7**, although the surfaces identified herein are nearer the maximum peak compared to prior work, they are not at the absolute maximum. Creating a surface with the exact correct contact angle would allow for the maximum achievable heat transfer coefficient and the most efficient condensing surface. Furthermore, although our surfaces displayed very low hysteresis, there is still opportunity for additional improvements. Reducing the hysteresis further will enhance condensation further, though this becomes increasingly more difficult as you get nearer 0° hysteresis. A better understanding of the true glass transition temperature could provide additional insight into the amorphous behavior of the solid surfaces. Since the silanes used were based on polymers, the T_g was assumed to be similar to that of the virgin polymer, though this may not be exact. Using an ellipsometer with a cooling stage that can reach sub-zero temperatures, valuable insights into the behavior of these surfaces could be gathered. This could enable better tuning of future surfaces and how to further reduce the hysteresis.

Another avenue of opportunity to further improve condensation surfaces could be in creating solid polymer networks reacted with oils or other ultra-low T_g polymers. This would, in essence, create a lubricated surface but with the lubricant now covalently bound to the network and surface. By having the lubricant bound to the surface, it could provide the lubricating effects seen in previous studies and allow the condensate to be easily removed, but the lubricant will not cloak the droplets and deplete from the surface. One risk of this route would be the increased thermal resistance of the network though this could be mitigated with very thin or conductive coatings.

Lastly, the deposition methods of any prospective surface need to be scaled to be easily applied. Although we displayed condensation on coated copper tubes, they did require extensive pre-treatment. Developing a more facile deposition process that can be used for current industrial condensers would be critical to realize the gains from any solution.

6.2 Temperature Stable Diamond-Like Carbon for Boiling

The published work on a smooth and durable boiling surface is the first to show stable, enhanced boiling heat transfer on a smooth surface. However, this is only the beginning of the capabilities that finely tuned diamond-like carbon can present. Studies have shown that the doping with different elements (oxygen, nitrogen, hydrogen) can have different effects on the wettability, though there is no clear guide as to how. Understanding this interplay in elemental doping and being able to tune the contact angle and hysteresis opens up a huge variety of uses for DLC. In addition to being able to further improve the boiling heat transfer, these surfaces could also be used to condensation. Future focus of this work should examine how dopants into the DLC can be used to control the wetting characteristics and then developing a series of surfaces with a variety of contact angles and low hysteresis.

Another interesting use for such surfaces could come in the solid fouling characteristics. Anti- corrosion, biofouling, and micro-organism surfaces have significant value in marine shipping industry. A diamond-like carbon surface that can resist solid fouling would be particularly valuable with its added durability that would prevent damage and require less frequent upkeep. Finely tuned diamond-like carbon presents the greatest growth opportunity of any surface material in this dissertation if it can be well understood and closely controlled.

6.3 Anti-Icing Poly-Zwitterionic Network

The anti-icing surface present in chapter 4 is the first coating of its kind that can be easily produced and scaled. This surface can easily be tuned for a variety of applications from industrial refrigeration to commercial aircraft. While the poly-SBMA network showed significant improvement in delaying ice formation, the durability of the coating needs to be improved before it can reach widescale use. Defects tended to induce ice crystallization, so damage to the surface has the potential to reduce the efficacy of the surface. Increasing the durability of the surface while also finding a method to mitigate the crystallization around defects would significantly expand the useability of the surface. Additionally, some surfaces were particularly fragile and prone to cracking under certain conditions. As the crosslinking ratio increased, the networks were noticeably more brittle and prone to cracking if left in a dry environment too long. This was especially pronounced with the flushed networks, as we believe the excess SBMA in the unflushed networks acted as a plasticizer and increased the elasticity of the network. Unfortunately, in normal application, the network would eventually become flushed with the icing/deicing cycles, and since these surfaces would normally operate in dry conditions, they would be susceptible to this cracking. Addition of a plasticizer that could not be removed from the surface would be one potential route to resolving this brittleness.

6.4 Heat Stable Superhydrophobic Diamond-Like Carbon

The fluorinated diamond-like carbon presented in the final research chapter is a promising proof of concept that exemplifies significant promise for future surfaces, but as it currently stands, requires further development and refinement to be fully useful. Although the deposited surface exhibited superior temperature stability to other wettability modifying solids, the F-DLC did not remain stable up to 700°C as was seen with the Si-DLC. This is not completely unexpected as other studies have found that the stability of diamond-like carbon surfaces can vary above 500°C. One likely pathway to stabilize the film would be the addition of small amounts of other elements, like silicon, which have been shown to induce temperature stability above 500°C.

Most important to refine is the deposition process to create a more uniform and smoother surface. The primary limitation with pulsed laser deposition is that the target needs to be hard to get a good deposition from it. As we saw with the F-DLC, it is incredibly difficult to create targets suitable for deposition given the instability of fluorine. If PLD is desired, a different target formation process, or different constituents, will be needed to get higher quality targets to deposit from. An alternative route would be to deposit with plasma enhanced chemical vapor deposition (PECVD) and refine the process to remove hydrogenation. Using PECVD would lead to significantly smoother films and more uniform chemical bonding which would eliminate much of the irregular C-F bonding seen in **Figure 5.2**. If a different gaseous carbon source can be identified for PECVD that would reduce the hydrogen content of the film and allow for a purer stoichiometry, the high hardness and sp^3 content can be achieved with PECVD that are typical with PLD.

6.5 Closing Remarks

As a whole, the field of surface science is addressing engineering challenges on a micro- and nano- scale and remain a fascinating study as we try to control liquids around us. Phase transformation is particularly interesting as we attempt to just reach a point in which we can even replicate nature which has found unique ways to control phase transformation better than we can. The work in this thesis represents only a small insight into the global effort to use engineered surfaces to control and enhance performance of phase transformation interfaces for a variety of applications. Materials research is an ever-evolving field and the high demand for condensation, boiling, and anti-icing surfaces will ensure that this research area will remain of particular interest for the foreseeable future.

References

1. Bhushan B, Jung YC. Natural and biomimetic artificial surfaces for superhydrophobicity, self-cleaning, low adhesion, and drag reduction. *Progress in Materials Science*. 2011;56(1):1-108. doi:10.1016/j.pmatsci.2010.04.003

2. Rajappan A, Golovin K, Tobelmann B, et al. Influence of textural statistics on drag reduction by scalable, randomly rough superhydrophobic surfaces in turbulent flow. *Physics of Fluids*. 2019;31(4):042107. doi:10.1063/1.5090514

3. Liu Y, Liu Z, Liu Y, et al. One-Step Modification of Fabrics with Bioinspired Polydopamine@Octadecylamine Nanocapsules for Robust and Healable Self-Cleaning Performance. *Small*. 2015;11(4):426-431. doi:10.1002/smll.201402383

4. Collier JG, Thome JR. *Convective Boiling and Condensation*. Clarendon Press; 1994.

5. Betz AR, Xu J, Qiu H, Attinger D. Do surfaces with mixed hydrophilic and hydrophobic areas enhance pool boiling? *Appl Phys Lett*. 2010;97(14):141909. doi:10.1063/1.3485057

6. Cha H, Vahabi H, Wu A, et al. Dropwise condensation on solid hydrophilic surfaces. *Sci Adv*. 2020;6(2):eaax0746. doi:10.1126/sciadv.aax0746

7. Takata Y, Hidaka S, Masuda M, Ito T. Pool boiling on a superhydrophilic surface. *International Journal of Energy Research*. 2003;27(2):111-119. doi:10.1002/er.861

8. Jaikumar A, Kandlikar SG. Ultra-high pool boiling performance and effect of channel width with selectively coated open microchannels. *International Journal of Heat and Mass Transfer*. 2016;95:795-805. doi:10.1016/j.ijheatmasstransfer.2015.12.061

9. Chen X, Wu J, Ma R, et al. Nanograssed Micropyramidal Architectures for Continuous Dropwise Condensation. *Advanced Functional Materials*. 2011;21(24):4617-4623. doi:10.1002/adfm.201101302

10. Anand S, Paxson AT, Dhiman R, Smith JD, Varanasi KK. Enhanced Condensation on Lubricant-Impregnated Nanotextured Surfaces. *ACS Nano*. 2012;6(11):10122-10129. doi:10.1021/nn303867y

11. Miljkovic N, Enright R, Nam Y, et al. Jumping-Droplet-Enhanced Condensation on Scalable Superhydrophobic Nanostructured Surfaces. *Nano Lett*. 2013;13(1):179-187. doi:10.1021/nl303835d

12. Cooke D, Kandlikar SG. Pool Boiling Heat Transfer and Bubble Dynamics Over Plain and Enhanced Microchannels. In: American Society of Mechanical Engineers Digital Collection; 2011:163-172. doi:10.1115/FEDSM-ICNMM2010-31147

13. Kim H, Ahn HS, Kwak HJ, Kim MH, Kim DE. Boiling crisis controlled by capillary pumping and viscous friction: Liquid penetration length and dry spot diameter. *Appl Phys Lett*. 2016;109(24):243901. doi:10.1063/1.4971986

14. Mikic BB, Rohsenow WM. A New Correlation of Pool-Boiling Data Including the Effect of Heating Surface Characteristics. *Journal of Heat Transfer*. 1969;91(2):245-250. doi:10.1115/1.3580136

15. Young T. III. An essay on the cohesion of fluids. *Philosophical Transactions of the Royal Society of London*. 1805;95:65-87. doi:10.1098/rstl.1805.0005

16. Marmur A. Equilibrium contact angles: theory and measurement. *Colloids and Surfaces A: Physicochemical and Engineering Aspects*. 1996;116(1):55-61. doi:10.1016/0927-7757(96)03585-6

17. Ramé E. The Interpretation of Dynamic Contact Angles Measured by the Wilhelmy Plate Method. *Journal of Colloid and Interface Science*. 1997;185(1):245-251. doi:10.1006/jcis.1996.4589

18. Restagno F, Poulard C, Cohen C, Vagharchakian L, Léger L. Contact Angle and Contact Angle Hysteresis Measurements Using the Capillary Bridge Technique. *Langmuir*. 2009;25(18):11188-11196. doi:10.1021/la901616x

19. Takenaga M, Jo S, Graupe M, Lee TR. Effective van der Waals surface energy of self-assembled monolayer films having systematically varying degrees of molecular fluorination. *Journal of Colloid and Interface Science*. 2008;320(1):264-267. doi:10.1016/j.jcis.2007.12.048

20. Peng H. Synthesis and Application of Fluorine-Containing Polymers with Low Surface Energy. *null*. 2019;59(4):739-757. doi:10.1080/15583724.2019.1636390

21. Grainger DW, Stewart CW. Fluorinated Coatings and Films: Motivation and Significance. In: *Fluorinated Surfaces, Coatings, and Films*. Vol 787. ACS Symposium Series. American Chemical Society; 2001:1-14. doi:10.1021/bk-2001-0787.ch001

22. Tuteja A, Choi W, Ma M, et al. Designing Superoleophobic Surfaces. *Science*. 2007;318(5856):1618-1622. doi:10.1126/science.1148326

23. Fordham S, Freeth FA. On the calculation of surface tension from measurements of pendant drops. *Proceedings of the Royal Society of London Series A Mathematical and Physical Sciences*. 1948;194(1036):1-16. doi:10.1098/rspa.1948.0063

24. du Noüy PL. A NEW APPARATUS FOR MEASURING SURFACE TENSION. *J Gen Physiol*. 1919;1(5):521-524. doi:10.1085/jgp.1.5.521

25. Pallas NR, Pethica BA. The surface tension of water. *Colloids and Surfaces*. 1983;6(3):221-227. doi:10.1016/0166-6622(83)80014-6

26. Mysels KJ. The maximum bubble pressure method of measuring surface tension, revisited. *Colloids and Surfaces*. 1990;43(2):241-262. doi:10.1016/0166-6622(90)80291-B

27. Jones G, Frizzell LD. A Theoretical and Experimental Analysis of the Capillary Rise Method for Measuring the Surface Tension of Solutions of Electrolytes. *J Chem Phys*. 1940;8(12):986-997. doi:10.1063/1.1750615

28. Grigoryev BA, Nemzer BV, Kurumov DS, Sengers JV. Surface tension of normal pentane, hexane, heptane, and octane. *International journal of thermophysics*. 1992;13(3):453-464.

29. Postigo MA, Zurita JL, De Soria MLG, Katz M. Surface tensions of binary mixtures:2-propanol+dichloromethane and n-pentane+methylacetate at 298.15 K. *Colloids and Surfaces*. 1989;23(3):231-240. doi:10.1016/0166-6622(89)80337-3

30. Nishikido N, Mahler W, Mukerjee P. Interfacial tensions of perfluorohexane and perfluorodecalin against water. *Langmuir*. 1989;5(1):227-229.

31. Kahl H, Wadewitz T, Winkelmann J. Surface Tension of Pure Liquids and Binary Liquid Mixtures. *J Chem Eng Data*. 2003;48(3):580-586. doi:10.1021/je0201323

32. Wang Y, Sang DK, Du Z, Zhang C, Tian M, Mi J. Interfacial Structures, Surface Tensions, and Contact Angles of Diiodomethane on Fluorinated Polymers. *J Phys Chem C*. 2014;118(19):10143-10152. doi:10.1021/jp501683d

33. Daniel D, Mankin MN, Belisle RA, Wong T-S, Aizenberg J. Lubricant-infused micro/nano-structured surfaces with tunable dynamic omniphobicity at high temperatures. *Appl Phys Lett*. 2013;102(23):231603. doi:10.1063/1.4810907

34. Tan M, Zhang H, Wang Y, Ma H, Zhu J, Han J. Solvent effect on the formation of self-assembled monolayer on DLC surface between n-hexane and Vertrel XF. *Applied Surface Science*. 2008;254(20):6332-6336. doi:10.1016/j.apsusc.2008.03.174

35. Owens DK, Wendt RC. Estimation of the surface free energy of polymers. *Journal of applied polymer science*. 1969;13(8):1741-1747.

36. FOWKES FM. Attractive Forces at Interfaces. *Journal of Industrial and Engineering Chemistry*. 1964;56(12):40-52. doi:10.1021/ie50660a008

37. Preston DJ, Miljkovic N, Sack J, Enright R, Queeney J, Wang EN. Effect of hydrocarbon adsorption on the wettability of rare earth oxide ceramics. *Appl Phys Lett*. 2014;105(1):011601. doi:10.1063/1.4886410

38. Barquins M, Cognard J. Adhesion characteristics of gold surfaces. *Gold Bulletin*. 1986;19(3):82-86. doi:10.1007/BF03214647

39. Shojaei AH, Li X. Mechanisms of buccal mucoadhesion of novel copolymers of acrylic acid and polyethylene glycol monomethylether monomethacrylate. *Journal of Controlled Release*. 1997;47(2):151-161. doi:10.1016/S0168-3659(96)01626-4

40. Sundquist BE. A direct determination of the anisotropy of the surface free energy of solid gold, silver, copper, nickel, and alpha and gamma iron. *Acta Metallurgica*. 1964;12(1):67-86. doi:10.1016/0001-6160(64)90055-0

41. Cha S, Kim C. Poly(dimethylsiloxane) Stamp Coated with a Low-Surface-Energy, Diffusion-Blocking, Covalently Bonded Perfluoropolyether Layer and Its Application to the Fabrication of Organic Electronic Devices by Layer Transfer. *ACS Appl Mater Interfaces*. 2018;10(28):24003-24012. doi:10.1021/acsami.8b03811

42. Burnham NA, Dominguez DD, Mowery RL, Colton RJ. Probing the surface forces of monolayer films with an atomic-force microscope. *Phys Rev Lett*. 1990;64(16):1931-1934. doi:10.1103/PhysRevLett.64.1931

43. Lim BC, Thomas NL, Sutherland I. Surface energy measurements of coated titanium dioxide pigment. *Progress in Organic Coatings*. 2008;62(2):123-128. doi:10.1016/j.porgcoat.2007.10.002

44. Westerlind BS, Berg JC. Surface energy of untreated and surface-modified cellulose fibers. *Journal of Applied Polymer Science*. 1988;36(3):523-534. doi:10.1002/app.1988.070360306

45. Bhat NV, Upadhyay DJ. Plasma-induced surface modification and adhesion enhancement of polypropylene surface. *Journal of Applied Polymer Science*. 2002;86(4):925-936. doi:10.1002/app.11024

46. Tuteja A, Choi W, McKinley GH, Cohen RE, Rubner MF. Design Parameters for Superhydrophobicity and Superoleophobicity. *MRS Bulletin*. 2008;33(8):752-758. doi:10.1557/mrs2008.161

47. Roach P, Shirtcliffe NJ, Newton MI. Progess in superhydrophobic surface development. *Soft Matter*. 2008;4(2):224-240. doi:10.1039/B712575P

48. Cheng Y-T, Rodak DE. Is the lotus leaf superhydrophobic? *Appl Phys Lett*. 2005;86(14):144101. doi:10.1063/1.1895487

49. Ma M, Hill RM. Superhydrophobic surfaces. *Current Opinion in Colloid & Interface Science*. 2006;11(4):193-202. doi:10.1016/j.cocis.2006.06.002

50. Lafuma A, Quéré D. Superhydrophobic states. *Nature Materials*. 2003;2(7):457-460. doi:10.1038/nmat924

51. Wong T-S, Kang SH, Tang SKY, et al. Bioinspired self-repairing slippery surfaces with pressure-stable omniphobicity. *Nature*. 2011;477(7365):443-447. doi:10.1038/nature10447

52. Wang L, McCarthy TJ. Covalently Attached Liquids: Instant Omniphobic Surfaces with Unprecedented Repellency. *Angewandte Chemie International Edition*. 2016;55(1):244-248. doi:https://doi.org/10.1002/anie.201509385

53. Kwon G, Kota ArunK, Li Y, Sohani A, Mabry JM, Tuteja A. On-Demand Separation of Oil-Water Mixtures. *Advanced Materials*. 2012;24(27):3666-3671. doi:10.1002/adma.201201364

54. Kota AK, Kwon G, Choi W, Mabry JM, Tuteja A. Hygro-responsive membranes for effective oil–water separation. *Nature Communications*. 2012;3(1):1025. doi:10.1038/ncomms2027

55. De Gennes P-G, Brochard-Wyart F, Quéré D. *Capillarity and Wetting Phenomena: Drops, Bubbles, Pearls, Waves*. Springer Science & Business Media; 2013.

56. Preston DJ, Lu Z, Song Y, et al. Heat Transfer Enhancement During Water and Hydrocarbon Condensation on Lubricant Infused Surfaces. *Scientific Reports*. 2018;8(1):540. doi:10.1038/s41598-017-18955-x

57. Rykaczewski K, Paxson AT, Staymates M, et al. Dropwise Condensation of Low Surface Tension Fluids on Omniphobic Surfaces. *Scientific Reports*. 2014;4(1):4158. doi:10.1038/srep04158

58. Mockenhaupt B, Ensikat H-J, Spaeth M, Barthlott W. Superhydrophobicity of Biological and Technical Surfaces under Moisture Condensation: Stability in Relation to Surface Structure. *Langmuir*. 2008;24(23):13591-13597. doi:10.1021/la802351h

59. Chu Z, Seeger S. Superamphiphobic surfaces. *Chem Soc Rev*. 2014;43(8):2784-2798. doi:10.1039/C3CS60415B

60. Yong J, Chen F, Yang Q, Huo J, Hou X. Superoleophobic surfaces. *Chem Soc Rev*. 2017;46(14):4168-4217. doi:10.1039/C6CS00751A

61. Ejaz Ahmed F, Lalia BS, Hilal N, Hashaikeh R. Underwater superoleophobic cellulose/electrospun PVDF–HFP membranes for efficient oil/water separation. *Desalination*. 2014;344:48-54. doi:10.1016/j.desal.2014.03.010

62. Liu M, Wang S, Wei Z, Song Y, Jiang L. Bioinspired Design of a Superoleophobic and Low Adhesive Water/Solid Interface. *Advanced Materials*. 2009;21(6):665-669. doi:10.1002/adma.200801782

63. Tuteja A, Choi W, Mabry JM, McKinley GH, Cohen RE. Robust omniphobic surfaces. *Proc Natl Acad Sci USA*. 2008;105(47):18200. doi:10.1073/pnas.0804872105

64. Kang SM, Kim SM, Kim HN, Kwak MK, Tahk DH, Suh KY. Robust superomniphobic surfaces with mushroom-like micropillar arrays. *Soft Matter*. 2012;8(33):8563-8568. doi:10.1039/C2SM25879J

65. Bielinski AR, Boban M, He Y, et al. Rational Design of Hyperbranched Nanowire Systems for Tunable Superomniphobic Surfaces Enabled by Atomic Layer Deposition. *ACS Nano*. 2017;11(1):478-489. doi:10.1021/acsnano.6b06463

66. Eral HB, 't Mannetje DJCM, Oh JM. Contact angle hysteresis: a review of fundamentals and applications. *Colloid and Polymer Science*. 2013;291(2):247-260. doi:10.1007/s00396-012-2796-6

67. Gao L, McCarthy TJ. Contact angle hysteresis explained. *Langmuir*. 2006;22(14):6234-6237.

68. Marmur A. Thermodynamic aspects of contact angle hysteresis. *Advances in Colloid and Interface Science*. 1994;50:121-141. doi:10.1016/0001-8686(94)80028-6

69. Drelich J. Guidelines to measurements of reproducible contact angles using a sessile-drop technique. *Surface Innovations*. 2013;1(4):248-254. doi:10.1680/si.13.00010

70. McHale JP, Garimella SV, Fisher TS, Powell GA. Pool Boiling Performance Comparison of Smooth and Sintered Copper Surfaces with and Without Carbon Nanotubes. *Nanoscale and Microscale Thermophysical Engineering*. 2011;15(3):133-150. doi:10.1080/15567265.2011.575918

71. Dorrer C, Rühe J. Wetting of Silicon Nanograss: From Superhydrophilic to Superhydrophobic Surfaces. *Advanced Materials*. 2008;20(1):159-163. doi:10.1002/adma.200701140

72. Shibuichi S, Yamamoto T, Onda T, Tsujii K. Super Water- and Oil-Repellent Surfaces Resulting from Fractal Structure. *Journal of Colloid and Interface Science*. 1998;208(1):287-294. doi:10.1006/jcis.1998.5813

73. Ahuja A, Taylor JA, Lifton V, et al. Nanonails: A Simple Geometrical Approach to Electrically Tunable Superlyophobic Surfaces. *Langmuir*. 2008;24(1):9-14. doi:10.1021/la702327z

74. Wang P, Zhang D, Sun S, Li T, Sun Y. Fabrication of Slippery Lubricant-Infused Porous Surface with High Underwater Transparency for the Control of Marine Biofouling. *ACS Appl Mater Interfaces*. 2017;9(1):972-982. doi:10.1021/acsami.6b09117

75. Rioboo R, Voué M, Vaillant A, De Coninck J. Drop Impact on Porous Superhydrophobic Polymer Surfaces. *Langmuir*. 2008;24(24):14074-14077. doi:10.1021/la802897g

76. Wenzel RN. RESISTANCE OF SOLID SURFACES TO WETTING BY WATER. *Ind Eng Chem*. 1936;28(8):988-994. doi:10.1021/ie50320a024

77. Cassie ABD, Baxter S. Wettability of porous surfaces. *Transactions of the Faraday society*. 1944;40:546-551.

78. McHale G. Cassie and Wenzel: Were They Really So Wrong? *Langmuir*. 2007;23(15):8200-8205. doi:10.1021/la7011167

79. Miljkovic N, Preston DJ, Enright R, Wang EN. Jumping-droplet electrostatic energy harvesting. *Appl Phys Lett*. 2014;105(1):013111. doi:10.1063/1.4886798

80. Cavalli A, Preston DJ, Tio E, et al. Electrically induced drop detachment and ejection. *Physics of fluids*. 2016;28(2):022101.

81. Mondal B, Mac Giolla Eain M, Xu Q, Egan VM, Punch J, Lyons AM. Design and Fabrication of a Hybrid Superhydrophobic–Hydrophilic Surface That Exhibits Stable Dropwise Condensation. *ACS Appl Mater Interfaces*. 2015;7(42):23575-23588. doi:10.1021/acsami.5b06759

82. Hoenig SH, Modak S, Chen Z, Kaviany M, Gilchrist JF, Bonner RW. Role of substrate thermal conductivity and vapor pressure in dropwise condensation. *Applied Thermal Engineering*. 2020;178:115529. doi:10.1016/j.applthermaleng.2020.115529

83. Cho HJ, Preston DJ, Zhu Y, Wang EN. Nanoengineered materials for liquid–vapour phase-change heat transfer. *Nature Reviews Materials*. 2016;2(2):16092. doi:10.1038/natrevmats.2016.92

84. Carey VP, Chen G, Grigoropoulos C, Kaviany M, Majumdar A. A review of heat transfer physics. *Nanoscale and Microscale Thermophysical Engineering*. 2008;12(1):1-60.

85. Glassford APM. Practical model for molecular contaminant deposition kinetics. *Journal of thermophysics and heat transfer*. 1992;6(4):656-664.

86. Chen L-H, Chen C-Y, Lee Y-L. Nucleation and growth of clusters in the process of vapor deposition. *Surface science*. 1999;429(1-3):150-160.

87. Fletcher NH. Size Effect in Heterogeneous Nucleation. *J Chem Phys*. 1958;29(3):572-576. doi:10.1063/1.1744540

88. Varanasi KK, Hsu M, Bhate N, Yang W, Deng T. Spatial control in the heterogeneous nucleation of water. *Applied Physics Letters*. 2009;95(9):094101.

89. Bonner III RW. Correlation for dropwise condensation heat transfer: Water, organic fluids, and inclination. *International Journal of Heat and Mass Transfer*. 2013;61:245-253.

90. Khalil K, Soto D, Farnham T, et al. Grafted Nanofilms Promote Dropwise Condensation of Low-Surface-Tension Fluids for High-Performance Heat Exchangers. *Joule*. 2019;3(5):1377-1388. doi:10.1016/j.joule.2019.04.009

91. Alwazzan M, Egab K, Peng B, Khan J, Li C. Condensation on hybrid-patterned copper tubes (I): Characterization of condensation heat transfer. *International Journal of Heat and Mass Transfer*. 2017;112:991-1004. doi:10.1016/j.ijheatmasstransfer.2017.05.039

92. Peng B, Ma X, Lan Z, Xu W, Wen R. Experimental investigation on steam condensation heat transfer enhancement with vertically patterned hydrophobic–hydrophilic hybrid surfaces. *International Journal of Heat and Mass Transfer*. 2015;83:27-38. doi:10.1016/j.ijheatmasstransfer.2014.11.069

93. Oh I, Cha H, Chen J, et al. Enhanced Condensation on Liquid-Infused Nanoporous Surfaces by Vibration-Assisted Droplet Sweeping. *ACS Nano*. 2020;14(10):13367-13379. doi:10.1021/acsnano.0c05223

94. Zhang L, Shi J, Xu B, Chen Z. Experimental Study on Distribution Characteristics of Condensate Droplets Under Ultrasonic Vibration. *Microgravity Science and Technology*. 2018;30(6):737-746. doi:10.1007/s12217-018-9616-7

95. Boreyko JB, Collier CP. Dewetting Transitions on Superhydrophobic Surfaces: When Are Wenzel Drops Reversible? *J Phys Chem C*. 2013;117(35):18084-18090. doi:10.1021/jp4053083

96. Chen R, Jiao L, Zhu X, et al. Cassie-to-Wenzel transition of droplet on the superhydrophobic surface caused by light induced evaporation. *Applied Thermal Engineering*. 2018;144:945-959. doi:10.1016/j.applthermaleng.2018.09.011

97. Preston DJ, Song Y, Lu Z, Antao DS, Wang EN. Design of lubricant infused surfaces. *ACS applied materials & interfaces*. 2017;9(48):42383-42392.

98. Sett S, Sokalski P, Boyina K, et al. Stable Dropwise Condensation of Ethanol and Hexane on Rationally Designed Ultrascalable Nanostructured Lubricant-Infused Surfaces. *Nano Lett*. 2019;19(8):5287-5296. doi:10.1021/acs.nanolett.9b01754

99. Mukherjee R, Berrier AS, Murphy KR, Vieitez JR, Boreyko JB. How Surface Orientation Affects Jumping-Droplet Condensation. *Joule*. 2019;3(5):1360-1376. doi:10.1016/j.joule.2019.03.004

100. Mulroe MD, Srijanto BR, Ahmadi SF, Collier CP, Boreyko JB. Tuning Superhydrophobic Nanostructures To Enhance Jumping-Droplet Condensation. *ACS Nano*. 2017;11(8):8499-8510. doi:10.1021/acsnano.7b04481

101. Tong LS. Heat-transfer mechanisms in nucleate and film boiling. *Nuclear Engineering and Design*. 1972;21(1):1-25. doi:10.1016/0029-5493(72)90082-9

102. Bankoff SG. The prediction of surface temperatures at incipient boiling. In: *Chem. Eng. Prog., Symp. Ser*. Vol 55. ; 1959:87.

103. Attinger D, Frankiewicz C, Betz AR, et al. Surface engineering for phase change heat transfer: A review. *MRS Energy & Sustainability*. 2014;1:E4. doi:10.1557/mre.2014.9

104. Qi Y, Klausner JF. Comparison of Nucleation Site Density for Pool Boiling and Gas Nucleation. *Journal of Heat Transfer*. 2005;128(1):13-20. doi:10.1115/1.2130399

105. Betz AR, Jenkins J, Kim C-J "CJ", Attinger D. Boiling heat transfer on superhydrophilic, superhydrophobic, and superbiphilic surfaces. *International Journal of Heat and Mass Transfer*. 2013;57(2):733-741. doi:10.1016/j.ijheatmasstransfer.2012.10.080

106. Wang CH, Dhir VK. Effect of Surface Wettability on Active Nucleation Site Density During Pool Boiling of Water on a Vertical Surface. *Journal of Heat Transfer*. 1993;115(3):659-669. doi:10.1115/1.2910737

107. Bui TD, Dhir VK. Transition Boiling Heat Transfer on a Vertical Surface. *Journal of Heat Transfer*. 1985;107(4):756-763. doi:10.1115/1.3247501

108. Kim DE, Park SC, Yu DI, Kim MH, Ahn HS. Enhanced critical heat flux by capillary driven liquid flow on the well-designed surface. *Appl Phys Lett*. 2015;107(2):023903. doi:10.1063/1.4926971

109. Ahn HS, Lee C, Kim J, Kim MH. The effect of capillary wicking action of micro/nano structures on pool boiling critical heat flux. *International Journal of Heat and Mass Transfer*. 2012;55(1):89-92. doi:10.1016/j.ijheatmasstransfer.2011.08.044

110. Kim HD, Kim MH. Effect of nanoparticle deposition on capillary wicking that influences the critical heat flux in nanofluids. *Appl Phys Lett*. 2007;91(1):014104. doi:10.1063/1.2754644

111. Iragorry J, Tao Y-X, Jia S. Review Article: A Critical Review of Properties and Models for Frost Formation Analysis. *null*. 2004;10(4):393-420. doi:10.1080/10789669.2004.10391111

112. Rashid T, Khawaja HA, Edvardsen K. Review of marine icing and anti-/de-icing systems. *null*. 2016;15(2):79-87. doi:10.1080/20464177.2016.1216734

113. Piucco RO, Hermes CJL, Melo C, Barbosa JR. A study of frost nucleation on flat surfaces. *Experimental Thermal and Fluid Science*. 2008;32(8):1710-1715. doi:10.1016/j.expthermflusci.2008.06.004

114. Shen Y, Wu X, Tao J, Zhu C, Lai Y, Chen Z. Icephobic materials: Fundamentals, performance evaluation, and applications. *Progress in Materials Science*. 2019;103:509-557. doi:10.1016/j.pmatsci.2019.03.004

115. Kreder MJ, Alvarenga J, Kim P, Aizenberg J. Design of anti-icing surfaces: smooth, textured or slippery? *Nature Reviews Materials*. 2016;1(1):15003. doi:10.1038/natrevmats.2015.3

116. Kulinich SA, Farhadi S, Nose K, Du XW. Superhydrophobic surfaces: are they really ice-repellent? *Langmuir*. 2011;27(1):25-29.

117. Du N, Liu XY, Hew CL. Ice Nucleation Inhibition: MECHANISM OF ANTIFREEZE BY ANTIFREEZE PROTEIN. *Journal of Biological Chemistry*. 2003;278(38):36000-36004. doi:10.1074/jbc.M305222200

118. Knight CA, De Vries AL, Oolman LD. Fish antifreeze protein and the freezing and recrystallization of ice. *Nature*. 1984;308(5956):295-296.

119. Devries AL. Glycoproteins as biological antifreeze agents in Antarctic fishes. *Science*. 1971;172(3988):1152-1155.

120. Graether SP, Kuiper MJ, Gagné SM, et al. β-Helix structure and ice-binding properties of a hyperactive antifreeze protein from an insect. *Nature*. 2000;406(6793):325-328. doi:10.1038/35018610

121. Knight CA, Cheng CC, DeVries AL. Adsorption of alpha-helical antifreeze peptides on specific ice crystal surface planes. *Biophysical journal*. 1991;59(2):409-418.

122. Guo Q, He Z, Jin Y, et al. Tuning Ice Nucleation and Propagation with Counterions on Multilayer Hydrogels. *Langmuir*. 2018;34(40):11986-11991. doi:10.1021/acs.langmuir.8b02106

123. He Z, Wu C, Hua M, et al. Bioinspired Multifunctional Anti-icing Hydrogel. *Matter*. 2020;2(3):723-734. doi:10.1016/j.matt.2019.12.017

124. Jin Y, Wu C, Yang Y, Wu J, He Z, Wang J. Inhibiting Condensation Freezing on Patterned Polyelectrolyte Coatings. *ACS nano*. 2020;14(4):5000-5007.

125. Zhuo Y, Xiao S, Håkonsen V, He J, Zhang Z. Anti-icing Ionogel Surfaces: Inhibiting Ice Nucleation, Growth, and Adhesion. *ACS Materials Letters*. 2020;2(6):616-623.

126. Kehlhofer R. *Combined-Cycle Gas & Steam Turbine Power Plants*. PennWell; 2009. https://books.google.com/books?id=OmnOG7vWfuQC

127. Seader JD, Henley EJ, Roper DK. *Separation Process Principles*. Vol 25. Wiley New York; 1998.

128. Khawaji AD, Kutubkhanah IK, Wie J-M. Advances in seawater desalination technologies. *Desalination*. 2008;221(1-3):47-69.

129. Pérez-Lombard L, Ortiz J, Pout C. A review on buildings energy consumption information. *Energy and buildings*. 2008;40(3):394-398.

130. Ahlers M, Buck-Emden A, Bart H-J. Is dropwise condensation feasible? A review on surface modifications for continuous dropwise condensation and a profitability analysis. *Journal of advanced research*. 2019;16:1-13.

131. Kim S, Kim KJ. Dropwise Condensation Modeling Suitable for Superhydrophobic Surfaces. *Journal of Heat Transfer*. 2011;133(081502). doi:10.1115/1.4003742

132. Paxson AT, Yagüe JL, Gleason KK, Varanasi KK. Stable Dropwise Condensation for Enhancing Heat Transfer via the Initiated Chemical Vapor Deposition (iCVD) of Grafted Polymer Films. *Advanced Materials*. 2014;26(3):418-423. doi:10.1002/adma.201303065

133. Rose Jw. On the mechanism of dropwise condensation. *International Journal of Heat and Mass Transfer*. 1967;10(6):755-762.

134. Dai X, Sun N, Nielsen SO, et al. Hydrophilic directional slippery rough surfaces for water harvesting. *Science advances*. 2018;4(3):eaaq0919.

135. Xiao R, Miljkovic N, Enright R, Wang EN. Immersion Condensation on Oil-Infused Heterogeneous Surfaces for Enhanced Heat Transfer. *Scientific Reports*. 2013;3(1):1988. doi:10.1038/srep01988

136. Tsuchiya H, Tenjimbayashi M, Moriya T, et al. Liquid-infused smooth surface for improved condensation heat transfer. *Langmuir*. 2017;33(36):8950-8960.

137. Günay AA, Sett S, Ge Q, Zhang T, Miljkovic N. Cloaking Dynamics on Lubricant-Infused Surfaces. *Advanced Materials Interfaces*. 2020;7(19):2000983. doi:10.1002/admi.202000983

138. Guo L, Tang GH, Kumar S. Dynamic Wettability on the Lubricant-Impregnated Surface: From Nucleation to Growth and Coalescence. *ACS Appl Mater Interfaces*. 2020;12(23):26555-26565. doi:10.1021/acsami.0c03018

139. Ge Q, Raza A, Li H, Sett S, Miljkovic N, Zhang T. Condensation of Satellite Droplets on Lubricant-Cloaked Droplets. *ACS Appl Mater Interfaces*. 2020;12(19):22246-22255. doi:10.1021/acsami.9b22417

140. Sett S, Yan X, Barac G, Bolton LW, Miljkovic N. Lubricant-infused surfaces for low-surface-tension fluids: promise versus reality. *ACS applied materials & interfaces*. 2017;9(41):36400-36408.

141. Foulkes T, Sett S, Sokalski P, Oh J, Miljkovic N. Fundamental limits of jumping droplet heat transfer. *Appl Phys Lett*. 2020;116(9):093701. doi:10.1063/1.5141744

142. Niu D, Guo L, Hu HW, Tang GH. Dropwise condensation heat transfer model considering the liquid-solid interfacial thermal resistance. *International Journal of Heat and Mass Transfer*. 2017;112:333-342. doi:10.1016/j.ijheatmasstransfer.2017.04.061

143. Rose JW. Proc. Inst. Mech. Eng. Part A-J. *Power Energy*. 2002;216:115.

144. Liu X, Cheng P. Dropwise condensation theory revisited Part II. Droplet nucleation density and condensation heat flux. *International Journal of Heat and Mass Transfer*. 2015;83:842-849. doi:10.1016/j.ijheatmasstransfer.2014.11.008

145. Furmidge CGL. Studies at phase interfaces. I. The sliding of liquid drops on solid surfaces and a theory for spray retention. *Journal of Colloid Science*. 1962;17(4):309-324. doi:10.1016/0095-8522(62)90011-9

146. Barriet D, Lee TR. Fluorinated self-assembled monolayers: composition, structure and interfacial properties. *Current opinion in colloid & interface science*. 2003;8(3):236-242.

147. Cheng DF, Urata C, Yagihashi M, Hozumi A. A Statically Oleophilic but Dynamically Oleophobic Smooth Nonperfluorinated Surface. *Angewandte Chemie International Edition*. 2012;51(12):2956-2959. doi:10.1002/anie.201108800

148. Golovin K, Kobaku SP, Lee DH, DiLoreto ET, Mabry JM, Tuteja A. Designing durable icephobic surfaces. *Science advances*. 2016;2(3):e1501496.

149. Shanks HR, Maycock PD, Sidles PH, Danielson GC. Thermal Conductivity of Silicon from 300 to 1400\ifmmode^\circ\else\textdegree\fi{}K. *Phys Rev*. 1963;130(5):1743-1748. doi:10.1103/PhysRev.130.1743

150. Ma X-H, Zhou X-D, Lan Z, LI Y-M, Zhang Y. Condensation heat transfer enhancement in the presence of non-condensable gas using the interfacial effect of dropwise condensation. *International Journal of Heat and Mass Transfer*. 2008;51(7):1728-1737. doi:10.1016/j.ijheatmasstransfer.2007.07.021

151. Jackson JD, An P, Ahmadinejad M. Heat transfer from a steam/air mixture to a water-cooled condensing plate. In: *International Heat Transfer Conference Digital Library*. Begel House Inc.; 2002.

152. Ganzevles FLA, Van Der Geld CWM. Temperatures and the condensate heat resistance in dropwise condensation of multicomponent mixtures with inert gases. *International journal of heat and mass transfer*. 2002;45(15):3233-3243.

153. Abdulhadi M. Estimation of air traces in steam-air mixtures subjected to dropwise condensation. *International communications in heat and mass transfer*. 1987;14(3):347-351.

154. Reisbig RL. Diffusion-controlled condensation from a two-species mixture. *High Temperatures High Pressures (Print)*. 1992;24(2):231-240.

155. SUDARAMAN T, TG S. HEAT TRANSFER DURING DROPWISE CONDENSATION OF STEAM IN THE PRESENCE OF NON-CONDENSABLE GASES. EFFECTS OF GEOMETRICAL SHAPE OF THE SURFACE REVERSAL OF COOLING WATER FLOW AND ORIENTATION. Published online 1976.

156. Citakoglu E, Rose JW. Dropwise condensation—some factors influencing the validity of heat-transfer measurements. *International Journal of Heat and Mass Transfer*. 1968;11(3):523-537.

157. Ma X-H, Zhou X-D, Lan Z, Yi-Ming LI, Zhang Y. Condensation heat transfer enhancement in the presence of non-condensable gas using the interfacial effect of dropwise condensation. *International Journal of Heat and Mass Transfer*. 2008;51(7-8):1728-1737.

158. Ma X-H, Zhou X-D, Lan Z, LI Y-M, Zhang Y. Condensation heat transfer enhancement in the presence of non-condensable gas using the interfacial effect of dropwise condensation. *International Journal of Heat and Mass Transfer*. 2008;51(7):1728-1737. doi:10.1016/j.ijheatmasstransfer.2007.07.021

159. Abu-Orabi M. Modeling of heat transfer in dropwise condensation. *International journal of heat and mass transfer*. 1998;41(1):81-87.

160. Carey VP. *Liquid-Vapor Phase-Change Phenomena: An Introduction to the Thermophysics of Vaporization and Condensation Processes in Heat Transfer Equipment*. CRC Press; 2020.

161. Miljkovic N, Enright R, Nam Y, et al. Jumping-droplet-enhanced condensation on scalable superhydrophobic nanostructured surfaces. *Nano letters*. 2013;13(1):179-187.

162. Preston DJ, Lu Z, Song Y, et al. Heat transfer enhancement during water and hydrocarbon condensation on lubricant infused surfaces. *Scientific reports*. 2018;8(1):1-9.

163. Rykaczewski K, Paxson AT, Staymates M, et al. Dropwise condensation of low surface tension fluids on omniphobic surfaces. *Scientific reports*. 2014;4:4158.

164. Outlook SAE. World energy outlook special report. *International Energy Agency*. 2015;135.

165. Outlook AE. Energy information administration. *Department of Energy*. 2020;2020(1).

166. Tanuma T. 1 - Introduction to steam turbines for power plants. In: Tanuma T, ed. *Advances in Steam Turbines for Modern Power Plants*. Woodhead Publishing; 2017:3-9. doi:10.1016/B978-0-08-100314-5.00001-4

167. Edenhofer O. *Climate Change 2014: Mitigation of Climate Change*. Vol 3. Cambridge University Press; 2015.

168. Rogalev N, Prokhorov V, Rogalev A, Komarov I, Kindra V. Steam boilers' advanced constructive solutions for the ultra-supercritical power plants. *International Journal of Applied Engineering Research*. 2016;11(18):9297-9306.

169. Basu S, Debnath AK. Chapter 13 - Advanced Ultrasupercritical Thermal Power Plant and Associated Auxiliaries. In: Basu S, Debnath AK, eds. *Power Plant Instrumentation and*

Control Handbook (Second Edition). Academic Press; 2019:893-988. doi:10.1016/B978-0-12-819504-8.00013-5

170. Xu J, Sun E, Li M, Liu H, Zhu B. Key issues and solution strategies for supercritical carbon dioxide coal fired power plant. *Energy*. 2018;157:227-246. doi:10.1016/j.energy.2018.05.162

171. Yan J, Smith III LD, Karoutas Z. Departure from nucleate boiling modeling development for PWR fuel. In: *International Conference on Nuclear Engineering*. Vol 55805. American Society of Mechanical Engineers; 2013:V003T10A016.

172. Van Houten R. *Fuel Rod Failure as a Consequence of Departure from Nucleate Boiling or Dryout*. Nuclear Regulatory Commission; 1979.

173. Petti DA, Martinson ZR, Hobbins RR, et al. *Power Burst Facility (PBF) Severe Fuel Damage Test 1-4 Test Results Report*. Nuclear Regulatory Commission, Washington, DC (USA). Div. of Systems …; 1989.

174. Dasgupta A, Chandraker DK, Vijayan PK. SCADOP: Phenomenological modeling of dryout in nuclear fuel rod bundles. *Nuclear Engineering and Design*. 2015;293:127-137.

175. Clifford I, Pecchia M, Mukin R, Cozzo C, Ferroukhi H, Gorzel A. Studies on the effects of local power peaking on heat transfer under dryout conditions in BWRs. *Annals of Nuclear Energy*. 2019;130:440-451.

176. Zhang Y, Zhao J, Wei J, Xue Y. Nucleate pool boiling heat transfer on a micro-pin-finned surface in short-term microgravity. *Heat Transfer Engineering*. 2017;38(6):594-610.

177. Nazari A, Saedodin S. Porous anodic alumina coating for optimisation of pool-boiling performance. *Surface Engineering*. 2017;33(10):753-759.

178. Jo HS, Kim M-W, Kim K, et al. Effects of capillarity on pool boiling using nano-textured surfaces through electrosprayed BiVO4 nano-pillars. *Chemical Engineering Science*. 2017;171:360-367.

179. Jo HS, An S, Park HG, et al. Enhancement of critical heat flux and superheat through controlled wettability of cuprous-oxide fractal-like nanotextured surfaces in pool boiling. *International Journal of Heat and Mass Transfer*. 2017;107:105-111.

180. Surtaev AS, Pavlenko AN, Kuznetsov DV, et al. Heat transfer and crisis phenomena at pool boiling of liquid nitrogen on the surfaces with capillary-porous coatings. *International Journal of Heat and Mass Transfer*. 2017;108:146-155.

181. Gheitaghy AM, Saffari H, Mohebbi M. Investigation pool boiling heat transfer in U-shaped mesochannel with electrodeposited porous coating. *Experimental Thermal and Fluid Science*. 2016;76:87-97.

182. Kruse CM, Anderson T, Wilson C, et al. Enhanced pool-boiling heat transfer and critical heat flux on femtosecond laser processed stainless steel surfaces. *International journal of heat and mass transfer*. 2015;82:109-116.

183. Deng D, Wan W, Feng J, Huang Q, Qin Y, Xie Y. Comparative experimental study on pool boiling performance of porous coating and solid structures with reentrant channels. *Applied Thermal Engineering*. 2016;107:420-430.

184. Jo HS, Lee J-G, An S, et al. Supersonically sprayed, triangular copper lines for pool boiling enhancement. *International Journal of Heat and Mass Transfer*. 2017;113:210-216.

185. Mori S, Aznam SM, Okuyama K. Enhancement of the critical heat flux in saturated pool boiling of water by nanoparticle-coating and a honeycomb porous plate. *International Journal of Heat and Mass Transfer*. 2015;80:1-6.

186. Mani D, Sivan S, Ali HM, Ganesan UK. Investigation to Improve the Pool Boiling Heat Transfer Characteristics Using Laser-Textured Copper-Grooved Surfaces. Li C, ed. *International Journal of Photoenergy*. 2020;2020:3846157. doi:10.1155/2020/3846157

187. Zakšek P, Zupančič M, Gregorčič P, Golobič I. Investigation of Nucleate Pool Boiling of Saturated Pure Liquids and Ethanol-Water Mixtures on Smooth and Laser-Textured Surfaces. *null*. 2020;24(1):29-42. doi:10.1080/15567265.2019.1689590

188. Sahu RP, Sinha-Ray S, Sinha-Ray S, Yarin AL. Pool boiling on nano-textured surfaces comprised of electrically-assisted supersonically solution-blown, copper-plated nanofibers: Experiments and theory. *International Journal of Heat and Mass Transfer*. 2015;87:521-535. doi:10.1016/j.ijheatmasstransfer.2015.04.009

189. Hendricks TJ, Krishnan S, Choi C, Chang C-H, Paul B. Enhancement of pool-boiling heat transfer using nanostructured surfaces on aluminum and copper. *International Journal of Heat and Mass Transfer*. 2010;53(15):3357-3365. doi:10.1016/j.ijheatmasstransfer.2010.02.025

190. Jun S, Sinha-Ray S, Yarin AL. Pool boiling on nano-textured surfaces. *International Journal of Heat and Mass Transfer*. 2013;62:99-111. doi:10.1016/j.ijheatmasstransfer.2013.02.046

191. Kim H, Park Y, Buongiorno J. Measurement of wetted area fraction in subcooled pool boiling of water using infrared thermography. *Nuclear Engineering and Design*. 2013;264:103-110. doi:10.1016/j.nucengdes.2013.07.002

192. El-Genk MS, Ali AF. Enhanced nucleate boiling on copper micro-porous surfaces. *International Journal of Multiphase Flow*. 2010;36(10):780-792. doi:10.1016/j.ijmultiphaseflow.2010.06.003

193. Voglar J, Gregorčič P, Zupančič M, Golobič I. Boiling performance on surfaces with capillary-length-spaced one- and two-dimensional laser-textured patterns. *International*

Journal of Heat and Mass Transfer. 2018;127:1188-1196. doi:10.1016/j.ijheatmasstransfer.2018.07.056

194. MacNamara RJ, Lupton TL, Lupoi R, Robinson AJ. Enhanced nucleate pool boiling on copper-diamond textured surfaces. *Applied Thermal Engineering*. 2019;162:114145. doi:10.1016/j.applthermaleng.2019.114145

195. NUCLEATE BOILING HEAT TRANSFER PERFORMANCE OF LASER TEXTURED COPPER SURFACES. *Journal of Enhanced Heat Transfer*. 2019;26(6):597-618.

196. Berenson PJ. Experiments on pool-boiling heat transfer. *International Journal of Heat and Mass Transfer*. 1962;5(10):985-999. doi:10.1016/0017-9310(62)90079-0

197. WEBB RL. The Evolution of Enhanced Surface Geometries for Nucleate Boiling. *null*. 1981;2(3-4):46-69. doi:10.1080/01457638108962760

198. Chu K-H, Enright R, Wang EN. Structured surfaces for enhanced pool boiling heat transfer. *Appl Phys Lett*. 2012;100(24):241603. doi:10.1063/1.4724190

199. Son HH, Seo GH, Jeong U, Shin DY, Kim SJ. Capillary wicking effect of a Cr-sputtered superhydrophilic surface on enhancement of pool boiling critical heat flux. *International Journal of Heat and Mass Transfer*. 2017;113:115-128. doi:10.1016/j.ijheatmasstransfer.2017.05.055

200. Kwark SM, Kumar R, Moreno G, Yoo J, You SM. Pool boiling characteristics of low concentration nanofluids. *International Journal of Heat and Mass Transfer*. 2010;53(5):972-981. doi:10.1016/j.ijheatmasstransfer.2009.11.018

201. Kim SJ, Bang IC, Buongiorno J, Hu LW. Surface wettability change during pool boiling of nanofluids and its effect on critical heat flux. *International Journal of Heat and Mass Transfer*. 2007;50(19):4105-4116. doi:10.1016/j.ijheatmasstransfer.2007.02.002

202. Barber J, Brutin D, Tadrist L. A review on boiling heat transfer enhancement with nanofluids. *Nanoscale Research Letters*. 2011;6(1):280. doi:10.1186/1556-276X-6-280

203. Amiri A, Shanbedi M, Amiri H, et al. Pool boiling heat transfer of CNT/water nanofluids. *Applied Thermal Engineering*. 2014;71(1):450-459. doi:10.1016/j.applthermaleng.2014.06.064

204. Murshed SMS, Nieto de Castro CA, Lourenço MJV, Lopes MLM, Santos FJV. A review of boiling and convective heat transfer with nanofluids. *Renewable and Sustainable Energy Reviews*. 2011;15(5):2342-2354. doi:10.1016/j.rser.2011.02.016

205. You SM, Kim JH, Kim KH. Effect of nanoparticles on critical heat flux of water in pool boiling heat transfer. *Applied physics letters*. 2003;83(16):3374-3376.

206. Liang G, Mudawar I. Review of pool boiling enhancement with additives and nanofluids. *International Journal of Heat and Mass Transfer*. 2018;124:423-453. doi:10.1016/j.ijheatmasstransfer.2018.03.046

207. Kim SJ, Bang IC, Buongiorno J, Hu LW. Effects of nanoparticle deposition on surface wettability influencing boiling heat transfer in nanofluids. *Applied Physics Letters*. 2006;89(15):153107.

208. Wen D, Ding Y. Experimental investigation into the pool boiling heat transfer of aqueous based γ-alumina nanofluids. *Journal of Nanoparticle Research*. 2005;7(2):265-274. doi:10.1007/s11051-005-3478-9

209. Phan HT, Caney N, Marty P, Colasson S, Gavillet J. Surface coating with nanofluids: the effects on pool boiling heat transfer. *Nanoscale and Microscale Thermophysical Engineering*. 2010;14(4):229-244.

210. Kim SJ, Bang IC, Buongiorno J, Hu LW. Surface wettability change during pool boiling of nanofluids and its effect on critical heat flux. *International Journal of Heat and Mass Transfer*. 2007;50(19-20):4105-4116.

211. Sarafraz MM, Hormozi F, Silakhori M, Peyghambarzadeh SM. On the fouling formation of functionalized and non-functionalized carbon nanotube nano-fluids under pool boiling condition. *Applied Thermal Engineering*. 2016;95:433-444. doi:10.1016/j.applthermaleng.2015.11.071

212. Vafaei S, Borca-Tasciuc T. Role of nanoparticles on nanofluid boiling phenomenon: Nanoparticle deposition. *Chemical Engineering Research and Design*. 2014;92(5):842-856. doi:10.1016/j.cherd.2013.08.007

213. Sarafraz MM, Hormozi F. Scale formation and subcooled flow boiling heat transfer of CuO–water nanofluid inside the vertical annulus. *Experimental Thermal and Fluid Science*. 2014;52:205-214. doi:10.1016/j.expthermflusci.2013.09.012

214. Quéré D. Wetting and Roughness. *Annu Rev Mater Res*. 2008;38(1):71-99. doi:10.1146/annurev.matsci.38.060407.132434

215. Kim JS, Girard A, Jun S, Lee J, You SM. Effect of surface roughness on pool boiling heat transfer of water on hydrophobic surfaces. *International Journal of Heat and Mass Transfer*. 2018;118:802-811.

216. Surtaev AS, Serdyukov VS, Safonov AI. Enhancement of boiling heat transfer on hydrophobic fluoropolymer coatings. *Interfacial Phenomena and Heat Transfer*. 2018;6(3).

217. Chandekar A, Sengupta SK, Whitten JE. Thermal stability of thiol and silane monolayers: A comparative study. *Applied Surface Science*. 2010;256(9):2742-2749.

218. Gupta R, Shinde S, Yella A, Subramaniam C, Saha SK. Thermomechanical characterisations of PTFE, PEEK, PEKK as encapsulation materials for medium temperature solar applications. *Energy*. 2020;194:116921. doi:10.1016/j.energy.2020.116921

219. Sarafraz MM, Hormozi F, Kamalgharibi M. Sedimentation and convective boiling heat transfer of CuO-water/ethylene glycol nanofluids. *Heat and Mass Transfer*. 2014;50(9):1237-1249. doi:10.1007/s00231-014-1336-y

220. Dash S, Rapoport L, Varanasi KK. Crystallization-Induced Fouling during Boiling: Formation Mechanisms to Mitigation Approaches. *Langmuir*. 2018;34(3):782-788. doi:10.1021/acs.langmuir.7b02936

221. Hibiki T, Ishii M. Active nucleation site density in boiling systems. *International Journal of Heat and Mass Transfer*. 2003;46(14):2587-2601. doi:10.1016/S0017-9310(03)00031-0

222. Bowers A, Bunn J, Kim M. Efficient Methods to Calculate Partial Sphere Surface Areas for a Higher Resolution Finite Volume Method for Diffusion-Reaction Systems in Biological Modeling. *Mathematical and Computational Applications*. 2020;25(1):2.

223. Liaw SP, Dhir VK. Void Fraction Measurements During Saturated Pool Boiling of Water on Partially Wetted Vertical Surfaces. *Journal of Heat Transfer*. 1989;111(3):731-738. doi:10.1115/1.3250744

224. Shoji M, Yi XZ. Study of Contact Angle Hysteresis : In Relation to Boiling Surface Wettability. *JSME International Journal Series B*. 1994;37(3):560-567. doi:10.1299/jsmeb.37.560

225. Stephan P, Hammer J. A new model for nucleate boiling heat transfer. *Heat and Mass Transfer*. 1994;30(2):119-125. doi:10.1007/BF00715018

226. Forster HK, Zuber N. Dynamics of vapor bubbles and boiling heat transfer. *AIChE Journal*. 1955;1(4):531-535. doi:10.1002/aic.690010425

227. Cooper MG. The microlayer and bubble growth in nucleate pool boiling. *International Journal of Heat and Mass Transfer*. 1969;12(8):915-933. doi:10.1016/0017-9310(69)90155-0

228. Mukherjee A, Kandlikar SG. Numerical study of single bubbles with dynamic contact angle during nucleate pool boiling. *International Journal of Heat and Mass Transfer*. 2007;50(1):127-138. doi:10.1016/j.ijheatmasstransfer.2006.06.037

229. Dekempeneer E, Van Acker K, Vercammen K, et al. Abrasion resistant low friction diamond-like multilayers. *Surface and Coatings Technology*. 2001;142-144:669-673. doi:10.1016/S0257-8972(01)01141-0

230. Banerji A, Bhowmick S, Alpas AT. High temperature tribological behavior of W containing diamond-like carbon (DLC) coating against titanium alloys. *Surface and Coatings Technology*. 2014;241:93-104. doi:10.1016/j.surfcoat.2013.10.075

231. Gharam AA, Lukitsch MJ, Balogh MP, Alpas AT. High temperature tribological behaviour of carbon based (B4C and DLC) coatings in sliding contact with aluminum. *Thin Solid Films*. 2010;519(5):1611-1617. doi:10.1016/j.tsf.2010.07.074

232. Yang B, Zheng Y, Zhang B, Wei L, Zhang J. The high-temperature tribological properties of Si-DLC films. *Surface and Interface Analysis*. 2012;44(13):1601-1605. doi:10.1002/sia.5094

233. Shamsa M, Liu WL, Balandin AA, Casiraghi C, Milne WI, Ferrari AC. Thermal conductivity of diamond-like carbon films. *Appl Phys Lett*. 2006;89(16):161921. doi:10.1063/1.2362601

234. Kimock FM, Knapp BJ. Commercial applications of ion beam deposited diamond-like carbon (DLC) coatings. *Surface and Coatings Technology*. 1993;56(3):273-279. doi:10.1016/0257-8972(93)90261-L

235. Lifshitz Y. Hydrogen-free amorphous carbon films: correlation between growth conditions and properties. *Diamond and Related Materials*. 1996;5(3):388-400. doi:10.1016/0925-9635(95)00445-9

236. Pappas DL, Saenger KL, Bruley J, et al. Pulsed laser deposition of diamond-like carbon films. *Journal of Applied Physics*. 1992;71(11):5675-5684. doi:10.1063/1.350501

237. Taherian F, Marcon V, van der Vegt NFA, Leroy F. What Is the Contact Angle of Water on Graphene? *Langmuir*. 2013;29(5):1457-1465. doi:10.1021/la304645w

238. Ostrovskaya L, Perevertailo V, Ralchenko V, Dementjev A, Loginova O. Wettability and surface energy of oxidized and hydrogen plasma-treated diamond films. *Diamond and Related Materials*. 2002;11(3):845-850. doi:10.1016/S0925-9635(01)00636-7

239. Oliver WC, Pharr GM. Measurement of hardness and elastic modulus by instrumented indentation: Advances in understanding and refinements to methodology. *Journal of materials research*. 2004;19(1):3-20.

240. Koch T, Seidler S. Correlations Between Indentation Hardness and Yield Stress in Thermoplastic Polymers. *Strain*. 2009;45(1):26-33. doi:10.1111/j.1475-1305.2008.00468.x

241. Lu M-C, Huang C-H, Huang C-T, Chen Y-C. A modified hydrodynamic model for pool boiling CHF considering the effects of heater size and nucleation site density. *International Journal of Thermal Sciences*. 2015;91:133-141. doi:10.1016/j.ijthermalsci.2015.01.011

242. Takata Y, Hidaka S, Masuda M, Ito T. Pool boiling on a superhydrophilic surface. *International Journal of Energy Research*. 2003;27(2):111-119. doi:10.1002/er.861

243. Dhir VK, Liaw SP. Framework for a unified model for nucleate and transition pool boiling. Published online 1989.

244. Chang Y-S. Performance analysis of frostless heat exchanger by spreading antifreeze solution on heat exchanger surface. *Journal of Thermal Science and Technology*. 2011;6(1):123-131.

245. Boluk Y. Adhesion of freezing precipitates to aircraft surfaces. Published online 1996.

246. Sayward JM. *Seeking Low Ice Adhesion*. Vol 79. The Laboratory; 1979.

247. Emery AF, Siegel BL. Experimental measurements of the effects of frost formation on heat exchanger performance. In: *Heat and Mass Transfer in Frost and Ice, Packed Beds, and Environmental Discharges*. ; 1990.

248. Huang L, Liu Z, Liu Y, Gou Y, Wang J. Experimental study on frost release on fin-and-tube heat exchangers by use of a novel anti-frosting paint. *Experimental Thermal and Fluid Science*. 2009;33(7):1049-1054.

249. Wilson PW, Heneghan AF, Haymet ADJ. Ice nucleation in nature: supercooling point (SCP) measurements and the role of heterogeneous nucleation. *Cryobiology*. 2003;46(1):88-98. doi:10.1016/S0011-2240(02)00182-7

250. Cooper SJ, Nicholson CE, Liu J. A simple classical model for predicting onset crystallization temperatures on curved substrates and its implications for phase transitions in confined volumes. *The Journal of chemical physics*. 2008;129(12):124715.

251. Xu D, Johnson WL. Geometric model for the critical-value problem of nucleation phenomena containing the size effect of nucleating agent. *Physical Review B*. 2005;72(5):052101.

252. Cao L, Jones AK, Sikka VK, Wu J, Gao D. Anti-icing superhydrophobic coatings. *Langmuir*. 2009;25(21):12444-12448.

253. Kim P, Wong T-S, Alvarenga J, Kreder MJ, Adorno-Martinez WE, Aizenberg J. Liquid-infused nanostructured surfaces with extreme anti-ice and anti-frost performance. *ACS nano*. 2012;6(8):6569-6577.

254. Coady MJ, Wood M, Wallace GQ, et al. Icephobic Behavior of UV-Cured Polymer Networks Incorporated into Slippery Lubricant-Infused Porous Surfaces: Improving SLIPS Durability. *ACS Appl Mater Interfaces*. 2018;10(3):2890-2896. doi:10.1021/acsami.7b14433

255. Feeney RE, Burcham TS, Yeh Y. Antifreeze glycoproteins from polar fish blood. *Annual review of biophysics and biophysical chemistry*. 1986;15(1):59-78.

256. Zachariassen KE, Kristiansen E. Ice nucleation and antinucleation in nature. *Cryobiology*. 2000;41(4):257-279.

257. Liou Y-C, Tocilj A, Davies PL, Jia Z. Mimicry of ice structure by surface hydroxyls and water of a β-helix antifreeze protein. *Nature*. 2000;406(6793):322-324. doi:10.1038/35018604

258. Zhang W, Laursen RA. Structure-function relationships in a type I antifreeze polypeptide the role of threonine methyl and hydroxyl groups in antifreeze activity. *Journal of Biological Chemistry*. 1998;273(52):34806-34812.

259. Esser-Kahn AP, Trang V, Francis MB. Incorporation of Antifreeze Proteins into Polymer Coatings Using Site-Selective Bioconjugation. *J Am Chem Soc*. 2010;132(38):13264-13269. doi:10.1021/ja103038p

260. He Z, Xie WJ, Liu Z, et al. Tuning ice nucleation with counterions on polyelectrolyte brush surfaces. *Science advances*. 2016;2(6):e1600345.

261. Liu Z, He Z, Lv J, et al. Ion-specific ice propagation behavior on polyelectrolyte brush surfaces. *RSC Adv*. 2017;7(2):840-844. doi:10.1039/C6RA24847K

262. Nagura M, Saitoh H, Gotoh Y, Ohkoshi Y. States of water in poly(vinyl alcohol)/poly(sodium l-glutamate) blend hydrogels. *Polymer*. 1996;37(25):5649-5652. doi:10.1016/S0032-3861(96)00417-X

263. Wolfe J, Bryant G, Koster KL. What is “unfreezable water”, how unfreezable is it and how much is there? *Cryoletters*. 2002;23(3):157-166.

264. Wu S, He Z, Zang J, et al. Heterogeneous ice nucleation correlates with bulk-like interfacial water. *Sci Adv*. 2019;5(4):eaat9825. doi:10.1126/sciadv.aat9825

265. Ping ZH, Nguyen QT, Chen SM, Zhou JQ, Ding YD. States of water in different hydrophilic polymers — DSC and FTIR studies. *Polymer*. 2001;42(20):8461-8467. doi:10.1016/S0032-3861(01)00358-5

266. Guan L, Xu H, Huang D. The investigation on states of water in different hydrophilic polymers by DSC and FTIR. *Journal of Polymer Research*. 2011;18(4):681-689. doi:10.1007/s10965-010-9464-7

267. Hatakeyama H, Hatakeyama T. Interaction between water and hydrophilic polymers. *Thermochimica Acta*. 1998;308(1):3-22. doi:10.1016/S0040-6031(97)00325-0

268. Cai H, Kou R, Liu G. Counterion-Tunable Thermosensitivity of Strong Polyelectrolyte Brushes. *Langmuir*. 2019;35(51):16862-16868. doi:10.1021/acs.langmuir.9b02982

269. Chernyy S, Järn M, Shimizu K, et al. Superhydrophilic Polyelectrolyte Brush Layers with Imparted Anti-Icing Properties: Effect of Counter ions. *ACS Appl Mater Interfaces*. 2014;6(9):6487-6496. doi:10.1021/am500046d

270. Kou R, Zhang J, Chen Z, Liu G. Counterion Specificity of Polyelectrolyte Brushes: Role of Specific Ion-Pairing Interactions. *ChemPhysChem*. 2018;19(11):1404-1413. doi:10.1002/cphc.201701256

271. Zhao Y-H, Wee K-H, Bai R. Highly hydrophilic and low-protein-fouling polypropylene membrane prepared by surface modification with sulfobetaine-based zwitterionic polymer through a combined surface polymerization method. *Journal of Membrane Science*. 2010;362(1):326-333. doi:10.1016/j.memsci.2010.06.037

272. Liang B, Zhang G, Zhong Z, Huang Y, Su Z. Superhydrophilic Anti-Icing Coatings Based on Polyzwitterion Brushes. *Langmuir*. 2019;35(5):1294-1301. doi:10.1021/acs.langmuir.8b01009

273. Tao C, Bai S, Li X, et al. Formation of zwitterionic coatings with an aqueous lubricating layer for antifogging/anti-icing applications. *Progress in Organic Coatings*. 2018;115:56-64. doi:10.1016/j.porgcoat.2017.11.002

274. Zou W, Fan Z, Zhai S, Wang S, Xu B, Cai Z. A multifunctional antifog, antifrost, and self-cleaning zwitterionic polymer coating based on poly (SBMA-co-AA). *Journal of Coatings Technology and Research*. Published online 2020:1-12.

275. Liu C, Lee J, Small C, Ma J, Elimelech M. Comparison of organic fouling resistance of thin-film composite membranes modified by hydrophilic silica nanoparticles and zwitterionic polymer brushes. *Journal of Membrane Science*. 2017;544:135-142.

276. Nguyen JL, Schwartz J, Dockery DW. The relationship between indoor and outdoor temperature, apparent temperature, relative humidity, and absolute humidity. *Indoor Air*. 2014;24(1):103-112. doi:10.1111/ina.12052

277. Liu K, Wang C, Ma J, et al. Janus effect of antifreeze proteins on ice nucleation. *Proc Natl Acad Sci USA*. 2016;113(51):14739. doi:10.1073/pnas.1614379114

278. He Z, Liu K, Wang J. Bioinspired Materials for Controlling Ice Nucleation, Growth, and Recrystallization. *Acc Chem Res*. 2018;51(5):1082-1091. doi:10.1021/acs.accounts.7b00528

279. Geng H, Yao B, Zhou J, et al. Size Fractionation of Graphene Oxide Nanosheets via Controlled Directional Freezing. *J Am Chem Soc*. 2017;139(36):12517-12523. doi:10.1021/jacs.7b05490

280. Guo P, Zheng Y, Wen M, Song C, Lin Y, Jiang L. Icephobic/Anti-Icing Properties of Micro/Nanostructured Surfaces. *Advanced Materials*. 2012;24(19):2642-2648. doi:10.1002/adma.201104412

281. Huang Y, Hu M, Yi S, et al. Preparation and characterization of silica/fluorinated acrylate copolymers hybrid films and the investigation of their icephobicity. *Thin Solid Films*. 2012;520(17):5644-5651. doi:10.1016/j.tsf.2012.04.067

282. Li S-N, Li B, Yu Z-R, et al. Constructing dual ionically cross-linked poly (acrylamide-co-acrylic acid)/chitosan hydrogel materials embedded with chitosan decorated halloysite nanotubes for exceptional mechanical performance. *Composites Part B: Engineering*. Published online 2020:108046.

283. Tran TN, Ramanan SN, Lin H. Synthesis of hydrogels with antifouling properties as membranes for water purification. *JoVE (Journal of Visualized Experiments)*. 2017;(122):e55426.

284. Bu IYY, Oei SP. Hydrophobic vertically aligned carbon nanotubes on Corning glass for self cleaning applications. *Applied Surface Science*. 2010;256(22):6699-6704. doi:10.1016/j.apsusc.2010.04.073

285. Taga Y. Recent progress in coating technology for surface modification of automotive glass. *Journal of Non-Crystalline Solids*. 1997;218:335-341. doi:10.1016/S0022-3093(97)00281-0

286. Dehbi A, Guentay S. A model for the performance of a vertical tube condenser in the presence of noncondensable gases. *Nuclear Engineering and Design*. 1997;177(1):41-52. doi:10.1016/S0029-5493(97)00184-2

287. Rajappan A, Golovin K, Tobelmann B, et al. Influence of textural statistics on drag reduction by scalable, randomly rough superhydrophobic surfaces in turbulent flow. *Physics of Fluids*. 2019;31(4):042107. doi:10.1063/1.5090514

288. Xia F, Jiang L. Bio-Inspired, Smart, Multiscale Interfacial Materials. *Advanced Materials*. 2008;20(15):2842-2858. doi:10.1002/adma.200800836

289. Tuteja A, Choi W, Ma M, et al. Designing Superoleophobic Surfaces. *Science*. 2007;318(5856):1618. doi:10.1126/science.1148326

290. Zhang X, Shi F, Niu J, Jiang Y, Wang Z. Superhydrophobic surfaces: from structural control to functional application. *J Mater Chem*. 2008;18(6):621-633. doi:10.1039/B711226B

291. Ma M, Hill RM, Rutledge GC. A Review of Recent Results on Superhydrophobic Materials Based on Micro- and Nanofibers. *null*. 2008;22(15):1799-1817. doi:10.1163/156856108X319980

292. Li Y, Li L, Sun J. Bioinspired Self-Healing Superhydrophobic Coatings. *Angewandte Chemie International Edition*. 2010;49(35):6129-6133. doi:10.1002/anie.201001258

293. Golovin K, Boban M, Mabry JM, Tuteja A. Designing Self-Healing Superhydrophobic Surfaces with Exceptional Mechanical Durability. *ACS Appl Mater Interfaces*. 2017;9(12):11212-11223. doi:10.1021/acsami.6b15491

294. Wang J-K, Zhou Q, Wang J-P, Yang S, Li GL. Hydrophobic self-healing polymer coatings from carboxylic acid- and fluorine-containing polymer nanocontainers. *Colloids*

and Surfaces A: Physicochemical and Engineering Aspects. 2019;569:52-58. doi:10.1016/j.colsurfa.2019.02.050

295. Youngblood JP, Sottos NR. Bioinspired Materials for Self-Cleaning and Self-Healing. *MRS Bulletin*. 2008;33(8):732-741. doi:10.1557/mrs2008.158

296. Azimi G, Dhiman R, Kwon H-M, Paxson AT, Varanasi KK. Hydrophobicity of rare-earth oxide ceramics. *Nature Materials*. 2013;12(4):315-320. doi:10.1038/nmat3545

297. Verho T, Bower C, Andrew P, Franssila S, Ikkala O, Ras RHA. Mechanically Durable Superhydrophobic Surfaces. *Advanced Materials*. 2011;23(5):673-678. doi:10.1002/adma.201003129

298. Peng C, Chen Z, Tiwari MK. All-organic superhydrophobic coatings with mechanochemical robustness and liquid impalement resistance. *Nature Materials*. 2018;17(4):355-360. doi:10.1038/s41563-018-0044-2

299. Jaikumar A, Kandlikar SG. Enhanced pool boiling heat transfer mechanisms for selectively sintered open microchannels. *International Journal of Heat and Mass Transfer*. 2015;88:652-661. doi:10.1016/j.ijheatmasstransfer.2015.04.100

300. J. P. O’Connor, Seung Mun You, D. C. Price. A dielectric surface coating technique to enhance boiling heat transfer from high power microelectronics. *IEEE Transactions on Components, Packaging, and Manufacturing Technology: Part A*. 1995;18(3):656-663. doi:10.1109/95.465166

301. Bergles AE. High flux boiling applied to microelectronics thermal control. *International Communications in Heat and Mass Transfer*. 1988;15(4):509-531. doi:10.1016/0735-1933(88)90045-0

302. S. Dashi, T. Yong, T. Biao. Enhanced Boiling Microstructures Applied to Microelectronics Cooling. In: *2009 International Conference on Measuring Technology and Mechatronics Automation*. Vol 3. ; 2009:380-383. doi:10.1109/ICMTMA.2009.612

303. Hetsroni G, Mosyak A, Segal Z, Ziskind G. A uniform temperature heat sink for cooling of electronic devices. *International Journal of Heat and Mass Transfer*. 2002;45(16):3275-3286. doi:10.1016/S0017-9310(02)00048-0

304. Grill A. Diamond-like carbon: state of the art. *Diamond and Related Materials*. 1999;8(2):428-434. doi:10.1016/S0925-9635(98)00262-3

305. Robertson J. Properties of diamond-like carbon. *Surface and Coatings Technology*. 1992;50(3):185-203. doi:10.1016/0257-8972(92)90001-Q

306. Aisenberg S, Chabot R. Ion-Beam Deposition of Thin Films of Diamondlike Carbon. *Journal of Applied Physics*. 1971;42(7):2953-2958. doi:10.1063/1.1660654

307. Lei Wang, Sidi Gong, Cihui Yang, Jing Wen. Electrical resistivity optimization of diamond-like carbon thin film for electrical probe storage application. *Nanotechnology Reviews*. 2016;5(5):461-466. doi:10.1515/ntrev-2016-0032

308. Koppert R, Goettel D, Freitag-Weber O, Schultes G. Nickel containing diamond like carbon thin films. *Solid State Sciences*. 2009;11(10):1797-1800. doi:10.1016/j.solidstatesciences.2009.04.022

309. Yang Y-S, Huang W. A grey-fuzzy Taguchi approach for optimizing multi-objective properties of zirconium-containing diamond-like carbon coatings. *Expert Systems with Applications*. 2012;39(1):743-750. doi:10.1016/j.eswa.2011.07.067

310. Ghadai RK, Kalita K, Mondal SC, Swain BP. PECVD process parameter optimization: towards increased hardness of diamond-like carbon thin films. *null*. 2018;33(16):1905-1913. doi:10.1080/10426914.2018.1512114

311. Tabbal M, Mérel P, Chaker M, et al. Synthesis of diamond-like-carbon coatings by pulsed laser deposition: optimization of process parameters. *Surface and Coatings Technology*. 1999;116-119:452-455. doi:10.1016/S0257-8972(99)00183-8

312. Bao T, Morrison PW, Woyczynski WA. Parametric optimization of microhardness of diamond-like carbon films prepared by plasma enhanced chemical vapor deposition. *Thin Solid Films*. 2005;485(1):27-41. doi:10.1016/j.tsf.2005.03.026

313. Sønderby S, Berthelsen AN, Almtoft KP, Christensen BH, Nielsen LP, Bøttiger J. Optimization of the mechanical properties of magnetron sputtered diamond-like carbon coatings. *Diamond and Related Materials*. 2011;20(5):682-686. doi:10.1016/j.diamond.2011.03.016

314. Hang L, Yin Y, Xu J. Optimisation of diamond-like carbon films by unbalanced magnetron sputtering for infrared transmission enhancement. *Thin Solid Films*. 2006;515(1):357-361. doi:10.1016/j.tsf.2005.12.099

315. Tang J-F, Tsai Y-J, Huang C-H, et al. Effects of process parameters on optical characteristics of diamond-like carbon thin films deposited using high-power impulse magnetron sputtering. *Thin Solid Films*. 2019;690:137562. doi:10.1016/j.tsf.2019.137562

316. Bendavid A, Martin PJ, Randeniya L, Amin MS, Rohanizadeh R. The properties of fluorine-containing diamond-like carbon films prepared by pulsed DC plasma-activated chemical vapour deposition. *Diamond and Related Materials*. 2010;19(12):1466-1471. doi:10.1016/j.diamond.2010.10.001

317. Bendavid A, Martin PJ, Randeniya L, Amin MS. The properties of fluorine containing diamond-like carbon films prepared by plasma-enhanced chemical vapour deposition. *Diamond and Related Materials*. 2009;18(1):66-71. doi:10.1016/j.diamond.2008.09.021

318. Yu GQ, Tay BK, Sun Z. Fluorinated amorphous diamond-like carbon films deposited by plasma-enhanced chemical vapor deposition. *Surface and Coatings Technology*. 2005;191(2):236-241. doi:10.1016/j.surfcoat.2004.04.060

319. Ahmed SkF, Banerjee D, Chattopadhyay KK. The influence of fluorine doping on the optical properties of diamond-like carbon thin films. *Vacuum*. 2010;84(6):837-842. doi:10.1016/j.vacuum.2009.11.009

320. Sundaram NG, Ramachandran S, Lee G-S, Overzet L. Study and Optimization of PECVD Films Containing Fluorine and Carbon Layered with Diamond Like Carbon Films as Ultra Low Dielectric Constant Interlayer Dielectrics. *MRS Proceedings*. 2013;1511:mrsf12-1511-ee12-04. doi:10.1557/opl.2013.37

321. Grischke M, Hieke A, Morgenweck F, Dimigen H. Variation of the wettability of DLC-coatings by network modification using silicon and oxygen. *Diamond and Related Materials*. 1998;7(2):454-458. doi:10.1016/S0925-9635(97)00237-9

322. Hatada R, Baba K. Preparation of hydrophobic diamond like carbon films by plasma source ion implantation. *Nuclear Instruments and Methods in Physics Research Section B: Beam Interactions with Materials and Atoms*. 1999;148(1):655-658. doi:10.1016/S0168-583X(98)00745-9

323. He X-M, Hakovirta M, Nastasi M. Hardness, hydrophobic and optical properties of fluorine and boron co-alloyed diamond-like carbon films. *Materials Letters*. 2005;59(11):1417-1421. doi:10.1016/j.matlet.2004.11.059

324. Tang G, Ma X, Sun M, Li X. Mechanical characterization of ultra-thin fluorocarbon films deposited by R.F. magnetron sputtering. *Carbon*. 2005;43(2):345-350. doi:10.1016/j.carbon.2004.09.022

325. Cheng C-L, Chia C-T, Chiu C-C, Wu C-C, Lin I-N. Hydrogen effects on the post-production modification of diamond-like carbon produced by pulsed laser deposition. *Diamond and Related Materials*. 2001;10(3):970-975. doi:10.1016/S0925-9635(00)00508-2

326. Angus JC. Empirical categorization and naming of “diamond-like” carbon films. *Thin Solid Films*. 1986;142(1):145-151. doi:10.1016/0040-6090(86)90310-X

327. Grill A. Review of the tribology of diamond-like carbon. *Wear*. 1993;168(1-2):143-153.

328. Voevodin AA, Donley MS. Preparation of amorphous diamond-like carbon by pulsed laser deposition: a critical review. *Surface and Coatings Technology*. 1996;82(3):199-213. doi:10.1016/0257-8972(95)02734-3

329. Yu GQ, Tay BK, Sun Z, Pan LK. Properties of fluorinated amorphous diamond like carbon films by PECVD. *Applied Surface Science*. 2003;219(3):228-237. doi:10.1016/S0169-4332(03)00644-5

330. Jiang M, Ning Z. Influence of deposition pressure on the structure and properties of fluorinated diamond-like carbon films prepared by RF reactive magnetron sputtering. *Surface and Coatings Technology*. 2006;200(12):3682-3686. doi:10.1016/j.surfcoat.2005.03.023

331. Piwowarczyk J, Jędrzejewski R, Moszyński D, Kwiatkowski K, Niemczyk A, Baranowska J. XPS and FTIR Studies of Polytetrafluoroethylene Thin Films Obtained by Physical Methods. *Polymers (Basel)*. 2019;11(10):1629. doi:10.3390/polym11101629